

https://dspace.org/

Quantum many-body correlations in low-dimensional systems

Pelwan, Chad

2020
https://hdl.handle.net/10539/31004

Downloaded from a DSpace repository. https://dspace.org/

University of the Witwatersrand

Quantum Many-body Correlations in Low-dimensional Systems

Author:
Chad Pelwan (441424)

Principal Supervisor:
Dr. Izak Snyman

Co-supervisor:
Prof. Alexander Quandt



A thesis submitted to the Faulty of Science, University of the Witwatersrand, Johannesburg, in fulfilment of the requirements for the degree of Doctor of Philosophy.

September 2020

Declaration

I, Chad Dean Pelwan, declare that this thesis entitled, "Quantum Many-body Correlations in Low-dimensional Systems", and the work presented in it, are my own. It is being submitted for the degree of Doctor of Philosophy at the University of the Witwatersrand, Johannesburg. It has not been submitted before for any degree or examination at any other university.

The study performed in Part I was conceptualised by Dr. Izak Snyman we performed the simulations and calculations independently. Chapter 3 is based on the article "Ultraviolet dynamics from ground-state overlap in the Kondo model" *Phys. Rev. B* **99** (2019) 075432, which I co-authored with my supervisor, Dr. Izak Snyman. My supervisor and I derived each result separately before comparing our work to eliminate errors. I used the published text as a template for the thesis chapter, but made extensive additions and modifications. The study performed in Part II was conceptualised by Prof. Alexander Quandt and I had performed the simulations and calculations. The latter part of Chapter 5 is based on the article "Onset times of long-lived rogue waves in an optical waveguide array" *J. Opt. Soc. Am. A* **37**, C67-C72 (2020).

Signed: 

Date: 5th October 2020

Abstract

In Part I, we consider a quantum quench from the strongly correlated ground state of the Kondo model to a Fermi sea. We calculate the overlap between the ground states before and after the quench, as well as the Loschmidt echo, that is, the transition amplitude between the initial state and the evolved state at a time t after the quench. The overlap is known to determine the dynamics of the echo at large times. We show, in addition, that the overlap depends algebraically on the emergent Kondo length, with a power-law exponent that is the difference of long- and short-time contributions that appear in the echo. Our result suggests that, in general, there may be more information contained in the overlap than previously recognized.

In Part II, we study the effects of increasing modulation instability and random fluctuations on the onset times of rogue waves in a waveguide array as described by the discrete unstable nonlinear Schrödinger equation (UNLSE). We analytically determine regions of instability, where rogue waves are likely to occur in the UNLSE and then we use numerical techniques to study the time evolution of these systems. We find that the effects of the fluctuations are prominent on the onset times of rogue waves only for small modulation instability, but otherwise large modulation instability dominates the onset time behaviour.

Acknowledgements

This work is indebted to the guidance of my supervisors Dr. Izak Snyman and Prof. Alexander Quandt. Thank you both for your patience and encouragement during this research. I am grateful to have worked with, and learned from, such distinguished and accomplished physicists. Additionally, I would like to thank Dr. Robert Warmbier for his assistance and encouragement, particularly towards the end of the research. This work is based on the research supported wholly by the National Research Foundation of South Africa (Grant Number: 107867).

On a personal note, I would like to thank my parents and my sister for their understanding and their unwavering support. Lastly, I would like to thank Julia for her love and for teaching me that the deep stillness we seek does not arise because the world is still, but that it is nourished when we allow things to be just as they are for now.

Contents

Declaration ii

Abstract iii

Acknowledgements iv

Contents v

List of Figures vii

Nomenclature ix

1 Introduction 1

I 4

2 Introduction 5

3 UV dynamics from ground-state overlap in the Kondo model 20
3.1 Outline of Chapter 3 . . . 20
3.2 The Kondo Model . . . 21
3.2.1 Aims and Main Findings . . . 22
3.3 Analysis . . . 23
3.4 Identifying the Variational Parameters of the Multicoherent-state Expansion . . . 26
3.5 Loschmidt Echo: Long-time Behaviour . . . 28
3.6 The Kondo Model and Anderson's Orthogonality Theorem . . . 32
3.7 Further Analytical Progress in Ohmic Case . . . 33
3.8 Kondo Length Dependence of the Overlap . . . 38
3.8.1 Analytical Results at Small α . . . 39
3.9 Numerical Results . . . 40
3.10 Conclusion . . . 46

Appendices 47

A Further Numerical Results 47

II **49**

4 Introduction **50**
4.1 A Brief History of Rogue Waves in the Ocean 50
4.2 The Nonlinear Schrödinger Equation 53
4.3 Nonlinear Optics 54
4.4 Discrete Optical Waveguide Arrays 57
4.5 Solutions to the NLSE and Modulation Instability 60

5 Rogue Waves Originating from Modulation Instability in the UNLSE **64**
5.1 The Unstable Nonlinear Schrödinger Equation 65
5.1.1 Aims 65
5.2 Analytical Analysis: Modulation Instability 66
5.3 Rogue Wave Solutions to the UNLSE 69
5.4 Conclusions 77

Appendices **78**

B Numerical Analysis **78**

6 Summary **81**

References **95**

List of Figures

2.1 Logarithmic discretisation of states in a conduction band where intervals contain exactly one single-particle orbital and $\varepsilon_F = 0$. 9
2.2 The behaviour of an observable quantity Q calculated using NRG where each point represents a recalculating of Q at a smaller value of Λ. A convergence to a limiting value is observed as Λ decreases. 10
2.3 Ground state energy of the kinetic term for the Kondo Hamiltonian. 12
2.4 Low energy excitations for (i) one (ii) two, and (iii) three particle excitations in the kinetic term of the Kondo Hamiltonian. 13
2.5 Ground state energy of the kinetic term for the SB Hamiltonian. 13
2.6 Low energy excitations for (i) one (ii) two, and (iii) three particle excitations in the kinetic term of the SB Hamiltonian. 14

3.1 The amplitudes of the Loschmidt echo vs time in units of a. The various panels are calculated using Eq. 3.56 making use of the expression for Eq. 3.58 for $\alpha = 0.85$ and various values of α'. The different curves correspond to different values of $\Delta/a \in \{0.156, 0.18, 0.205, 0.23, 0.255, 0.28, 0.305\}$. 41
3.2 The Kondo length ξ vs Δ both in units of a. For each line, the ground state of $H_{\alpha,\Delta}$ is numerically calculated each of the parameter values of α and Δ. 42
3.3 The amplitudes of the scaled Loschmidt echoes vs time in units of Z and ξ given in Eqs. 3.84 and 3.85, respectively. The insets show the corresponding unscaled data vs time in units a. The sloped dashed lines represent the power-law decay for $|P(t)|/Z = C(t/a)^{-\xi/2}$, with C and ξ obtained by fitting to amplitude data for $t < 10^{-1}\xi$. 43
3.4 Symbols: The short-time power-law exponent χ defined in Eq. 3.77 at five different values of α' as extracted from our numerical $P(t)$ data. Curves: The small α prediction $\chi = (\varphi/\pi - \varphi'/\pi)$. 44
3.5 Symbols: The ground state to ground state overlap squared $|\langle\alpha', 0|\alpha, \Delta\rangle|$ vs the Kondo length ξ for various values of α' for a fixed $\alpha = 0.85$. Lines: The power-law $|\langle\alpha', 0|\alpha, \Delta\rangle| = G\xi^{\eta}$, with G and η obtained by fitting the data with $\xi \gtrapprox 25a$. 45
3.6 Symbols: Each data point corresponds to a fixed value of α and β. The x and y coordinates of each point are respectively $(\beta - \xi)/2$, with a short-time power-law exponent ξ cf. Eq. 3.86, as extracted from the data in such as that plotted in Fig. 3.5. Black lines: The heuristic prediction $\eta = (\beta - \chi)/2$. Inset: An enlarged view of the clustered $\beta = 0.3$ data. 46

A.1 The amplitudes of the scaled Loschmidt echoes vs time in units of Z and ξ given in Eqs. 3.84 and 3.85, respectively. The insets show the corresponding unscaled data vs time in units a. The sloped dashed lines represent the power-law decay for $|P(t)|/Z = C(t/a)^{-\xi/2}$, with C and ξ obtained by fitting to amplitude data for $t < 10^{-1}\xi$. 47

A.2 The amplitudes of the scaled Loschmidt echoes vs time in units of Z and ξ given in Eqs. 3.84 and 3.85, respectively. The insets show the corresponding unscaled data vs time in units a. The sloped dashed lines represent the power-law decay for $|P(t)|/Z = C(t/a)^{-\xi/2}$, with C and ξ obtained by fitting to amplitude data for $t < 10^{-1}\xi$. 48

4.1 A schematic illustration of a possible experimental set up to study the NLSE. The waveguide system consists of $Al_xGa_{1-x}As$ multilayerd cladding, the layers of which are usually grown on top of a GaAs substrate with increasing refractive index to ensure nonlinearity. A focused light beam is injected into a waveguide and is allowed to propagate along the length of the waveguide array. These waveguides usually have a defined separation distance between waveguides of a particular width and the dotted lines indicate the overlapping modal amplitudes to allow for tunnelling into neighbouring waveguides. 59
4.2 The effect of MI in a nonlinear medium on a finite amplitude plane wave in the time (left) and frequency (right) domain. The left panel depicts how the plane wave becomes unstable to a small perturbation which results in wave envelopes. The right panel depicts how sideband frequencies grow to the left and right of an intensity peak representing the carrier wave frequency, ω_0. Adapted from [1]. 61
4.3 Modulation instability as a function of ω, where the grey, dashed lined indicates a maximum at $\omega = \sqrt{2}$ corresponding to the value $a = 0.25$. 62
4.4 Solution to Eq. 4.16, where we plot $|\psi(\xi, \tau)|^2$. This yields a Peregrine soliton emerging from a finite background amplitude. 63

5.1 The modulation instability $\mathrm{Im}(\Omega(Q, q))$ of Eq. 5.14 with $\beta = \gamma = A_0 = 1$. The orange band in (A) depicts values where the $\mathrm{Im}(\Omega)$ is non-zero. Labels S1 and S2 identify stable points where $\mathrm{Im}(\Omega)$ is zero. The dashed box in (A) is represented in 3D in (B). In (B), each white circle indicates a point of interest, where $0 < \mathrm{Im}(\Omega) \leq 1$. 68
5.2 Time evolution of Eq. 5.1 with initial condition Eq. 5.15 showing a Peregrine rogue wave solution and profile along maximum intensity. Here, $\beta = \gamma = 1$, $N = 100$, $T = 5000$, $\epsilon = 2 \cdot 10^{-1}$, and $w = 0$. 70
5.3 Temporal evolution of Eq. 5.1 with initial condition Eq. 5.16, where $\beta = \gamma = A_0 = 1$, $N = 400$, $T = 1.6 \cdot 10^4$, $\epsilon = 1 \cdot 10^{-3}$, $w = 5 \cdot 10^{-2}$, $Q = 0$, and $q = 0.75\pi$. 72
5.4 Time evolution of Eq. 5.1 with initial condition Eq. 5.16 between $0 \leq t \lesssim 250$ for $Q = 0.31$ and $q = 0.75$ giving $\mathrm{Im}(\Omega) = 0.35$ (upper), and $Q = 1$ and $q = 0.06$ giving $\mathrm{Im}(\Omega) = 1$ (lower). Here, $\beta = \gamma = A_0 = 1$, $w = 0$, $N = 400$, $T = 1.6 \cdot 10^4$, and $\epsilon = 1 \cdot 10^{-3}$. 73
5.5 Time evolution of Eq. 5.1 with initial condition Eq. 5.16 showing multiple long-lived rogue waves for $Q = 0.31$ and $q = 0.75$ giving $\mathrm{Im}(\Omega) = 0.35$ in (A), and $Q = 1$ and $q = 0.06$ giving $\mathrm{Im}(\Omega) = 1$ in (B). Here, $\beta = \gamma = A_0 = 1$, $w = 0$, $N = 400$, $T = 1.6 \cdot 10^4$, and $\epsilon = 1 \cdot 10^{-3}$. 74
5.6 Time evolution of maximum amplitude for two different values of $\mathrm{Im}(\Omega)$, where the inset shows the time evolution for $0 \leq t \leq 500$. 75
5.7 The onset time vs $\mathrm{Im}(\Omega)$, where each line, from dark blue to orange, represents an increasing Γ_m. 76

B.1 The relative change in the total amplitude over the total time of integration $T = 1.6 \cdot 10^4$ for the Runge Kutta algorithm. Parameters in Eq. B.4 are set to $\beta = \gamma = 1$, and $w = 0$ and $w = 5 \cdot 10^{-2}$. Parameters in Eq. B.5 are set to $Q = 1$, $q = 0.06$, $\epsilon = 1 \cdot 10^{-3}$, and $A_0 = 1$, with the relative error tolerance values in both simulations set to 10^{-8}. . . . 80

Nomenclature

Acronyms

AI	Abnormality Index
1D	One-Dimensional
2D	Two-Dimensional
AIM	Anderson Impurity Model
BCH	Baker-Campbell-Hausdorff
BEC	Bose-Einstein Condensate
IR	Infrared
MI	Modulation Instability
NLSE	Nonlinear Schrödinger Equation
NRG	Numerical Renormalization Group
SB	Spin Boson
SH	Silbey-Harris
SSH	Su-Schrieffer-Heeger
UNLSE	Unstable Nonlinear Schrödinger Equation
UV	Ultraviolet

Chapter 1

Introduction

Electrons in condensed matter systems interact with each other via a repulsive Coulomb interaction. In many cases, an effective single particle description, where correlations are regarded as weak, approximates the behaviour of the system well. For instance, a model of non-interacting fermions describes the basic properties of metals surprisingly well. Even in systems with strong electronic correlations, the low energy excitations of the electrons can be regarded as quasi-particles that still behave like weakly interacting fermions. An explanation for this behaviour is provided by Fermi liquid theory [2], the success of which has been one of the landmark achievements in condensed matter physics. However, this success is mostly restricted to the description of bulk three-dimensional metals.

Systems exists where electrons are restricted to fewer than three dimensions. These are known as low-dimensional systems. Restricting the dimensions of a system does not necessarily simplify the physics. In fact, interesting quantum correlations in many-body systems are often the result of interactions between particles, which are enhanced in low-dimensional systems. These systems exhibit fascinating phenomena and for this reason, they have been the focus of much research in 21st century [3].

When describing low-dimensional systems, the theoretical description of the system is quantitatively different from that predicted by Fermi liquid theory. An intuitive understanding of this can be obtained by considering a one-dimensional wire. Here, electrons are spatially confined to move along the wire and any perturbation to the system results in collective excitations of a large number of electrons. Another system that does not follow the predictions of Fermi liquid theory is the Kondo model. This system contains impurities and displays interacting many-body behaviour at low energies [4]. Despite

being widely studied for over half a century, the Kondo model continues to provide theoretical insights worth investigating.

Quantum correlations can be harnessed in useful ways using fine tuned low-dimensional artificial systems, such as quantum wires and quantum dots. For example, low-dimensional semiconductors have been fabricated by means of a epitaxial, vapour deposition growth technique under ultra-high vacuum [5]. This method allows for the precise control of thickness and doping in the material, and has resulted in the design and construction of state-of-the-art optical and electronic devices.

In addition to this, a recently developed femtosecond laser writing technique has resulted in the fabrication of evanescent, coupled optical waveguide arrays. This system has allowed experimentalists to explore various quantum mechanical effects through a mapping that exists between the time-dependent Schrödinger equation and the paraxial approximation of the Helmholtz equation. Here, the evolution of light is spatially evolved instead of temporally. Furthermore, the field of discrete optical waveguide arrays presents a multitude of possibilities and has already seen successes in its observations of analogous optical phenomena. These include non-relativistic quantum mechanical phenomena, topological insulators, and nonlinear phenomena. The latter also highlights another success of low-dimensional systems, which are often easier realise experimentally compared to their three-dimensional counterparts.

To this end, we will study aspects relating to the temporal evolution of two one-dimensional systems, where each of these systems display interesting properties and highlight the diversity that one-dimensional systems have to offer. For this reason, the thesis is divided up into two parts, where each part consists of two chapters. The first of these chapters, Chapters 2 and 4, provide the necessary background knowledge to readers who may be unfamiliar with the respective topics. The second chapters, Chapters 3 and 5, focus on specific topics that we have studied.

The chapter descriptions are as follows:

- Chapter 2: We introduce the Kondo model and present an argument as to how this is an effective low energy model that is equivalent to the Anderson impurity model by means of a Schrieffer-Wollf transformation. By arguing that a non-perturbative method is needed to study this system, we introduce the numerical renormalization group method and provide some technical details associated with it as well as highlighting that, for the quantities we will consider, this method proves an insufficient one. Therefore, we introduce the Ohmic spin-boson model, which is equivalent to the Kondo model by means of the bosonization technique, and we

motivate why we study this model by considering a multimode coherent state expansion, which is better suited to study the quantities we consider.

- Chapter 3: We present our first study, where we consider quantum quenches from a strongly correlated ground state of the Kondo model to a Fermi sea. We state the aims of the study and present analytical and numerical calculations for the Loschmidt echo and the ground state to ground state overlap. Our results and conclusions relating to this study are then presented.

- Chapter 4: We introduce the nonlinear Schrödinger equation. We then discuss the analogous hydrodynamic counterpart of this equation and provide an historical account to the formation of rogue waves in the ocean and how they are classified. Next, we discuss continuous and discrete nonlinear optics, fields that have been used to study optical rogue wave formation. We then analyse how rogue waves are formed due to modulation instability.

- Chapter 5: We present our study on rogue wave formation in the unstable nonlinear Schrödinger equation, where we quantify the onset times of multiple rogue waves. We state our aims for the study and present our numerical and analytical results for the time evolved system. Our conclusions relating to this study are then presented.

Part I

Chapter 2

Introduction

In Chapter 2, we introduce the Kondo model and we outline how a local magnetic moment and exchange interaction comes about in the presence of a Coulomb interaction. We show this by introducing the Anderson impurity model and then argue that an effective low-energy description of this model is the Kondo model. We briefly describe the interesting aspects of the Kondo model in the context of many-body physics and we discuss that a non-perturbative method is necessary when studying it. Thus, we introduce the numerical renormalisation group method and then describe how physical quantities are calculated using it. By noting the limitations that the renormalisation group method possesses when calculating quantities with equal accuracy at all energy scales, we argue that an alternative scheme is required. For this reason, we introduce a multimode coherent state expansion and explain how it is used for our calculations. To make use of the expansion, we highlight the Kondo model's universality by describing its equivalence to the Ohmic spin boson model. The latter is used to obtain the results presented in Chapter 3.

Central to the work in Part I is the Kondo model [6], where the Hamiltonian reads

$$H_{s\text{-}d} = \sum_{k\sigma} \varepsilon_k c^\dagger_{k\sigma} c_{k\sigma} + 2J \vec{S}_{\text{imp}} \cdot \vec{s}_{\text{el}}(0). \tag{2.1}$$

Here, the first term describes a Fermi sea of electrons, where $c^\dagger_{k\sigma}$ creates an electron with a spin $\sigma = \{\uparrow, \downarrow\}$. The second term describes a Heisenberg type exchange, J, between the electron spin density $\vec{s}_{\text{el}}(0)$ at the origin and the local magnetic moment $\vec{S}_{\text{imp}}$. These operators are defined as

$$\vec{s}_{\text{el}} = \sum_{\sigma\sigma'} c^\dagger_\sigma \vec{\sigma}_{\sigma\sigma'} c_{\sigma'} \tag{2.2}$$

and

$$\vec{S}_{\text{imp}} = \sum_{kk'\sigma\sigma'} S_{kk'} d^{\dagger}_{k\sigma} \vec{\sigma}_{\sigma\sigma'} d_{k'\sigma'}. \tag{2.3}$$

Here, $\vec{\sigma}$ is the vector $(\sigma_x, \sigma_y, \sigma_z)$ of Pauli matrices. Let us briefly explain how this local magnetic moment and exchange interaction comes about in a system of electrons where the microscopic interaction is a Coulomb repulsion.

Consider a Fermi sea of itinerant conduction band electrons. We neglect interactions among electrons and, for a clean system, the Hamiltonian simply reads

$$H_{\text{band}} = \sum_{k\sigma} \varepsilon_k c^{\dagger}_{k\sigma} c_{k\sigma}. \tag{2.4}$$

Now consider an impurity that provides a localised d-orbital that the electrons can hop onto and off of. Since this orbital is localised, there is a high Coulombic energy cost to doubly occupy the state. Here, unlike in the case for the band orbitals, we have to take into account the Coulomb repulsion, U, between two electrons that may occupy the d-orbital. The d-orbital Hamiltonian therefore reads

$$H_{\text{imp}} = \sum_{\sigma} \varepsilon_d d^{\dagger}_{\sigma} d_{\sigma} + U d^{\dagger}_{\uparrow} d^{\dagger}_{\downarrow} d_{\downarrow} d_{\uparrow}, \tag{2.5}$$

where $d^{\dagger}_{\sigma}$ creates an electron at the impurity site. We assume that the single particle energy of the d-orbital, ε_d, lies between the bottom of the band and the Fermi energy, ε_F, while $2\varepsilon_d + U \gg \varepsilon_F$. Under these conditions, the single occupation of the d-orbital is energetically favoured. Hence, the system is expected to posses a local magnetic moment.

The d-orbital and band are coupled via a hybridization term

$$H_{\text{hybrid}} = \sum_{k\sigma} V_k \left(d^{\dagger}_{\sigma} c_{k\sigma} + c^{\dagger}_{k\sigma} d_{\sigma} \right), \tag{2.6}$$

where V_k is the coupling strength between the band orbital and the d-orbital. Hopping is local which implies that V_k is independent of k (or at worst weakly dependent on k). The full Hamiltonian $H_{\text{AIM}} = H_{\text{bath}} + H_{\text{imp}} + H_{\text{hybrid}}$ is known as the the Anderson impurity model (AIM) [7], which Anderson had developed to explain the existence of localised magnetic moments. The obvious question now is whether or not local magnetic moments survive when the hybridisation is non-zero. The presence of these local moments give rise to strongly correlated physics at low temperatures. In fact, when this model was introduced in 1961, its aim was to provide insight into the long standing experimentally

observed puzzle that at low temperatures, the resistivity of certain dilute magnetic alloys increases if the temperature T is decreased [8–10].

We will now argue that to leading order in $V_k/\min\{\varepsilon_F - \varepsilon_d, 2\varepsilon_d + U - \varepsilon_F\}$, the AIM is equivalent to the Kondo model. To zeroth order in the hybridization, the impurity is singly occupied in the ground state of the AIM. Scattering occurs through high energy virtual states, where the impurity is either unoccupied or doubly occupied. These virtual excitations lead to an exchange interaction in the effective low energy description of the singly occupied sector. This can be seen by performing a Schrieffer-Wolff transformation [11]. (This, and similar methods for finding effective low energy Hamiltonians, will be a recurring theme in this chapter.) The full ground state wave function of the system, $|\varphi\rangle$, can be decomposed into three terms: $|\varphi_0\rangle$, $|\varphi_1\rangle$, and $|\varphi_2\rangle$, where the first wave function describes a state where the impurity site is unoccupied; the second describes a state where the impurity site is singly occupied; and the third describes a state where the impurity site is doubly occupied. When $\varepsilon_d \ll \varepsilon_F$ and $U + 2\varepsilon_d \gg \varepsilon_F$, the overlaps $\langle\varphi_0|\varphi_0\rangle$ and $\langle\varphi_2|\varphi_2\rangle$ are much smaller than that of $\langle\varphi_1|\varphi_1\rangle$. The decomposed Schrödinger equation is written as

$$\begin{pmatrix} H_{00} & H_{01} & 0 \\ H_{10} & H_{11} & H_{12} \\ 0 & H_{21} & H_{22} \end{pmatrix} \begin{pmatrix} |\varphi_0\rangle \\ |\varphi_1\rangle \\ |\varphi_2\rangle \end{pmatrix} = E \begin{pmatrix} |\varphi_0\rangle \\ |\varphi_1\rangle \\ |\varphi_2\rangle \end{pmatrix}. \tag{2.7}$$

Since H_{hybrid} only allows that a single electron can hop onto and off of the impurity site, there are no terms in Eq. 2.7 that directly couple $|\varphi_0\rangle$ and $|\varphi_2\rangle$. We multiply out Eq. 2.7 as follows:

$$E\,|\varphi_0\rangle = H_{00}\,|\varphi_0\rangle + H_{01}\,|\varphi_1\rangle\,, \tag{2.8a}$$

$$E\,|\varphi_1\rangle = H_{10}\,|\varphi_0\rangle + H_{11}\,|\varphi_1\rangle + H_{12}\,|\varphi_2\rangle\,, \quad \text{and} \tag{2.8b}$$

$$E\,|\varphi_2\rangle = H_{21}\,|\varphi_1\rangle + H_{22}\,|\varphi_2\rangle\,. \tag{2.8c}$$

Since we are interested in the singly occupied state $|\varphi_1\rangle$, we solve Eqs. 2.8a and 2.8c to find that $|\varphi_0\rangle = (E - H_{00})^{-1} H_{01}\,|\varphi_1\rangle$ and $|\varphi_2\rangle = (E - H_{22})^{-1} H_{21}\,|\varphi_1\rangle$, respectively. Substituting these into Eq. 2.8b gives

$$E\,|\varphi_1\rangle = \left[H_{11} + H_{10}\,(E - H_{00})^{-1} H_{01} + H_{12}\,(E - H_{22})^{-1} H_{21}\right]|\varphi_1\rangle\,. \tag{2.9}$$

Eq. 2.9 is not a straight forward eigenvalue problem because the energy E appears on the right hand side of the equation. However, it turns out that, for excitation energies sufficiently lower than $\varepsilon_F - \varepsilon_d$

and $U + 2\varepsilon_d - \varepsilon_F$, the operators on the right hand side can be replaced with an effective (1 + 2)-body interaction Hamiltonian; we can guess its form using elementary reasoning. Since there is the direct term H_{11}, we obtain a kinetic contribution $\sum_{k\sigma} \varepsilon_k c^\dagger_{k\sigma} c_{k\sigma}$. The remaining terms are quadratic in the hybridization. This suggest that the two-body terms in the effective low energy Hamiltonian are composed of operator strings describing hop-on-hop-off or hop-off-hop-on processes. Such operator strings contain a creation and annihilation operator each associated with a conduction band orbital as well as a creation and annihilation operator associated with the d-orbital. This is indeed the case, which has been verified by detailed calculations [12].

We note that the system displays spin rotation invariance that allows for two types of terms. The first is $\vec{S}_{\text{imp}} \cdot \vec{s}_{\text{el}}$, where the component of $\vec{s}_{\text{el}}$ in the z-direction is, for example,

$$s_z = \frac{1}{2}\left(d^\dagger_\uparrow d_\uparrow - d^\dagger_\downarrow d_\downarrow\right). \tag{2.10}$$

The second term is

$$\left(d^\dagger_\uparrow d_\uparrow + d^\dagger_\downarrow d_\downarrow\right) \sum_{kk'\sigma} J_{kk'} c^\dagger_{k\sigma} c_{k'\sigma}. \tag{2.11}$$

In Eq.2.11, the operators in parentheses simply count the number of electrons in the d-orbital which, in this case, is equal to one because we consider only the singly occupied sector. Thus, Eq.2.11 is not a two-body interaction but simply a static potential scattering of band electrons. Static potential processes produce the usual decrease in resistivity at decreasing temperature. Therefore, this term is not important for understanding strong correlations and we can ignore it.

The second and third terms in parentheses in Eq. 2.9 should be second order in V_k which would correspond to hopping onto and off of the impurity site. Furthermore, $(E - H_{22})^{-1}$ corresponds, as it should, to double occupancy and gives contributions of the order of

$$(E - H_{22})^{-1} \approx (U + 2\varepsilon_d - \varepsilon_F)^{-1}, \tag{2.12}$$

while

$$(E - H_{00})^{-1} \approx (\varepsilon_F - \varepsilon_d)^{-1}. \tag{2.13}$$

Finally, owing to the weak dependence on k of the hybridization coupling, $S_{kk'}$ will also have a weak k dependence. The effective low energy Hamiltonian should therefore have the form of the Kondo Hamiltonian in Eq. 2.1 with J being of the order $O\left(V_k^2/\min\{\varepsilon_F - \varepsilon_d, U + \varepsilon_d - \varepsilon_F\}\right)$. This is indeed what a detailed calculation produces, which can be found in Refs.[12, 13].

Above we have sketched a common physical system described by the Kondo model. Now we very briefly review why the model is interesting in the context of many-body physics. As Kondo noticed, a perturbative calculation of the rate at which the localised magnetic moment scatters electrons, produces terms logarithmic in temperature [6]. This leads to a minimum resistivity at a finite temperature and a breakdown of perturbation theory at $T \to 0$. Subsequently, Anderson attempted to derive a tractable effective low energy theory in the limit of small J, by systematically tracing out conduction band energy levels far from the Fermi energy [14]. Technically his method was very similar to the Schriefer Wolff transformation that maps the AIM onto the Kondo model. The elimination of high energy modes leads to a renormalisation of J. For $J < 0$ (ferromagnetic case), J renormalises to zero as more modes are eliminated, so that at low energies one arrives at a weakly interacting effective picture. For $J > 0$ (anti-ferromagnetic case) however J is renormalised to larger and larger values until a point is reached when the assumption that J is small no longer holds. These results make it clear that non-perturbative methods are needed to study the Kondo problem.

One such non-perturbative method is the numerical renormalisation group (NRG) method which was introduced by Wilson [15]. The NRG method is a renormalisation group methods that resolves physics at decreasing energy scales. This is done by taking into account the influence the high energy states have on low energy physics before eliminating them. Unlike Anderson's method, it does not rely on small couplings or perturbative expansions. The trade-off, however, is that the method must be implemented numerically rather than analytically.

A key feature of NRG is that the continuous, single-particle spectrum $\varepsilon \in [-D, D]$ of the band in a crystal is discretised for the purposes of numerical calculations on, what is referred to as, a logarithmic gird. This is depicted in Fig. 2.1 where the grid discretisation is controlled by the discretisation parameter $\Lambda > 1$, such that each of the intervals $I_{n+} = (\Lambda^{-(n+1)}D, \Lambda^{-n}D]$ and $I_{n-} = [-\Lambda^{-n}D, -\Lambda^{-(n+1)}, D)$ where $n \in \mathbb{N}_0$ contains exactly one single-particle orbital. In the limit where $\Lambda \to 1$, the continuous original band is recovered. When calculating an observable quantity,

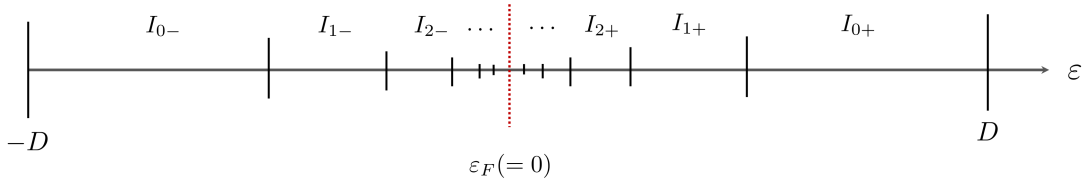

FIGURE 2.1: Logarithmic discretisation of states in a conduction band where intervals contain exactly one single-particle orbital and $\varepsilon_F = 0$.

Q, using NRG, one recalculates the same quantity at different values of Λ and hopes to observe the following behaviour depicted in Fig. 2.2 Q converges to a limiting value as Λ is decreased. The smaller

Λ becomes, the more expensive the computation becomes in terms of memory and computation time. In practice, it is challenging to perform calculations using NRG below $\Lambda \approx 1.5$ for the Kondo model

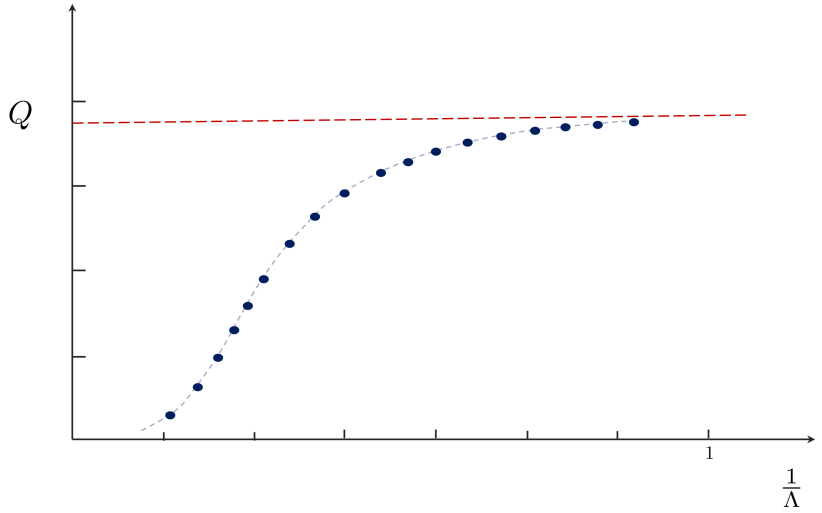

FIGURE 2.2: The behaviour of an observable quantity Q calculated using NRG where each point represents a recalculating of Q at a smaller value of Λ. A convergence to a limiting value is observed as Λ decreases.

and other related system [16]. This limits the applicability of the method to quantities for which convergence has already set in at this value of Λ. As depicted in in Fig. 2.1, the discretisation is done in such a manner that there are many levels at energies closer to the Fermi energy, while at $\Lambda = 1.5$ there is only one state in the upper sixth of the discretised band. Observables whose behaviour is determined mostly by physics at energy scales $\ll D$ can therefore be expected to show rapid convergence as Λ is reduced, while observables sensitive to physics at larger energy (or shorter time) scales likely present a tough challenge for NRG [17]. In this thesis we consider quantities that are not easily computed with NRG and therefore we require an alternative scheme for calculating them.

The method that we employ is described later in this chapter and it is based on the equivalence between the Kondo model and the Ohmic spin boson (SB) model. It is important to note that, aside from its relation to the Kondo model, the SB model has diverse applications in fields which include quantum biology [18] and superconducting nano-circuits [19]. The SB Hamiltonian describes a two-level system that is linearly coupled to a bath of harmonic oscillators. In the thermodynamic limit, the bath is completely characterized by an effective spectral density, $J(\omega)$. Usually, spectral densities with a simple power law are considered, that is, $J(\omega) \propto \alpha\omega^s$, where α plays the role of the classical coefficient of friction [20]. The parameter s indicates the type of dissipation the bath produces which is sub-Ohmic when $s < 1$, Ohmic when $s = 1$, and super-Ohmic when $s > 1$.

We now turn to the equivalence that exists between the SB model and the Kondo model. We will not provide an explicit derivation to show this equivalence. Instead, we provide a general discussion, where we relate equivalent terms in each Hamiltonian. To begin with, we state the Kondo model presented in in Eq. 2.1 in its anisotropic form

$$H_{\mathrm{AK}} = \sum_{k\sigma} \varepsilon_k c^\dagger_{k\sigma} c_{k\sigma} + J_\parallel \sigma_z S_z(0) + J_\perp \left[\sigma_- S_+(0) + \sigma_+ S_-(0)\right], \tag{2.14}$$

where $J_\parallel$ and $J_\perp$ refer to the longitudinal and transverse components of the coupling, respectively, and $S_\pm = S_x \pm iS_y$. In Eq. 2.14, we take $\varepsilon_k = 2\pi n/L$, with n running over odd multiples of $1/2$, that is, we set the Fermi energy to zero and linearise the dispersion relation around the Fermi energy. The fermions we consider are confined to an interval $[-L/2, L/2]$ in 1D. Then, the equivalent SB Hamiltonian is given by

$$H_{\mathrm{SB}} = \sum_{n=1}^{\infty} q_n \, b_n^\dagger b_n - \left(\frac{J_\parallel}{2\pi} - 1\right) \sum_{n=1}^{\infty} \sqrt{\frac{\pi q_n}{L}} e^{-aq_n/2} \left(b_n + b_n^\dagger\right) + \frac{J_\perp}{\pi a}\sigma_x, \tag{2.15}$$

where b_n are bosonic operators that satisfy the commutation relation $[b_n, b_{n'}] = 0$, $q_n = 2\pi n/L$ with $n \in \mathbb{Z}$. The factor a introduces a soft ultraviolet cut-off and the resulting regularized Hamiltonian is equivalent to the anisotropic Kondo model at energies sufficiently smaller than $1/a$. The equivalence becomes clearer when performing the following unitary transformation $UH_{\mathrm{SB}}U^\dagger = \tilde{H}_{\mathrm{SB}}$+const., where

$$U = \exp\left(\frac{-i\phi\sigma_z}{\sqrt{2}}\right), \tag{2.16}$$

with

$$\phi = i \sum_{n=1}^{\infty} \sqrt{\frac{2\pi}{q_n L}} e^{-aq_n/2} (b_n^\dagger - b_n). \tag{2.17}$$

The unitarily transformed SB Hamiltonian is given by

$$\begin{aligned} \tilde{H}_{\mathrm{SB}} = &\sum_{n=1}^{\infty} \omega_n \, b_n^\dagger b_n + \frac{J_\parallel}{2} \sum_{n}^{\infty} \sqrt{\frac{q_n}{\pi L}} e^{-aq_n/2} \left(b_n^\dagger + b_n\right) \sigma_z \\ &+ \frac{J_\perp}{2\pi a} \left[\exp\left(2 \sum_{n=1}^{\infty} \sqrt{\frac{\pi}{q_n L}} e^{-aq_n/2} (b_n^\dagger - b_n)\right) \sigma_- + \mathrm{h.c.}\right], \end{aligned} \tag{2.18}$$

where the abbreviation h.c. stands for Hermitian conjugate.

In a 1D Fermi gas, charge-density fluctuations are associated with quanta which are bosonic in nature [21]. In the unitarily transformed SB model, bosons are proportional to the Fourier modes of

the electron spin density, that is,

$$b_n = \sqrt{\frac{2}{n}} \int_{-L/2}^{L/2} dx e^{-iq_n x} S_z(x), \tag{2.19}$$

where the spin density $S_z(x) = \left(\left[\psi_\uparrow^\dagger(x)\psi_\uparrow(x) - \psi_\downarrow^\dagger(x)\psi_\downarrow(x) \right] /2 \right)$. Here, $\psi_\sigma^\dagger(x)$ creates an electron of either spin up or down at position x, and $n \in \mathbb{N}$. One can check that the bosons defined in Eq. 2.19 produce the expected bosonic commutation relations; for detailed calculations see Ref. [21]. There is an inverse relation to Eq. 2.19 that expresses fermionic operators in terms of bosonic ones. This inverse relation can be substituted into Eq. 2.15 to eventually arrive at Eq. 2.18. We will not follow this route here. Rather, we will point out how each term in Eq. 2.15 has a counterpart in Eq 2.18 that plays an identical role.

We begin with the first term in both equations representing the respective kinetic energies of the system. To intuitively understand how this term acts in the Kondo model, we consider the lowest particle-hole excitations of a free Fermi gas. We are effectively dealing with spinless fermions. This

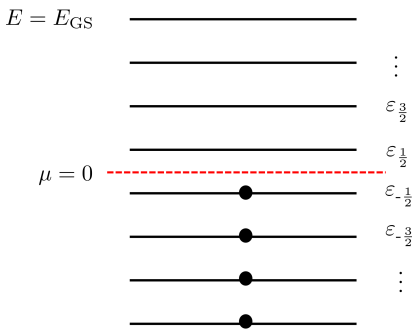

FIGURE 2.3: Ground state energy of the kinetic term for the Kondo Hamiltonian.

comes about as follows: the original spin-up and spin-down degrees of freedom are transformed to two new species of fermions, labelled "spin" and "charge", so that the density of "spin"-fermions gives the spin density of electrons, while the density of "charge"-fermions gives the charge density. Only the "spin"-fermions couple to the localised magnetic moment. The ground state of the system, with energy $E = E_{\mathrm{GS}}$, is obtained when all energy levels that lie below μ are singly occupied. This is depicted in Fig. 2.3 where the black dots indicate the occupation of a state by a single electron and the kinetic energy, $\varepsilon_k = 2\pi k/L$, with k taking half-integer values as indicated on the right-hand side. The lowest energy excitation occurs when a single electron residing in the energy state just below μ is excited to a state just above it. This process is depicted in Fig. 2.4(i) where there now exists a hole in the place where the excited electron was (indicated by the dotted white circle). The total energy

now is $E = E_{\mathrm{GS}} + (2\pi/L)$. If we excite the particle a second and third time, we observe the possible low energy excitations shown Figs. 2.4(ii) and 2.4(iii), respectively. We note that, in these respective processes, there is a two- and three-fold degeneracy, and that the total energies are $E = E_{\mathrm{GS}} + 2(2\pi/L)$ and $E = E_{\mathrm{GS}} + 3(2\pi/L)$. The low energy excitation spectrum is therefore $2\pi/L$, $4\pi/L$, and $6\pi/L$, and the respective degeneracy factors, 1, 2, and 3.

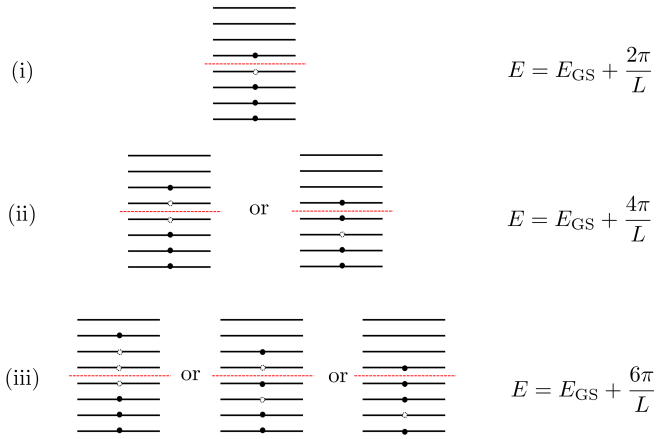

FIGURE 2.4: Low energy excitations for (i) one (ii) two, and (iii) three particle excitations in the kinetic term of the Kondo Hamiltonian.

Now consider the kinetic term in the SB model where the kinetic energy $\omega_n = 2\pi n/L$ with n taking positive, integer values and, again, the chemical potential, indicated by a red, dotted line. As shown in Fig. 2.5, the ground state of the system is given by all states above μ being unoccupied and the total energy of the system is $E = 0$. Once again, we consider the low energy excitations where we begin by exciting a single particle above μ into the first energy level. This process is depicted in Fig. 2.6(i) and the total energy is $E = 2\pi/L$. The second and third cases for low energy excitations are similar to the

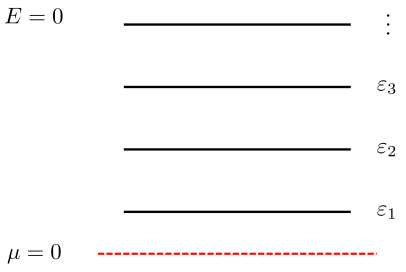

FIGURE 2.5: Ground state energy of the kinetic term for the SB Hamiltonian.

previous case, however, we are reminded that for bosons more than one particle can occupy a state. The various possibilities for these excitations are depicted in Fig. 2.6(ii) and Fig. 2.6(iii). We observe that the degeneracies and energy spectrum of this system are the same as those of the Kondo model's.

We can therefore be satisfied that the bosonic and fermionic kinetic energies are equivalent because both yield the same degeneracies and energy spectrum.

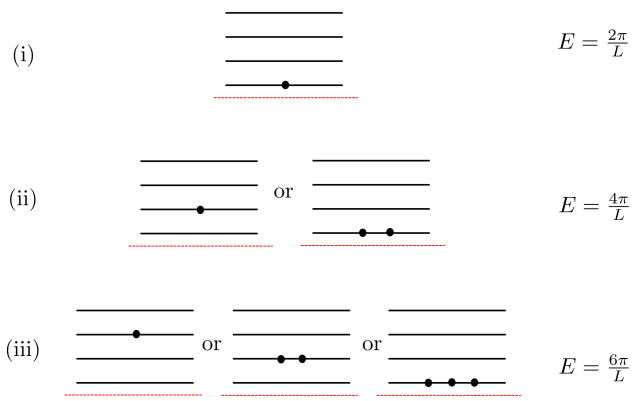

FIGURE 2.6: Low energy excitations for (i) one (ii) two, and (iii) three particle excitations in the kinetic term of the SB Hamiltonian.

The second terms in Eqs. 2.14 and 2.18 both contain the expression $J_\parallel \sigma_z$; this implies that, for them to be equivalent,

$$\sum_n^\infty \sqrt{\frac{q_n}{\pi L}} e^{-aq_n/2} \left(b_n^\dagger + b_n\right) \tag{2.20}$$

must correspond to $S_z(0)$ which is consistent with the interpretation of b_n being proportional to the Fourier modes of the electron spin density. Furthermore, by the same argument,

$$\left(\frac{1}{2\pi a}\right) \exp\left(2\sum_{n=1}^\infty \sqrt{\frac{\pi}{q_n L}} e^{-aq_n/2}(b_n^\dagger - b_n)\right) \tag{2.21}$$

must correspond to $S_+(0)$. In the anisotropic Kondo model, the commutator between these two operators $[S_z(0), S_+(0)] \propto S_+(0)$ with a positive proportionality constant of dimensions $[L^{-1}]$. It stands to reason that the corresponding terms in the SB model should produce this result as well. Therefore, consider the commutator

$$\begin{aligned}
&\left[\frac{1}{2}\sum_n^\infty \sqrt{\frac{q_n}{\pi L}} e^{-aq_n/2}\left(b_n^\dagger + b_n\right), \left(\frac{1}{2\pi a}\right)\exp\left(2\sum_{n=1}^\infty \sqrt{\frac{\pi}{q_n L}} e^{-aq_n/2}(b_n^\dagger - b_n)\right)\right] \\
&= \frac{1}{2}\sum_{n=1}^\infty \frac{2}{L} e^{-aq_n}\left[\left(b_n^\dagger + b_n\right), \left(b_n^\dagger - b_n\right)\right]\left(\frac{1}{2\pi a}\right)\exp\left(2\sum_{n'=1}^\infty \sqrt{\frac{\pi}{q_{n'} L}} e^{-aq_{n'}/2}(b_{n'}^\dagger - b_{n'})\right).
\end{aligned} \tag{2.22}$$

Here, we have used the identity $[A, e^B] = [A, B]e^B$, where A and B are operators. Furthermore, by expanding the commutator, Eq. 2.22 becomes

$$\begin{aligned}
&\frac{1}{L}\left(\sum_{n=1}^{\infty} e^{-a2\pi n/L}\right) 2\left[b_n, b_n^\dagger\right]\left(\frac{1}{2\pi a}\right)\exp\left(2\sum_{n'=1}^{\infty}\sqrt{\frac{\pi}{q_{n'}L}}e^{-aq_{n'}/2}(b_{n'}^\dagger - b_{n'})\right)\\
&= \frac{2}{L}\left(\exp\left(\frac{2\pi a}{L}\right)-1\right)^{-1}\left(\frac{1}{2\pi a}\right)\exp\left(2\sum_{n'=1}^{\infty}\sqrt{\frac{\pi}{q_{n'}L}}e^{-aq_{n'}/2}(b_{n'}^\dagger - b_{n'})\right)\\
&\approx \frac{1}{\pi a}\exp\left(2\sum_{n'=1}^{\infty}\sqrt{\frac{\pi}{q_{n'}L}}e^{-aq_{n'}/2}(b_{n'}^\dagger - b_{n'})\right),
\end{aligned} \tag{2.23}$$

where the first step was obtained using $\ln(1-x) = -\sum_{m=1}^{\infty} x^m/m$. We therefore have the expected angular momentum commutator as in the anisotropic Kondo model and, in general, we have argued that the two models are equivalent.

We have argued that the Ohmic SB model is equivalent to the Kondo model. The question to ask is how this will help us. In Chapter 3, we will use a sophisticated numerically exact technique tailored to the SB model to obtain results for the Kondo model. Here, we lay the foundation by explaining a related, qualitatively correct and simple variational ansatz that gives insight into the structure of the ground state of the SB model. We begin by stating the SB Hamiltonian in Eq. 2.15 as

$$H_{\alpha,\Delta} = \sum_{n=1}^{\infty} \omega_n b_n^\dagger b_n - \sqrt{\alpha} \sum_{n=1}^{\infty} \frac{g_n}{2} \left(b_n + b_n^\dagger \right) \sigma_z + \frac{\Delta}{2} \sigma_x, \tag{2.24}$$

where we set $\hbar = 1$ and the Fermi velocity $v_F = 1$, with

$$\omega_n = [\hbar v_F]\, q_n, \quad g_n = 2\sqrt{\frac{\pi q_n}{L}} e^{-a q_n/2}, \tag{2.25}$$

as well as

$$\alpha = \left(\frac{J_\parallel}{2\pi} - 1 \right)^2 \quad \text{and} \quad \Delta = \frac{J_\perp}{\pi a}. \tag{2.26}$$

In Eq. 2.24, ω_n is the frequency of bosonic mode n, g_n the hybridization of bosonic mode n with the two level system, and Δ is the tunnelling amplitude between the two states of the two level system. Eq. 2.24 exhibits two trivially solvable limiting cases when either $g_n = 0$ or when $\Delta = 0$. In the first case, the spin and bath are uncoupled and the ground state has every bath oscillator in its ground state, with average zero displacement, while the spin is polarized in the x-direction. The second case then describes a system of finitely displaced harmonic oscillators and whose ground state is two-fold degenerate. Depending on which of the two degenerate ground states the system is in, the oscillators are displaced in one of two directions:

$$|f_+\rangle\, |\uparrow\rangle, \quad \text{and} \quad |f_-\rangle\, |\downarrow\rangle\,. \tag{2.27}$$

Here,

$$|f_\pm\rangle = \exp\left(\pm \sum_{n=1}^{\infty} f_n \left(b_n^\dagger - b_n \right) \right) |0\rangle \tag{2.28}$$

is a multimode coherent state with $|0\rangle$ being the bosonic vacuum state and the displacement f_n is given by $f_n = \sqrt{\alpha} g_n / 2\omega_n$. It is important to note that in Eq. 2.27, the direction of the displacement of the oscillator is fully correlated with that of the spin. To interpolate between these limiting cases, the Silbey -Harris (SH) ansatz [22, 23] was introduced which is an approximate coherent state ansatz. It is the linear combination of the two ground states in Eq. 2.27 given by

$$|f^{\mathrm{SH}}\rangle = \frac{1}{\sqrt{2}} \left(|f_+\rangle\, |\uparrow\rangle - |f_-\rangle\, |\downarrow\rangle \right), \tag{2.29}$$

with f_n now treated as variational parameters obtained by calculating the variational energy $E_{\text{var}} = \langle f^{\text{SH}}| H_{\alpha,\Delta} |f^{\text{SH}}\rangle$ and then minimising it such that $\partial E_{\text{var}}/\partial f_n = 0$. We make use of the Baker-Campbell-Hausdorff (BCH) formula which states that

$$e^B A e^{-B} = \sum_{i=0}^{\infty} \frac{[B,A]_i}{i!} = A + [B,A] + \frac{1}{2!}[B,[B,A]] + \cdots . \tag{2.30}$$

where A and B are operators to perform this calculation. Thus, with the help of the BCH formula, we calculate

$$\left\langle f^{\text{SH}}\right| \sum_{n=1}^{\infty} \omega_n b_n^\dagger b_n - \sum_{n=1}^{\infty} \frac{g_n}{2}\left(b_n + b_n^\dagger\right)\sigma_z + \frac{\Delta}{2}\sigma_x \left| f^{\text{SH}}\right\rangle \tag{2.31}$$

where we have set $\alpha = 1$. We note that coherent states are eigenstates of the bosonic annihilation operator such that $b_n |f_\pm\rangle = \pm f_n |f_\pm\rangle$ and hence $\langle f_\pm| b_n^\dagger = \pm f_n \langle f_\pm|$. The first term in Eq. 2.31 is given by

$$\begin{aligned}
\left\langle f^{\text{SH}}\right| \sum_{n=1}^{\infty} \omega_n b_n^\dagger b_n \left| f^{\text{SH}}\right\rangle &= \frac{1}{2}\sum_{n=1}^{\infty} \omega_n \left(\langle\uparrow| \langle f_+| b_n^\dagger b_n |f_+\rangle |\uparrow\rangle + \langle\downarrow| \langle f_-| b_n^\dagger b_n |f_-\rangle |\downarrow\rangle\right) \\
&= \frac{1}{2}\sum_{n=1}^{\infty} \omega_n \left(\langle\uparrow| f_n^2 \langle f_+|f_+\rangle |\uparrow\rangle + \langle\downarrow| f_n^2 \langle f_-|f_-\rangle |\downarrow\rangle\right) \\
&= \sum_{n=1}^{\infty} f_n^2 \omega_n .
\end{aligned} \tag{2.32}$$

In the first line in Eq. 2.32 we note that there are only to terms that remain when expanding the state $|f^{\text{SH}}\rangle$ since, as seen in Eq. 2.29, the states $|\uparrow\rangle$ and $|\downarrow\rangle$ are orthogonal. The second term in Eq. 2.31 reads

$$\begin{aligned}
\left\langle f^{\text{SH}}\right| -\sum_{n=1}^{\infty} \frac{g_n}{2}\left(b_n + b_n^\dagger\right)\sigma_z \left| f^{\text{SH}}\right\rangle &= -\sum_{n=1}^{\infty} \frac{g_n}{4}\left(\langle\uparrow| \langle f_+| \left(b_n + b_n^\dagger\right) |f_+\rangle |\uparrow\rangle - \langle\downarrow| \langle f_-| \left(b_n + b_n^\dagger\right) |f_-\rangle |\downarrow\rangle\right) \\
&= -\sum_{n=1}^{\infty} \frac{g_n}{4}\left(\langle\uparrow| 2f_n \langle f_+|f_+\rangle |\uparrow\rangle - \langle\downarrow| - 2f_n \langle f_-|f_-\rangle |\downarrow\rangle\right) \\
&= -\sum_{n=1}^{\infty} g_n f_n .
\end{aligned} \tag{2.33}$$

In the first line in of Eq. 2.33 we note that $\sigma_z |\uparrow\rangle = |\uparrow\rangle$ and $\sigma_z |\downarrow\rangle = -|\downarrow\rangle$, which results in the change of sign for the second term. The third, and final, term in Eq. 2.31 is calculated as follows

$$\begin{aligned}
\left\langle f^{\text{SH}}\right| \frac{\Delta}{2}\sigma_x \left| f^{\text{SH}}\right\rangle &= \frac{\Delta}{4}\left(-\langle f_+|f_-\rangle - \langle f_-|f_+\rangle\right) = -\frac{\Delta}{2}\langle f_+|f_-\rangle \\
&= -\frac{\Delta}{2}\langle 0| \exp\left(-2\sum_{n=1}^{\infty} f_n (b_n^\dagger - b_n)\right)|0\rangle ,
\end{aligned} \tag{2.34}$$

where in the first line of Eq. 2.34, we note that that $\sigma_x |\uparrow\rangle = |\downarrow\rangle$ and $\sigma_x |\downarrow\rangle = |\uparrow\rangle$. In the second line, for operators A and B, if $[A, B]$ is proportional to the identity, then we can use the following BCH identity: $\exp(A + B) = \exp(A)\exp(B)\exp(-1/2[A, B])$. With this identity, we rewrite the right hand side of Eq. 2.34 as

$$\begin{aligned}
-\frac{\Delta}{2}\langle 0|\exp\left(-2\sum_{n=1}^{\infty} f_n(b_n^\dagger - b_n)\right)|0\rangle = &-\frac{\Delta}{2}\Bigg(\langle 0|\exp\left(-2\sum_{n=1}^{\infty} f_n b_n^\dagger\right)|0\rangle\,\langle 0|\exp\left(2\sum_{n=1}^{\infty} f_n b_n\right)|0\rangle \times \\
&\langle 0|\exp\left(2\sum_{n=1}^{\infty} f_n^2\left[b_n^\dagger, b_n\right]\right)|0\rangle\Bigg) \\
= &-\frac{\Delta}{2}\Bigg(\langle 0|\exp\left(-2\sum_{n=1}^{\infty} f_n b_n^\dagger\right)|0\rangle\,\langle 0|\exp\left(2\sum_{n=1}^{\infty} f_n b_n\right)|0\rangle \times \\
&\exp\left(-2\sum_{n=1}^{\infty} f_n^2\right)\Bigg). \qquad (2.35)
\end{aligned}$$

We can expand the exponents in the first two expectation values and we find that, in the first case,

$$\begin{aligned}
\langle 0|\exp\left(-2\sum_{n=1}^{\infty} f_n b_n^\dagger\right)|0\rangle &= \langle 0|\sum_{i=0}^{\infty}\frac{1}{i!}\left(-2\sum_{n=1}^{\infty} f_n b_n^\dagger\right)^i|0\rangle \\
&= 1 + \langle 0|\left(-2\sum_{n=1}^{\infty} f_n b_n^\dagger\right)|0\rangle + \frac{1}{2!}\langle 0|\left(-2\sum_{n=1}^{\infty} f_n b_n^\dagger\right)^2|0\rangle + \cdots . \qquad (2.36)
\end{aligned}$$

Here, we see that only the zeroth order term survives since, in every other term, the sums of the bosonic creation operators act on the $|0\rangle$ state. As a result, this state is now orthogonal to the state $\langle 0|$ and their overlap is zero. The same reasoning can be applied to the second expectation value in the second line of Eq. 2.35, with the sums of the bosonic annihilation operators acting on the $\langle 0|$ state. Thus,

$$\left\langle f^{\mathrm{SH}}\middle|\frac{\Delta}{2}\sigma_x\middle|f^{\mathrm{SH}}\right\rangle = -\frac{\Delta}{2}\exp\left(-2\sum_{n=1}^{\infty} f_n^2\right) \qquad (2.37)$$

and taking all three terms into consideration, we find that

$$E_{\mathrm{var}} = \sum_{n=1}^{\infty} f_n^2\omega_n - \sum_{n=1}^{\infty} g_n f_n - \frac{\Delta}{2}\exp\left(-2\sum_{n=1}^{\infty} f_n^2\right). \qquad (2.38)$$

The optimal displacements are then given by

$$\begin{aligned}\frac{\partial E_{\text{var}}}{\partial f_n} &= 0 \\ &= 2f_n\Delta\exp\left(-2\sum_{n=1}^{\infty}f_n^2\right) + 2\omega_n f_n - g_n \end{aligned} \tag{2.39}$$

which is true if, and only if,

$$f_n = \frac{g_n}{2\left(\Delta_R + \omega_n\right)}. \tag{2.40}$$

In Eq. 2.40, we have denoted

$$\Delta_R = \Delta\exp\left(-2\sum_{n=1}^{\infty}f_n^2\right) = \Delta\left\langle f_+|f_-\right\rangle = \Delta\left\langle f^{\text{SH}}|-f^{\text{SH}}\right\rangle, \tag{2.41}$$

which is the renormalised tunnelling energy that is determined self-consistently.

Chapter 3

UV dynamics from ground-state overlap in the Kondo model

3.1 Outline of Chapter 3

In Chapter 3, we consider a quantum quench from a strongly correlated ground state of the Kondo model to a Fermi sea. By quench, we mean the following: the system is prepared in the ground state. Suddenly, the Hamiltonian is changed, which in our case we abruptly switch off the Kondo coupling, and the system time-evolves with this new Hamiltonian. We will calculate the overlap between the ground states before and after the quench as well as the Loschmidt echo, which is defined as the transition amplitude between the initial and evolved state at a time t after the quench. The overlap is known to determine the dynamics of the echo at large times. We show, in addition, that the overlap depends algebraically on the emergent Kondo length, with a power-law exponent that is the difference of long and short-time contributions that appear in the echo. Our result suggests that, in general, there may be more information contained in the overlap than previously recognized. The analysis we present is based on a coherent state expansion which is a representation of the Kondo ground state in terms of a discrete set of bosonic coherent states. This is a systematic improvement of the SH ansatz in which additional variational parameters were added resulting in, in principle, an exact method. The work reported in Chapter 3 is based on the work by Pelwan and Snyman in *Phys. Rev. B* **99** (2019) 075432 [24].

When a many-body Hamiltonian is suddenly quenched, the system's full response cannot always be calculated perturbatively. This singularity is captured by the overlaps between ground states before and after a quench. One such overlap is the ground state to ground state overlap which, due to its fundamental role in non-equilibrium dynamics [25] and quantum phase transitions [26], has been calculated in settings ranging from quantum impurity models [27–29] through single-particle and many-body localised systems [30–32], to spin chains [33, 34] and lattices [35], Luttinger liquids [36], and particles with fractional exclusion statistics [37]. These studies have been done using techniques that include conformal field theory, the numerical renormalisation group, matrix product states, and tensor networks. Since the overlap compares ground states, it is not surprising that it provides information about infrared (IR) physics, such as long time dynamics.

For instance, if the interaction between a Fermi liquid and a local impurity is suddenly quenched, the transition amplitude between the initial ground state, and the time evolved state after the quench – the Loschmidt echo – decays algebraically at long times, with an exponent equal to that governing the system size dependence of the overlap [25, 38–42]. These algebraic decays are, for example, $t^{-\alpha'/2}$ and $L^{-\alpha'/2}$ for the Loschmidt echo and the ground state to ground state overlap, respectively. Here, α' is the quench parameter of the post-quench Hamiltonian in Eq. 2.24. However, unlike truly infrared probes, the ground state to ground state overlap is determined by the whole Fermi sea, not just the Fermi surface [28]. It must therefore also contain information about properties beyond the infrared, that is, ultraviolet (UV) physics. We believe that this aspect of the overlap has been neglected because of a too narrow focus on the overlap's dependence on the system size – an infrared scale. To remedy this oversight, we study a model with an emergent scale, and consider the overlap's dependence on this scale. We are not the first to do so [28, 29], but the new aspect in our study is the link we establish to non-equilibrium dynamics beyond the infrared.

3.2 The Kondo Model

We aim to find a connection between UV and IR dynamics for the anisotropic Kondo model by considering the the Loschmidt echo and overlap between ground states through their respective power-law exponents. We study the anisotropic Kondo model which is a 1D Fermi-sea coupled to a spin-1/2 magnetic moment via a local exchange interaction. For ease of reference we restate the Hamiltonian introduced in Chapter 2 here as

$$H = \sum_{k\sigma} \varepsilon_k c^\dagger_{k\sigma} c_{k\sigma} + J_\parallel S_z(0) s_z + J_\perp \left[S_x(0) s_x + S_y(0) s_y \right]. \tag{3.1}$$

Here, $\vec{S}(0)$ is the electron spin density at $x = 0$, and $\vec{s}$ is the impurity spin. The interaction famously generates an emergent scale, the Kondo temperature T_k, see Eq. 3.12 below. The impurity and Fermi sea form a spin singlet in which the impurity is screened by the electron gas at distances larger than the Kondo length $\xi = \hbar v_F / 2T_k$, where v_F is the Fermi velocity. Below, we set $\hbar = v_F = 1$.

We consider quenches $(J_\parallel, J_\perp) \to \left(J'_\parallel, 0\right)$, that is, in the pre-quench Hamiltonian defined by Eq. 3.1 we set the couplings to $(J_\parallel, J_\perp)$ and in the post-quench Hamiltonian they are set to $\left(J'_\parallel, 0\right)$. The vanishing transverse coupling $J'_\perp$ in the post-quench Hamiltonian produces a diverging Kondo length $\xi' \to \infty$. This is associated with imperfect screening of the impurity spin, and the pre- and post-quench Hamiltonians therefore have distinct infrared properties. Quenches in the Kondo and related models have been studied numerous times before, both theoretically [41–51] and experimentally [52], but the connection between the ground state to ground state overlap and dynamics beyond the infrared has not.

3.2.1 Aims and Main Findings

Our aim is to use a combination of analytical and numerical techniques to calculation the Loschmidt echo give by

$$P(t) = \langle J_\parallel, J_\perp | e^{-iH_{J'_\parallel,0}t} | J_\parallel, J_\perp \rangle \,, \tag{3.2}$$

where the state $|J_\parallel, J_\perp\rangle$ is the ground state pre-quench and $H_{J'_\parallel,0}$ is the Hamiltonian post-quench. We also calculate the ground state to ground state overlap given by

$$Q = |\langle J_\parallel, J_\perp | J'_\parallel, 0 \rangle|^2. \tag{3.3}$$

We will find distinct power-laws in the regimes $t \ll \xi$ and $t \gg \xi$, that is,

$$|P(t)| \propto \begin{cases} \left(\frac{a}{t}\right)^{\chi/2} & \text{if } a \ll t \ll \xi, \\ \left(\frac{a}{\xi}\right)^{\chi/2} \left(\frac{\xi}{t}\right)^{\beta/2} & \text{if } \xi \ll t \ll L, \end{cases} \tag{3.4}$$

where L is the system size, and a is a short-distance cut-off of the order of the Fermi wavelength. The exponent β that governs the IR dynamics ($t \gg \xi$) equals the exponent that appears in the Anderson orthogonality theorem, in agreement with previous studies [25, 28], and depends on $J'_\parallel$ but not on parameters of the pre-quench Hamiltonian, provided that $J_\perp$ is finite. When we calculate the ground

state to ground state overlap we find that

$$Q = C(J_\parallel, J'_\parallel) \left(\frac{a}{\xi}\right)^{\chi/2} \left(\frac{\xi}{L}\right)^{\beta/2} . \tag{3.5}$$

As is known already [25, 27], the L dependence of the overlap is governed by the same exponent that governs the IR dynamics of the echo. In contrast, the overlap's ξ dependence at fixed $J_\parallel$ reveals a new power-law with an exponent equal to the difference between the UV and IR exponents of the echo; this is our main result.

Previous studies [28, 29] have considered the quench $(J_\parallel, J_\perp) \to (J_\parallel, J'_\perp)$, that is, where $J_\parallel$ is held fixed during the quench, and in general the Kondo length was quenched between finite values of ξ and ξ'. A very nontrivial analytical result was obtained for the case of a finite post-quench Kondo length. However, in the limit where $\xi' \gg \xi$, that is, quenching to $J'_\perp = 0$, this result reduces to a simple power-law $|\langle J_\parallel, J_\perp | J_\parallel, J_\perp \rangle|^2 \propto (\xi/\xi)^{\beta/2}$ reminiscent of the overlap between Fermi seas, with ξ' playing the role of the system size and ξ that of the Fermi wavelength. The factor $(\xi/t)^\beta$ in our result for $P(t)$ is consistent with this interpretation: it coincides with the IR response of a Fermi sea with the Fermi wavelength ξ. In Refs [28, 29], no UV contribution to the power-law exponent for ξ is found. Consistent with this, we find that up to finite-size errors the UV contribution ξ in Eq. 3.5 vanishes when we choose $J_\parallel = J'_\parallel$. For the overlap to be sensitive to UV physics, it is therefore essential to have $J_\parallel \neq J'_\parallel$. It is tempting to interpret the factor of $(a/\xi)^{\chi/2}$ in Eq. 3.5 and the factor of $(a/t)^{\chi/2}$ in Eq. 3.4 in terms of the Anderson orthogonality theorem [53, 54] and conclude that the physics above the Kondo scale also allows an effective description in terms of (phase-shifted) Fermi seas. In the UV effective theory, ξ would play the role of an effective system size. For sufficently large $J_\parallel$, we will show analytically that this picture is indeed correct. In this regime, the exponent χ approximately equals the power-law exponent one would obtain by applying the Anderson orthogonality theorem to the trivial initial state obtained by setting $J_\perp = 0$ in the pre-quench Hamiltonian. However, for smaller $J_\parallel$, the analytical argument breaks down and we find that numerically χ states to deviate from the $J_\perp \to 0$ result. In the absence of analytical results, we cannot prove conclusively that a UV Fermi sea picture is correct, but if it is, there is a renormalisation of $J_\parallel$ from its bare value.

3.3 Analysis

In our analysis, we exploit the exact mapping known to exist between the Kondo model with non-universal UV scales integrated out and the Ohmic spin boson model [55–57] as discussed in Chapter 2.

Given a microscopic Kondo Hamiltonian that accounts for physics at all length scales down to the lattice constant, one integrates out UV modes far from the Fermi energy but stops mode elimination at a scale $1/a$ well above the Kondo temperature. At energy scales below this cut-off, the microscopic model is equivalent to an effective Hamiltonian,

$$H = \sum_{n\in\mathbb{Z};\sigma=\uparrow,\downarrow} q_n c^\dagger_{n\sigma} c_{n\sigma} + \frac{\tilde{J}_\parallel}{2}\sigma_z\left[\psi^\dagger_\uparrow\psi_\uparrow - \psi^\dagger_\downarrow\psi_\downarrow\right] + \tilde{J}_\perp\left[\sigma_-\psi^\dagger_\uparrow\psi_\downarrow + \sigma_+\psi^\dagger_\downarrow\psi_\uparrow\right], \tag{3.6}$$

involving linearly dispersing electrons, $c_{n\sigma}$, with $q_n = 2\pi/L$ with $n \in \mathbb{Z}$, in a single (unfolded) chiral channel. Here, $\sigma_\pm = \sigma_x \pm i\sigma_y$ and σ_j with $j = x, y, z$ are the Pauli matrices acting on the impurity spin. The operator

$$\psi_\sigma = \sum_n e^{-a|q_n|/2} c_{n\sigma} \tag{3.7}$$

creates an electron wave packet centred around the origin with a group velocity v_F. The width of wave packet is $\sim a$, and this enforces a soft UV cut-off at the scale at which mode elimination is halted. The tilde above the Kondo couplings $\tilde{J}_\perp$ and $\tilde{J}_\parallel$ remind us that these parameters have been renormalised from their microscopic values. Using the fact that mode elimination leaves physics at energies below $1/a$ unchanged, and that the Kondo physics only sets in at $T_k \ll 1/a$, it is possible to calibrate $J_\parallel$ with respect to the original microscopic model. This gives $\tilde{J}_\parallel = 2\varphi$, where φ is the difference between phase shifts between spin-up and spin-down electrons at the Fermi energy, when instead of the interaction, the bare Fermi sea is subjected to a spin-dependent static potential $J_\parallel S_z(0)$. The value of $\tilde{J}_\perp$ depends on the system specific UV details in a way that is hard to calculate in practice. However, many IR properties of the system, among them ones we consider, are universal functions of the Kondo scale, and this allows one to make non-trivial statements about the behaviour of the system without knowledge of the relation between microscopic parameters and the renormalised $\tilde{J}_\perp$.

The SB model, as is discussed in Chapter 2, describes a two-level system linearly coupled to a bath of harmonic oscillators. For ease of reference we state the Hamiltonian again

$$H_{\alpha,\Delta} = \sum_{n=1}^{\infty}\omega_n b_n^\dagger b_n - \sqrt{\alpha}\sum_{n=1}^{\infty}\frac{g_n}{2}\left(b_n + b_n^\dagger\right)\sigma_z + \frac{\Delta}{2}\sigma_x, \tag{3.8}$$

where b_n are bosonic annihilation operators. We take $\Delta > 0$ and denote the ground state of Eq. 3.8 as $|\Delta, \alpha\rangle$. In the thermodynamic limit, the bath spectrum becomes dense and the bath is completely characterized by the spectral function $J(\omega) = \sum_{n=1}^{\infty} g_n^2\delta(\omega - \omega_n)$. Typically, a spectral function with an IR power-law is considered and below we derive some results assuming a spectral density of the form

$$J(\omega) = 2\omega_0^{1-s}\omega^s e^{-a\omega}, \tag{3.9}$$

where $e^{-a\omega}$ is a soft UV cut-off and ω_0 is the characteristic energy scale of the bath, when the bath is not Ohmic. As discussed in Chapter 2, the low-energy Hamiltonian in Eq. 3.6 can be mapped onto Eq. 3.8 with

$$\omega_n = [\hbar v_F]\, q_n, \quad g_n = 2\sqrt{\frac{\pi q_n}{L}} e^{-aq_n/2}, \tag{3.10}$$

and

$$\alpha = \left(\frac{\tilde{J}_\parallel}{2\pi} - 1\right)^2 = \left(\frac{\varphi}{\pi} - 1\right)^2, \quad \Delta = \frac{\tilde{J}_\perp}{\pi a}. \tag{3.11}$$

In the thermodynamic limit, one introduces Dirac-δ normalised bosonic field operators $\phi_\omega = \lim_{L\to\infty} \sqrt{L/2\pi} b_n$ and calculates the Kondo length as follows [58]:

$$\xi = \lim_{\omega\to 0} \langle \alpha, \Delta | \frac{\phi_\omega + \phi_\omega^\dagger}{\sqrt{2\omega}} \sigma_z |\alpha, \Delta\rangle, \tag{3.12}$$

where $|\alpha, \Delta\rangle$ is the ground state of the SB Hamiltonian in Eq. 3.8. In the fermionic language, the above definition translates to $\xi = \lim_{x\to\infty} 4x^2 \langle S_z(x) s_z\rangle$. The familiar Kondo temperature, defined via the static spin susceptibility [59], is related to the Kondo length [60] as $T_K = 1/2\xi$. For the Kondo quenches we are interested in, we must evaluate the SB Loschmidt echo,

$$P(t) = e^{iE_{\alpha',0}t} \langle \alpha, \Delta | e^{-iH_{\alpha',0}t} |\alpha, \Delta\rangle \tag{3.13}$$

where $E_{\alpha',0}$ is the ground state energy of $H_{\alpha',0}$ given by

$$E_{\alpha',0} = -\alpha' \sum_{n=1}^{\infty} \frac{g_n^2}{4\omega_n}. \tag{3.14}$$

Here, $\alpha' = (\varphi'/\pi - 1)^2$ and the relationship between φ' and $J'_\parallel$ is the same as that between φ and $J_\parallel$. Our analysis is based on an exact expansion of the ground state Eq. 3.8 in terms of a *discrete* set of coherent states. This expansion offers a systematic way of improving the quantitatively correct and simple SH ansatz discussed in Chapter 2. The theory behind this expansion was first set out in Refs. [58, 61, 62] and below we provide a brief review.

3.4 Identifying the Variational Parameters of the Multicoherent-state Expansion

According to an elementary theorem by Cahill [63] an arbitrary state $|\psi\rangle$ of a set of bosonic modes can be written as a *discrete* sum

$$|\psi\rangle = \sum_{m=1}^{\infty} c_m |f_m\rangle , \tag{3.15}$$

where $b_n |f_m\rangle = f_{mn} |f_m\rangle$. The representation is not unique and there is always sufficient freedom to choose the coefficients f_{mn} to be real. With this convenient choice,

$$|f_m\rangle = \exp \sum_{n=1}^{\infty} f_{mn} \left(b_n^\dagger - b_n \right) |0\rangle . \tag{3.16}$$

The SB Hamiltonian is invariant with respect to a unitary transformation

$$T = \sigma_x \exp \left(i\pi \sum_{n=1}^{\infty} b_n^\dagger b_n \right) \tag{3.17}$$

that sends $b_n \rightarrow -b_n$ and $\sigma_z \rightarrow -\sigma_z$. We take $\Delta > 0$, in which case the ground state $|\alpha, \Delta\rangle$ transforms under T as $T |\alpha, \Delta\rangle = - |\alpha, \Delta\rangle$. With the help of Cahill's theorem, we can therefore exactly parametrize the ground state as

$$|\alpha, \Delta\rangle = \sum_{m=1}^{\infty} \frac{c_m}{\sqrt{2}} \left(|f_m\rangle |\uparrow\rangle - |-f_m\rangle |\downarrow\rangle \right) . \tag{3.18}$$

In order to put this result to practical use, the sum in Eq. 3.18 is truncated to a finite number of M that is sufficiently large. Significant headway can be made analytically with the variational optimization of the truncated trial state of the form

$$|\psi\rangle = \sum_{m=1}^{M} \frac{c_m}{\sqrt{2}} \left(|f_m\rangle |\uparrow\rangle - |-f_m\rangle |\downarrow\rangle \right) , \tag{3.19}$$

and here we briefly review the relevant results.

By setting the variation of $\langle H_{\alpha,\Delta}\rangle$ with respect to f_{mn} with $m = \{1, 2, \ldots, M\}$, equal to zero, one obtains a set of equations of the form

$$\left(U\omega_n + V\right)\begin{pmatrix} f_{1n} \\ \vdots \\ f_{Mn} \end{pmatrix} = \sqrt{\alpha} g_n W, \tag{3.20}$$

with the entries of the real $M \times M$ matrices U and V and the real column vector W dependent on the trial state $|\psi\rangle$. However, they are independent of the mode index n, that is, the same U, V, and W enter the equations for each n. (Explicit expression can be found in Ref. [58].) This structure comes about because (i) $H_{\alpha,\Delta}$ is quadratic in $b_n^\dagger$ and b_n, and (ii) there are no direct processes in $H_{\alpha,\Delta}$ that scatter the bosons from a mode n to a mode $n' \neq n$. By noting that each matrix element of the inverse of $U\omega_n + V$ is the ratio of polynomials in ω_n that are respectively of the order of $M - 1$ and M, and that the denominator is the same for all elements (being the determinant of $U\omega_n + V$), we discover that

$$f_{m,n} = \frac{\sqrt{\alpha}}{2} g_n \, h_m(\omega_n), \tag{3.21a}$$

$$h_m(z) = \frac{\sum_{l=0}^{M-1} \mu_{m,l} \, z^l}{\prod_{l=1}^{M} (z - \Omega_l)} \tag{3.21b}$$

where $\mu_{m,l}$ is real. Furthermore, because $U\omega_n + V$ is real, the Ω_l that are not real come in complex conjugate pairs. It is intuitively clear that for modes with natural frequencies $\omega_n \gg \Delta$, the tunnelling term $\Delta\sigma_x/2$ becomes a negligible perturbation and hence $f_{mn} \simeq \sqrt{\alpha} g_n / 2\omega_n$. This implies that that $\mu_{m,M-1} = 1$. The same conclusion follows rigorously from the observation that, associated with mode n, the are unavoidable positive contributions to the energy that are proportional to $\omega_n \left(f_{mn} - \sqrt{\alpha} g_n / 2\omega_n\right)^2$. Energy considerations also dictate that there are no poles at Ω_l on the real line. Finding the $M^2 + M - 1$ unknown parameters Ω_m, μ_{m_1,m_2}, and c_m variationally constitutes a global minimization problem that we can solve numerically. However, as we will show below, some exact results for can also be derived without explicitly computing the optimal values for Ω_m, μ_{m_1,m_2} and c_m.

An example is a result that we derive in Sec. 3.5, namely, that at large times

$$P(t) \simeq |\langle \alpha, \Delta | \alpha', 0\rangle|^2 \exp\left(\frac{\alpha'}{4} \int_0^\infty d\omega \frac{J(\omega)}{\omega^2} e^{-i\omega t}\right). \tag{3.22}$$

We also make comments on long-time behaviour of the echo specifically in the Ohmic case.

3.5 Loschmidt Echo: Long-time Behaviour

We begin by noting that because $H_{\alpha',0}$ preserves the z component of spin and it is quadratic in bosonic operators, it is straightforward to compute the time evolution of $|\alpha, \Delta\rangle$. Our calculation for the Loschmidt echo begins with an arbitrary initial state

$$P(t) = \langle\psi|e^{-iH_{\alpha',0}t}|\psi\rangle\,. \tag{3.23}$$

Considering only the exponential operator acting on the right hand side, we substitute in Eq. 3.15 and Eq. 3.16 to obtain

$$e^{-iH_{\alpha',0}t}\,|\psi\rangle = \sum_{m=1}^{M} \exp\left(-iH_{\alpha',0}t\right) c_m \exp\left(\sum_{n=1}^{\infty} f_{mn}(b_n^\dagger - b_n)\right)|0\rangle\,. \tag{3.24}$$

Now for operators A and B acting on a state, say, $|0\rangle$, we can then Taylor expand $f(B)$ such that

$$\begin{aligned} Af(B)\,|0\rangle &= A\sum_{i=0}^{\infty}\frac{f^{(i)}(0)}{i!}B^i\,|0\rangle \\ &= \sum_{i=0}^{\infty}\frac{f^{(i)}(0)}{i!}\underbrace{AB^iA^{-1}}_{(ABA^{-1})^i}A\,|0\rangle \\ &= f(ABA^{-1})A\,|0\rangle\,. \end{aligned}$$

Using this relation, we can rewrite Eq. 3.24 as

$$e^{-iH_{\alpha',0}t}\,|\psi\rangle = \sum_{m=1}^{M} c_m \exp\left(b_n^\dagger(t) - b_n(t)\right)\exp\left(-iH_{\alpha',0}t\right)|0\rangle\,, \tag{3.25}$$

where

$$b_n^\dagger(t) \equiv e^{-iH_{\alpha',0}t}b_n^\dagger e^{iH_{\alpha',0}t}, \quad \text{and} \tag{3.26a}$$

$$b_n(t) \equiv e^{iH_{\alpha',0}t}b_n e^{-iH_{\alpha'0}t}. \tag{3.26b}$$

Next, we rewrite the post-quench SB Hamiltonian 3.8 by completing the square as

$$H_{\alpha',0} = \sum_{n=1}^{\infty}\omega_n\left(b_n^\dagger - \frac{\sqrt{\alpha'}g_n}{2\omega_n}\right)\left(b_n - \frac{\sqrt{\alpha'}g_n}{2\omega_n}\right) - \alpha'\sum_{n=1}^{\infty}\frac{g_n^2}{4\omega_n}. \tag{3.27}$$

We define new bosonic operators in terms of the bracketed terms in the above. That is, we set

$$B_n^\dagger = b_n^\dagger - \frac{\sqrt{\alpha'} g_n}{2\omega_n}, \quad \text{and} \tag{3.28a}$$

$$B_n = b_n - \frac{\sqrt{\alpha'} g_n}{2\omega_n}, \tag{3.28b}$$

and note that the last term in the Hamiltonian is the ground state energy of $H_{\alpha',0}$, as previously mentioned in Eq. 3.14. We simplify our Hamiltonian to

$$H_{\alpha',0} = \sum_{n=1}^{\infty} \omega_n B_n^\dagger B_n + E_{\alpha',0}. \tag{3.29}$$

Since the ground state of $H_{\alpha',0}$ is $|\alpha', 0\rangle$, acting on it with the annihilation operator gives $B_n |\alpha', 0\rangle = 0$. This implies the following:

$$\begin{aligned} \left(b_n - \frac{\sqrt{\alpha'} g_n}{2\omega_n}\right) |\alpha', 0\rangle &= 0 \\ b_n |\alpha', 0\rangle &= \frac{\sqrt{\alpha'} g_n}{2\omega_n} |\alpha', 0\rangle , \end{aligned} \tag{3.30}$$

that is, $|\alpha', 0\rangle$ is an eigenstate of b_n. Since $|\alpha', 0\rangle$ is a multi-mode coherent state, we can use Eq. 3.16 and expand it as

$$\begin{aligned} |\alpha', 0\rangle &= \exp\left(\sum_{n=1}^{\infty} \frac{\sqrt{\alpha'} g_n}{2\omega_n} \left(b_n^\dagger - b_n\right)\right) |0\rangle \\ &= \exp\left(\sum_{n=1}^{\infty} \frac{\sqrt{\alpha'} g_n}{2\omega_n} \left(B_n^\dagger - B_n\right)\right) |0\rangle , \end{aligned} \tag{3.31}$$

where we note that $b_n^\dagger(t) - b_n(t) = B_n^\dagger(t) - B_n(t)$. By inverting the above, we solve for the vacuum state

$$|0\rangle = \exp\left(-\sum_{n=1}^{\infty} \frac{\sqrt{\alpha'} g_n}{2\omega_n} \left(B_n^\dagger - B_n\right)\right) |\alpha', 0\rangle . \tag{3.32}$$

Applying Eqs. 3.25 and 3.32 we act on the vacuum state

$$\begin{aligned} e^{-iH_{\alpha',0}t} |0\rangle &= \exp\left(-\sum_{n=1}^{\infty} \frac{\sqrt{\alpha'} g_n}{2\omega_n} \left(B_n^\dagger(t) - B_n(t)\right)\right) e^{-iH_{\alpha',0}t} |\alpha', 0\rangle \\ &= \exp\left(-\sum_{n=1}^{\infty} \frac{\sqrt{\alpha'} g_n}{2\omega_n} \left(B_n^\dagger(t) - B_n(t)\right)\right) |\alpha', 0\rangle \, e^{-iE_{\alpha',0}t} \end{aligned} \tag{3.33}$$

where $B_n^\dagger(t) = e^{-iH_{\alpha',0}t} B_n^\dagger e^{iH_{\alpha',0}t}$. Finally, we evaluate Eq. 3.24 and we do so in terms of the new bosonic operators. That is, we use the result in Eq. 3.33 together with that of Eq. 3.16 to obtain

$$\begin{aligned} e^{-iH_{\alpha',0}t}\,|\psi\rangle &= \sum_{m=1}^{M} c_m \exp\left(\sum_{n=1}^{\infty} f_{mn}\left(B_n^\dagger(t) - B_n(t)\right)\right) \exp\left(-\sum_{n=1}^{\infty}\frac{\sqrt{\alpha}g_n}{2\omega}\left(B_n^\dagger(t) - B_n(t)\right)\right)|\alpha',0\rangle\, e^{-iE_{\alpha',0}t} \\ &= \sum_{m=1}^{M} c_m \exp\left(\sum_{n=1}^{\infty}\left(f_{mn} - \frac{\sqrt{\alpha}g_n}{2\omega_n}\right)\left(B_n^\dagger e^{-i\omega_n t} - B_n e^{i\omega_n t}\right)\right)|\alpha',0\rangle\, e^{-iE_{\alpha',0}t} \end{aligned} \tag{3.34}$$

and our state $|\psi\rangle$ is given by

$$|\psi\rangle = \sum_{m=1}^{M} c_m \exp\left(\sum_{n}^{\infty}\left(f_{mn} - \frac{\sqrt{\alpha'}g_l}{2\omega}\right)\left(B_n^\dagger - B_n\right)\right)|\alpha',0\rangle\,. \tag{3.35}$$

We now have all the requirements to calculate inner product using of the two above equations. We find that

$$\begin{aligned} P(t) = \sum_{m_1,m_2=1}^{M} c_{m_1}c_{m_2}\,\langle\alpha',0|\exp\left(\left(\sum_{n}^{\infty} f_{m_1 n} - \frac{\sqrt{\alpha'}g_n}{2\omega_n}\right)\left(B_n - B_n^\dagger\right)\right)\times \\ \exp\left(\left(\sum_{n}^{\infty} f_{m_2 n} - \frac{\sqrt{\alpha}g_n}{2\omega_n}\right)\left(B_n^\dagger e^{-i\omega_n t} - B_n e^{i\omega_n t}\right)\right)|\alpha',0\rangle \end{aligned} \tag{3.36}$$

and we can expand the summation over n as follows:

$$\begin{aligned} P(t) = \sum_{m_1,m_2=1}^{M} c_{m_1}c_{m_2}\times \\ \Big[\langle\alpha',0|\exp\left(\left(f_{m_1 1} - \frac{\sqrt{\alpha'}g_1}{2\omega_1}\right)\left(B_1 - B_1^\dagger\right)\right)\exp\left(\left(f_{m_2 1} - \frac{\sqrt{\alpha}g_1}{2\omega_1}\right)\left(B_1^\dagger e^{-i\omega_1 t} - B_1 e^{i\omega_1 t}\right)\right)|\alpha',0\rangle\times \\ \langle\alpha',0|\exp\left(\left(f_{m_1 2} - \frac{\sqrt{\alpha'}g_2}{2\omega_2}\right)\left(B_2 - B_2^\dagger\right)\right)\exp\left(\left(f_{m_2 1} - \frac{\sqrt{\alpha}g_1}{2\omega_1}\right)\left(B_1^\dagger e^{-i\omega_1 t} - B_1 e^{i\omega_1 t}\right)\right)|\alpha',0\rangle\cdots\Big]. \end{aligned} \tag{3.37}$$

We express this using a product over the exponentials as

$$\begin{aligned} P(t) = \sum_{m_1,m_2=1}^{M} c_{m_1}c_{m_2}\prod_{n=1}^{\infty}\langle\alpha',0|\exp\left(\left(f_{m_1 n} - \frac{\sqrt{\alpha'}g_n}{2\omega_n}\right)\left(B_n - B_n^\dagger\right)\right)\times \\ \exp\left(\left(f_{m_2 n} - \frac{\sqrt{\alpha}g_l}{2\omega_n}\right)\left(B_n^\dagger e^{-i\omega_n t} - B_n e^{i\omega_n t}\right)\right)|\alpha',0\rangle\,. \end{aligned} \tag{3.38}$$

Now, we can set $z_{m_1} = (f_{m_1 n} - \sqrt{\alpha'}g_n/2\omega_n)$ and $z_{m_2} = (f_{m_2 n} - \sqrt{\alpha}g_n/2\omega_n)e^{-i\omega_n t}$, which yields

$$P(t) = \sum_{m_1,m_2=1}^{M} c_{m_1}c_{m_2}\prod_{n=1}^{\infty}\langle\alpha',0|\exp\left(z_{m_1}B_n - z_{m_1}^* B_n^\dagger\right)\exp\left(z_{m_2}B_n^\dagger - z_{m_2}^* B_n\right)|\alpha',0\rangle\,. \tag{3.39}$$

Written is this way, we can use the following commutation relation: if the commutator $[A, B] \in \mathbb{C}$, then $e^{A+B} = e^A e^B e^{-1/2[A,B]}$. Thus, we have that

$$P(t) = \sum_{m_1,m_2=1}^{M} c_{m_1} c_{m_2} \prod_{n=1}^{\infty} \exp\left[-\frac{1}{2}\left(\left(f_{m_1 n} - \frac{\sqrt{\alpha'} g_n}{2\omega_n}\right)^2 + \left(f_{m_2 n} - \frac{\sqrt{\alpha} g_n}{2\omega_n}\right)^2\right)\right] \times \exp\left[\left(f_{m_1 n} - \frac{\sqrt{\alpha'} g_n}{2\omega_n}\right)\left(f_{m_2 n} - \frac{\sqrt{\alpha} g_n}{2\omega_n}\right) e^{-i\omega_n t}\right]. \tag{3.40}$$

Finally, we replace the f_{mn} functions as defined in Eq. 3.21, express the product of exponentials as a sum, and group orders of the function h_m. We then have

$$P(t) = \sum_{m_1,m_2=1}^{M} c_{m_1} c_{m_2} \exp\left[-\frac{1}{2}\left(\sum_{n=1}^{\infty} \frac{g_n^2}{2}\left(\frac{\alpha}{2}\left(h_{m_1}^2 + h_{m_2}^2\right)\right) - \frac{\sqrt{\alpha\alpha'}}{\omega_n}\left(h_{m_1} + h_{m_2}\right) + \frac{\alpha'}{\omega_n^2}\right)\right] \times \exp\left[\sum_{n=1}^{\infty} e^{-i\omega_n t} \frac{g_n^2}{4} \alpha \left(h_{m_1} h_{m_2}\right) - \frac{\sqrt{\alpha\alpha'}}{\omega_n}\left(h_{m_1} + h_{m_2}\right) + \frac{\alpha'}{2\omega_n^2}\right]. \tag{3.41}$$

Finally, we simplify the expression to

$$\boxed{P(t) = \sum_{m_1,m_2}^{M} c_{m_1} c_{m_2} \langle f_{m_1} | \alpha' + \rangle \langle \alpha' + | f_{m_2} \rangle \times \exp\left(\frac{1}{4} \sum_{n=1}^{\infty} g_n^2 \left[\frac{\sqrt{\alpha'}}{\omega_n} - \sqrt{\alpha} h_{m_1}(\omega_n)\right]\left[\frac{\sqrt{\alpha'}}{\omega_n} - \sqrt{\alpha} h_{m_2}(\omega_n)\right] e^{-i\omega_n t}\right),} \tag{3.42}$$

where

$$|\alpha' \pm\rangle = \exp\left(\pm\sqrt{\alpha'} \sum_{n=1}^{\infty} \frac{g_n}{2\omega_n}\left(b_n^\dagger - b_n\right)\right)|0\rangle, \tag{3.43}$$

so that $|\alpha' +\rangle\,|\uparrow\rangle$ and $|\alpha' -\rangle\,|\downarrow\rangle$ are the two degenerate ground states of $H_{\alpha',0}$, and

$$\langle f_m | \alpha' + \rangle = \exp\left(-\frac{1}{8} \sum_{n=1}^{\infty} \left[\frac{\sqrt{\alpha'}}{\omega_n} - \sqrt{\alpha} h_m(\omega_n)\right]^2\right). \tag{3.44}$$

At long times, the frequency in the sum in Eq. 3.42 is dominated by the contribution from small frequencies, where g_n/ω_n dominates over $h_m(\omega_n)$. (Recall that the $h_m(\omega_n)$ remain finite when $\omega \to 0$.) Thus, asymptotically,

$$P(t) \simeq |\langle \alpha, \Delta | \alpha', 0 \rangle|^2 \exp\left(\frac{\alpha'}{4} \sum_{n=1}^{\infty} \left(\frac{g_n}{\omega_n}\right)^2 e^{-i\omega_n t}\right), \tag{3.45}$$

where

$$|\alpha', 0\rangle = \frac{1}{\sqrt{2}}\left(|\alpha' +\rangle\,|\uparrow\rangle - |\alpha' -\rangle\,|\downarrow\rangle\right) \tag{3.46}$$

is the ground state of $H_{\alpha',0}$ with T (given in Eq. 3.17) eigenvalue -1. In the thermodynamic limit is it convenient to rewrite the result as

$$P(t) \simeq |\langle \alpha, \Delta | \alpha', 0 \rangle|^2 \exp\left(\frac{\alpha'}{4} \int_0^\infty d\omega \, \frac{J(\omega)}{\omega^2} e^{-i\omega t} \right). \tag{3.47}$$

Whereas $P(t)$ is regular in the thermodynamic limit, if the individual factors on the right of Eq. 3.47 are calculated separately, the calculations must be performed for a finite system size. The time dependence of Eq. 3.47 is the same as

$$e^{iE_{\alpha',0}t} \langle \mathrm{IR} | \, | e^{-iH_{\alpha',0}t} \, | \mathrm{IR} \rangle \,, \tag{3.48}$$

with

$$|\mathrm{IR}\rangle = \frac{1}{\sqrt{2}} |0\rangle \left(|\uparrow\rangle - |\downarrow\rangle \right). \tag{3.49}$$

This is because in the delocalised phase, the coherent state parameters f_{mn} tend to zero for modes n whose frequencies tend to zero [60]. As a result, IR probes cannot distinguish the initial state from the bosonic vacuum. Let us now focus on the Ohmic case with $s = 1$ where, at large times compared to ξ,

$$P(t) = Q \left(\frac{2\pi i t}{L} \right)^{-\beta/2}, \tag{3.50}$$

with $\beta = \alpha'$ and where we use the Kondo and SB notations $Q \equiv |\langle \alpha, \Delta | \alpha', 0 \rangle|^2$ interchangeably. Since $P(t)$ should not vanish when we take the limit as $L \to \infty$, we conclude that $Q \propto L^{-\beta/2}$. Let us now comment further on known results and explain the previously mentioned Anderson orthogonality theorem.

3.6 The Kondo Model and Anderson's Orthogonality Theorem

The results derived at the end of the previous section, namely the algebraic decays $t^{-\alpha'/2}$ and $L^{-\alpha'/2}$ of the Loschmidt echo and the overlap of ground states, respectively, have been obtained before, for instance, using NRG technology [27]. It is a manifestation of the fact that under the renormalisation, the Kondo ground state of the pre-quench Hamiltonian flows to a strong-coupling IR fixed point of the form

$$|\mathrm{IR}\rangle = \frac{1}{\sqrt{2}} \left(|\theta = -\pi\rangle \, |\uparrow\rangle - |\theta = \pi\rangle \, |\downarrow\rangle \right), \tag{3.51}$$

where we use the notation $|\theta\rangle$ to represent a non-interacting Fermi sea in which electrons undergo phase shifts that depend on their spin direction such that, at the Fermi energy, these phase shifts equal $\theta/2$ and $-\theta/2$ for spin-up and spin-down electrons, respectively. On the other hand, the post-quench ground state is of the form

$$|\varphi', \infty\rangle = \frac{1}{\sqrt{2}} \left(|\theta = -\varphi'\rangle \, |\uparrow\rangle - |\theta = \varphi'\rangle \, |\downarrow\rangle \right), \tag{3.52}$$

where φ' now is the difference in phase shifts between spin-up and spin-down electrons at the Fermi energy. The power-law behaviour of the overlap can be understood by replacing the true initial state with $|\mathrm{IR}\rangle$ and applying the celebrated Anderson orthogonality theorem, which states that

$$| \langle \pm\pi | \pm\varphi' \rangle |^2 \propto \left(\frac{L}{\lambda_F} \right)^{-(1/2-\varphi'/2\pi)^2}, \tag{3.53}$$

where λ_F is the Fermi wavelength and the proportionality constant is of the order of unity. Since the IR fixed point of the Kondo model is reached when length which are shorter than $\sim \xi$ are integrated out, the effective Fermi wavelength to use when applying the Anderson orthogonality theorem is of order ξ. Another classic result in many-body theory [40] states that for non-interacting fermions, the Loschmidt echo decays $\propto (\varepsilon_F t)^{-(1/2-\varphi'/2\pi)^2}$, with the same power-law exponent as that governing the L dependence of the overlap. When applying this result to the long-time dynamics of the Kondo model, the effective Fermi energy to use is $\varepsilon \sim \hbar v_F/\xi$. Finally, we note that coherent-state expansion provides an analytic derivation for these results. The derivation is exact because no restriction is placed on the number M of terms to which the expansion is truncated.

3.7 Further Analytical Progress in Ohmic Case

We now turn our attention to the Loschmidt echo at arbitrary times. We also specialize to the Ohmic case, relevant for the Kondo model. In the Ohmic case, the sums appearing in $P(t)$ in Eq. 3.42 can be calculated analytically. To achieve this, we note that we study a bath comprising of a set of linearly dispersing modes given by

$$\omega_n = [\hbar v_F] \, q_n, \quad q_n = \frac{2\pi n}{L}, \quad n = 1, 2, 3, \cdots, \tag{3.54}$$

where the infrared scale is introduced via a (large) system of size L. The requirement that the bath should be Ohmic the implies that

$$g_n(q) = 2\sqrt{\frac{\pi q_n}{L}} \exp\left(-\frac{aq_n}{2}\right). \tag{3.55}$$

Using this result and rewriting the Loschmidt echo in Eq. 3.42 as

$$P(t) = \sum_{m_1 m_2 = 1}^{M} c_{m_1} c_{m_2} \langle f_{m_1} | \alpha' + \rangle \langle \alpha' + | f_{m_2} \rangle P_{m_1 m_2}(t), \tag{3.56}$$

we can write $P_{m_1 m_2}(t)$ as

$$P_{m_1 m_2}(t) = \exp\left(\sum_{n=1}^{\infty} \frac{\pi q_n e^{-(a+it)q_n}}{L} \left[\alpha h_{m_1}(q_n) h_{m_1}(q_n) - \frac{\sqrt{\alpha\alpha'}}{q_n}\left(h_{m_1}(q_n) + h_{m_2}(q_n)\right) + \frac{\alpha'}{q_n^2}\right]\right). \tag{3.57}$$

The first and second terms in the square brackets need no IR regularization, and we can replace the sum over the discrete modes with an integral. We cannot do the same with the third term. Here, however, the discrete sum is computed straightforwardly as follows:

$$\begin{aligned}
\sum_{n=1}^{\infty} \frac{\pi\alpha' e^{-aq_n}}{Lq_n} e^{-(a+it)q_n} &= \frac{\alpha'}{2} \sum_{n=1}^{\infty} \frac{\left(\exp\left(-(a+it)\frac{2\pi}{L}\right)\right)^n}{n} \\
&= -\frac{\alpha'}{2} \ln\left[1 - \exp\left(-(a+it)\frac{2\pi}{L}\right)\right] \\
&\approx -\frac{\alpha'}{2} \ln\left[\frac{2\pi}{L}(a+it)\right],
\end{aligned}$$

where, in the first line we substituted in Eq. 3.54 and in the second line we used the expansion for $-\ln(1-x)$. We then find that

$$P_{m_1 m_2}(t) = -\frac{\alpha'}{2} \ln\left[\frac{2\pi}{L}(a+it)\right] \exp\left(\frac{\alpha}{2} A_{m_1 m_2}(t) - \frac{\sqrt{\alpha\alpha'}}{2}\left(B_{m_1}(t) - B_{m_2}(t)\right)\right), \tag{3.58}$$

where

$$A_{m_1 m_2}(t) = \int_0^{\infty} dq\ q e^{-q(a+it)} h_{m_1}(q) h_{m_2}(q), \quad \text{and} \tag{3.59a}$$

$$B_m(t) = \int_0^{\infty} dq\ e^{-q(a+it)} h_m(q). \tag{3.59b}$$

We also find that

$$\langle \alpha' + | f_m \rangle = \exp\left[-\frac{\alpha}{4} A_{mm}(0) + \frac{\sqrt{\alpha'\alpha}}{2} B_m(0) \right] \left(\frac{2\pi a}{L} \right)^{\alpha'/4} . \tag{3.60}$$

The fact that $h_m(q)$ is a rational function of q allows us to perform the above integrals analytically. These results are

$$A_{m_1 m_2}(t) = e^{-i\phi} \sum_{l=1}^{M} \mathrm{Res}\left[q e^{-i\phi} h_{m_1}(q e^{-i\phi}) h_{m_2}(q e^{-i\phi}) F(q|a+it|), q = \Omega_l e^{i\phi} \right] \tag{3.61}$$

and

$$B_m(t) = e^{-i\phi} \sum_{l=1}^{M} \mathrm{Res}\left[h_{m_1} F(q|a+it|), q = \Omega_l e^{i\phi} \right], \tag{3.62}$$

where $F(z) = e^{-z}\Gamma(0,-z)$, $\Gamma(\gamma, z)$ is the incomplete Γ function, and $\mathrm{Res}[f(q), q = q_0]$ is the residue of $f(q)$ at $q = q_0$. The phase ϕ is the argument of $a + it$, that is, $e^{i\phi} = (a+it)/|a+it|$. For the purpose of evaluating the residues explicitly, we define

$$\begin{aligned} h_{ml} &= \lim_{q\to\Omega_l} (q - \Omega_l)\, h_m(q) \\ &= \lim_{q\to\Omega_l} (q - \Omega_l) \frac{\sum_{n=0}^{M-1} \mu_{m,n} q^n}{\prod_{n=1}^{M} (q - \Omega_n)} \\ &= \lim_{q\to\Omega_l} \frac{\sum_{n=0}^{M-1} \mu_{m,n} q^n}{\prod_{n\neq l=1}^{M} (q - \Omega_n)} \\ &= \frac{\sum_{n=0}^{M-1} \mu_{m,n} \Omega_l^n}{\prod_{n\neq l=1}^{M} (\Omega_l - \Omega_n)} . \end{aligned} \tag{3.63}$$

and

$$\begin{aligned}\dot{h}_{ml} &= \lim_{q\to\Omega_l}\frac{d}{dq}\left[(q-\Omega_l)\,h_m(q)\right]\\ &= \lim_{q\to\Omega_l}\left[h_m(q)-(q-\Omega_l)\,\frac{d}{dq}h_m(q)\right]\\ &= -h_{ml}\sum_{n\neq l=1}^{M}\frac{1}{\Omega_l-\Omega_n}+\frac{\sum_{n=1}^{M-1}\mu_{m,n}n\Omega_l^{n-1}}{\prod_{n\neq l=1}^{M}(\Omega_l-\Omega_n)}\end{aligned} \tag{3.64}$$

We are now in a position to calculate the residues of Eqs.3.61 and 3.62. To do this, we note that for a second order pole, we can use the following relation:

$$\mathrm{Res}\left[y(z),z-z_0\right]=\lim_{z\to z_0}\frac{d}{dz}\left((z-z_0)^2\,y(z)\right), \tag{3.65}$$

where the function $y(z)$ has a pole at z_0. We begin with Eq. 3.61

$$\begin{aligned}A_{m_1m_2}(t) &= e^{-i\phi}\sum_{l=1}^{M}\mathrm{Res}\left[qe^{-i\phi}h_{m_1}(qe^{-i\phi})h_{m_2}(qe^{-i\phi})F(q|a+it|),q=\Omega_le^{i\phi}\right]\\ &= e^{-i\phi}\sum_{l=1}^{M}\lim_{q\to\Omega_le^{i\phi}}\frac{d}{dq}\left[qe^{-i\phi}\,(q-\Omega_l)^2\,h_{m_1}(qe^{-i\phi})h_{m_2}(qe^{-i\phi})F(q|a+it|)\right].\end{aligned} \tag{3.66}$$

Now we can move the $\lim_{q\to\Omega_le^{i\phi}} d/dq$ operators into the equation and, by the chain rule, obtain

$$\begin{aligned}A_{m_1m_2}(t) = {}& e^{-i\phi}\sum_{l=1}^{M}\mathrm{Res}\left[q^{-i\phi}h_{m_1}(qe^{-i\phi})h_{m_2}(qe^{-i\phi})F(q|a+it|),q=\Omega_le^{i\phi}\right]\\ &= e^{-i\phi}\sum_{l=1}^{M}\Bigg[\lim_{q\to\Omega_le^{i\phi}}\left(\frac{d}{dq}qe^{-i\phi}\,(q-\Omega_l)\,h_{m_1}(qe^{-i\phi})\,(q-\Omega_l)\,h_{m_2}(qe^{-i\phi})F(q|a+it|)\right)\\ &\quad+\lim_{q\to\Omega_le^{i\phi}}\left(qe^{-i\phi}\frac{d}{dq}\,(q-\Omega_l)\,h_{m_1}(qe^{-i\phi})\,(q-\Omega_l)\,h_{m_2}(qe^{-i\phi})F(q|a+it|)\right)\\ &\quad+\lim_{q\to\Omega_le^{i\phi}}\left(qe^{-i\phi}\,(q-\Omega_l)\,h_{m_1}(qe^{-i\phi}\frac{d}{dq}\,(q-\Omega_l)\,h_{m_2}(qe^{-i\phi})F(q|a+it|)\right)\\ &\quad+\lim_{q\to\Omega_le^{i\phi}}\left(qe^{-i\phi}\,(q-\Omega_l)\,h_{m_1}(qe^{-i\phi}\,(q-\Omega_l)\,h_{m_2}(qe^{-i\phi})\frac{d}{dq}F(q|a+it|)\right)\Bigg].\end{aligned} \tag{3.67}$$

We should take note of difference between the derivative in the third line of Eq. 3.67 and the definition of $\dot{h}_{ml}$ in Eq. 3.64. Thus, we perform a change of variables for the equation

$$\lim_{q\to\Omega_le^{i\phi}}\frac{d}{dq}\,(q-\Omega_l)\,h_m(qe^{-i\phi}) \tag{3.68}$$

and let

$$\begin{aligned}\frac{d}{dq} &= \frac{d\bar{q}}{dq}\frac{d}{dq} \\ &= e^{-i\phi}\frac{d}{d\bar{q}}\end{aligned} \tag{3.69}$$

Eq. 3.68 becomes

$$\begin{aligned}\lim_{q\to\Omega_l e^{i\phi}} \frac{d}{dq}\left(q-\Omega_l\right)h_m(qe^{-i\phi}) &= \lim_{\bar{q}\to\Omega_l} e^{-i\phi}\frac{d}{d\bar{q}}\left(\bar{q}e^{i\phi}-\Omega_l e^{i\phi}\right)h_m(\bar{q}) \\ &\lim_{\bar{q}\to\Omega_l}\frac{d}{d\bar{q}}\left(\bar{q}-\Omega_l\right)h_m(\bar{q}) \\ &= h_{ml}.\end{aligned} \tag{3.70}$$

We can use the same procedure outlined in Eq.3.69 for those terms that do not include the d/dq derivative and we find that

$$\lim_{q\to\Omega_l e^{i\phi}}\left(q-\Omega_l\right)h_m(qe^{-i\phi}) = e^{i\phi}h_{ml} \tag{3.71}$$

picks up an extra phase factor not cancelled out by the derivative. For the derivative of $F(q|a+it|)$ we note, firstly, that $F(z) = e^{-z}\Gamma(0,-z)$ and, secondly, that $\frac{d}{dz}\Gamma(0,z) = -e^{-z}/z$. Thus,

$$\begin{aligned}\lim_{q\to\Omega_l e^{i\phi}}\frac{d}{dq}\left(F(q|a+it|)\right) &= \lim_{q\to\Omega_l e^{i\phi}}\frac{d}{dq}\left(\exp\left(-q|a+it|\right)\Gamma(0,-q|a+it|)\right) \\ &= -e^{-i\phi}\left[(a+it)F\left(\Omega_l(a+it)\right)+\frac{1}{\Omega_l}\right].\end{aligned} \tag{3.72}$$

In the last step of the above equation we used $e^{i\phi}|a+it| = (a+it)$. Using the these results we find that

$$\begin{aligned}A_{m_1m_2}(t) &= e^{-i\phi}\sum_{l=1}^{M}\mathrm{Res}\left[q^{-i\phi}h_{m_1}(qe^{-i\phi})h_{m_2}(qe^{-i\phi})F(q|a+it|), q=\Omega_l e^{i\phi}\right] \\ &= \sum_{l=1}^{M}\Bigg[h_{m_1l}h_{m_2l}F(\Omega_l(a+it)) + \Omega_l F(\Omega_l(a+it))\left[\dot{h}_{m_1l}h_{m_2l}+h_{m_1l}\dot{h}_{m_2l}\right] \\ &\quad -\Omega_l(a+it)h_{m_1l}h_{m_2l}F(\Omega_l(a+it)) - h_{m_1l}h_{m_2l}\Bigg].\end{aligned} \tag{3.73}$$

For the second, much simpler residue we needed to calculate in Equation (3.15) we find that

$$\begin{aligned} B_m(t) &= e^{-i\phi} \sum_{l=1}^{M} \mathrm{Res}\left[h_{m_1 l}(qe^{-i\phi})F(q|a+it|), q = \Omega_l e^{i\phi}\right] \\ &= \sum_{l=1}^{M} \lim_{q\to\Omega_l e^{i\phi}} \left(\left(q - \Omega_l e^{i\phi}\right) h_{m_1 l}(qe^{-i\phi})F(q|a+it|)\right) \\ &= \sum_{l=1}^{M} h_{m_1 l} F(\Omega_l(a+it)). \end{aligned} \tag{3.74}$$

In these formulae, we assume that the poles Ω_l of $h_m(q)$ all have negative real parts, a fact that we have not proven; it is, however, borne out of the numerics. Furthermore, the additional terms that would appear if there were poles with positive real parts would only introduce additional contributions to the Loschmidt echo that decay exponentially over time and are unimportant at large times. These equations form the basis of our numerical study of the full $P(t)$.

3.8 Kondo Length Dependence of the Overlap

We now turn to the Kondo length dependence of the overlap. We first present an heuristic argument by means of which the numerical results we subsequently present may be anticipated. Provided that $\xi \gg a$, we expect ξ to set the scale for dynamics at times sufficiently larger than a. This motivates the scaling ansatz

$$P(t) = Z(\alpha, \alpha', \xi/a) F_{\alpha,\alpha'}\left(\frac{t}{\xi(\alpha, \Delta, a)}\right), \tag{3.75}$$

in which all parameter dependencies have been rendered explicit. If this ansatz is correct, we can extract Z from the long-time result which we calculate in Sec. 3.5 and obtain

$$Z = \left(\frac{2\pi\xi}{L}\right)^{-\beta/2} Q. \tag{3.76}$$

Now, consider the behaviour at times short compared to ξ. We expect the degrees of freedom that are relevant in this regime to be ignorant of the physics at the Kondo scale. For large $J_\parallel$, that is, small α, we can analytically show using the $M = 1$ expansion that for $a \ll t \ll \xi$,

$$P(t) = C\left(\frac{it}{a}\right)^{-\chi/2}, \tag{3.77}$$

with $\chi = (\varphi/\pi - \varphi'/\pi)^2 = (\sqrt{\alpha} - \sqrt{\alpha'})^2/2$ and C independent of ξ. We present this derivation now.

3.8.1 Analytical Results at Small α

Assuming that the ansatz in Eq. 3.75 is true, we analytically show for small α the explicit form of $P(t)$ in the regime where $a \ll t \ll \xi$. In the limit of small α, the $M = 1$ truncation becomes exact. (This is nothing but the SH ansatz discussed in Chapter 2.) For $M = 1$, there is only one variational parameter Ω_1. Its optimal value is $-\Delta_R$, where Δ_R satisfies

$$\begin{aligned} \Delta_R &= \Delta \langle f_1 | f_1 \rangle \\ &= \Delta \exp\left(-\alpha A_{11}(0)\right) < \Delta, \end{aligned} \tag{3.78}$$

and the Kondo length is

$$\xi = \frac{\sqrt{\alpha}}{\pi \Delta_R}. \tag{3.79}$$

For the $A_{11}(t)$ and $B_1(t)$ we obtain

$$A_{11}(t) = \left[1 + \Delta_R(a + it)\right] F\left(-\Delta_R(a + it)\right) - 1 \quad \text{and} \tag{3.80a}$$

$$B_1(t) = F\left(-\Delta_R(a + it)\right), \tag{3.80b}$$

and for $P(t)$ we obtain

$$P(t) = \left(\frac{it}{a}\right)^{-\alpha'/2} \exp\left[\frac{\alpha}{2}\left(A_{11}(t) - A_{11}(0)\right) - \sqrt{\alpha\alpha'}\left(B_1(t) - B_1(0)\right)\right]. \tag{3.81}$$

Provided that Δ is sufficiently smaller than $1/a$, we have $\Delta_R a, \Delta_R t \ll 1$ in the regime $a \ll t \ll \xi$ and we can expand $F\left(-\Delta_R(a + it)\right)$ for small arguments using $F(-z) = -\ln(z) - \gamma_E + O(z)$ where $\gamma_E \approx 0.57\cdots$ is the Euler-Mascheroni constant. We then find that $(A_{11}(t) - A_{11}(0)) = (B_1(t) - B_1(0)) = -\ln(1 + it/a)$ independent of ξ, and

$$P(t) = \left(\frac{it}{a}\right)^{-\chi/2} \tag{3.82}$$

with $\chi = \left(\sqrt{\alpha} - \sqrt{\alpha'}\right)$. We note that the same result would be obtained if we took $f_{1n} = \sqrt{\alpha} g_n / 2\omega_n$. In the Kondo language, this corresponds to the initial state

$$|\mathrm{UV}\rangle = \frac{1}{\sqrt{2}}\left(|-\varphi\rangle\,|\uparrow\rangle - |\varphi\rangle\,|\downarrow\rangle\right), \tag{3.83}$$

verifying our assumption. Here, $|\pm\varphi\rangle$ represents a non-interacting Fermi sea in which electrons undergo phase shifts that depend on their spin direction, such that, at the Fermi energy, these phase

shifts equal $\pm\varphi/2$ and $\mp\varphi/2$ for spin-up and spin-down electrons, respectively.

This is the same behaviour as we would have obtained if before the quench we had $J_\perp$ and hence $\xi = \infty$. Our analytical argument, however, breaks down at larger α. Let us nonetheless assume that a short-time power-law of the form Eq. 3.77 holds for arbitrary α with a ξ-independent C. Universal scaling according to the ansatz in Eq. 3.75 implies that $P(t)/Z$ depends only on t and ξ in the combination t/ξ. The ξ independence of C then implies that $Z \sim \xi^{-\chi/2}$. Using our analytic expression in Eq. 3.76 for Z, we arrive at the result we want, namely, $Q \sim \xi^{(\beta-\chi)/2}$. We also conclude that the overlap Q scales with the system size as $L^{-\beta/2}$. Since the only other length scale that Q can depend on is a, we reproduce our main result given in Eq. 3.5.

3.9 Numerical Results

In the following section we present our numerical results based on the coherent-state expansion. We note that a powerful extension of the technique has been developed to deal with general time-dependent problems [64, 65]. However, due to the simple form of the post-quench Hamiltonian, no sophisticated techniques are needed here, once the initial state is expressed in terms of bosons. We will use the numerical data of Ref. [61]; these data were obtained by simulated annealing for an expansion truncated to $M = 7$ terms at most. In Ref. [61], multiple checks were done to verify that numerical convergence is satisfactory. We estimate that the error in $P(t)$ is at most on the order of 1% at large times and less at shorter times. For a given α, we have data for ξ/a ranging between 1 and 2 decades, with the shortest ξ an order of magnitude larger than the short-distance cut-off a. For each of the 50 combinations of (α, Δ) at which data was taken, we calculated the Loschmidt and the scaling factor, Z, for quenches to various $\alpha' \in [0, 1.5]$. Further details are provided in Appendix A.

Using Eq. 3.56 we numerically calculate $P(t)$ for a range of values of $\alpha \in [0, 1.5]$, $\alpha' \in [0.3, 0.9]$, and $\Delta \in [0.156, 0.305]$ in steps of 0.025. The choice of these ranges is motivated later. As an example of the Loschmidt echo's behaviour, we plot the unscaled $|P(t)|$ vs t in units of a in Fig. 3.1 for with a fixed value of $\alpha = 0.85$ and $\alpha' = \{0, 0.1, 0.3, 0.5\}$ and various values of Δ. The long-time behaviour corresponds to a decay $t^{-\alpha'/2}$ observed in previous studies. In Fig. 3.1(A) we observe that, at long-times, the Loschmidt echo does not decay to zero when we quench from a fixed α to $\alpha' = 0$. However, as we increase the size of α', as shown in Figs. 3.1(B), (C), and (D), the echo does indeed decay to zero. We also observe that an increase in Δ/a results in more rapid decay of $|P(t)|$.

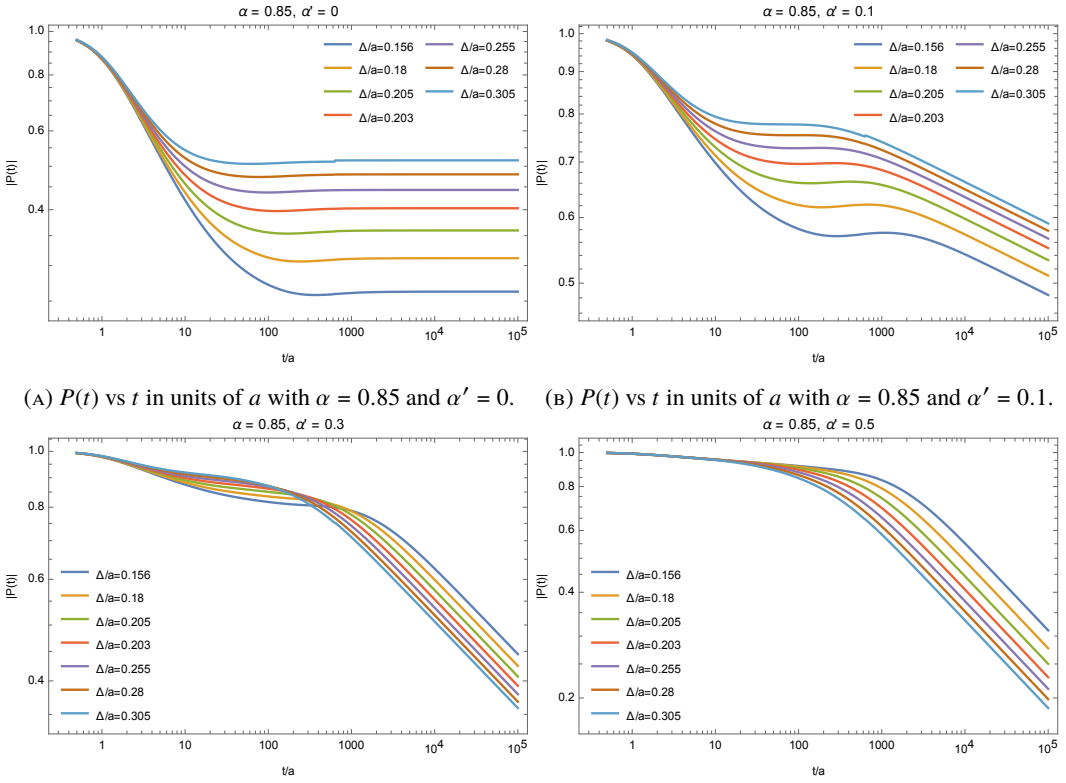

(A) $P(t)$ vs t in units of a with $\alpha = 0.85$ and $\alpha' = 0$.

(B) $P(t)$ vs t in units of a with $\alpha = 0.85$ and $\alpha' = 0.1$.

(C) $P(t)$ vs t in units of a with $\alpha = 0.85$ and $\alpha' = 0.3$.

(D) $P(t)$ vs t in units of a with $\alpha = 0.85$ and $\alpha' = 0.5$.

FIGURE 3.1: The amplitudes of the Loschmidt echo vs time in units of a. The various panels are calculated using Eq. 3.56 making use of the expression for Eq. 3.58 for $\alpha = 0.85$ and various values of α'. The different curves correspond to different values of $\Delta/a \in \{0.156, 0.18, 0.205, 0.23, 0.255, 0.28, 0.305\}$.

niversality

Now we wish to test the scaling ansatz in Eq. 3.75. To do so, we must calculate the Kondo length and scaling factor Z for the parameters of interest. In terms of the ground state parameters, these are given by

$$\begin{aligned} Z &= \left(\frac{2\pi\xi}{L}\right)^{-\alpha'/2} |\langle \alpha', 0 | \alpha, \Delta \rangle|^2 \\ &= \left(\frac{\xi}{a}\right)^{-\alpha'/2} \left| \sum_{m=1}^{M} \exp\left[-\frac{\alpha}{4} A_{mm}(0) + \frac{\sqrt{\alpha\alpha'}}{2} B_m(0) \right] \right|^2, \end{aligned} \tag{3.84}$$

and we express the Kondo length, ξ, as is done in Ref. [58], as

$$\xi = \frac{\sqrt{\alpha}}{2} \sum_{m_1, m_2} c_{m_1} c_{m_2} \left[h_{m_1}(0) + h_{m_2}(0) \right] \langle f_{m_1} | f_{m_2} \rangle . \tag{3.85}$$

Fig. 3.2 shows the result for the Kondo length where we calculate the Kondo length ξ using the expression in Eq. 3.85. This is shown in Fig. 3.2 where we plot ξ vs Δ both in units of a for each of the parameter values of α and Δ for which the ground state of $H_{\alpha,\Delta}$ is numerically calculated. On a log-log scale we observe a decreasing linear relationship between the two where lines connect data points corresponding to the same α where we set $a = 1$.

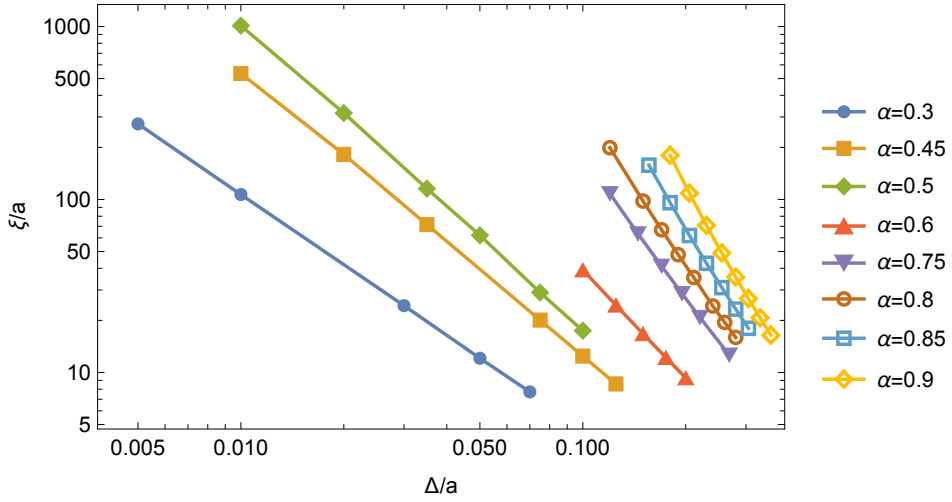

FIGURE 3.2: The Kondo length ξ vs Δ both in units of a. For each line, the ground state of $H_{\alpha,\Delta}$ is numerically calculated each of the parameter values of α and Δ.

Using the calculated Kondo lengths and scaling factors, we plot the scaled function of $P(t)/Z$ vs t/ξ in the main panels of Fig. 3.3. Different panels correspond to the different values of α' and we use the same values of Δ/a as before with the insets showing the corresponding unscaled plots. Additional plots for the other values of α and α' are found in Appendix A. In all panels in Fig. 3.3 we see excellent universal scaling in accordance with the ansatz in Eq. 3.75 in the short- and long-time regime. This is shown by the alignment of scaled echoes onto one another and we note that ξ and Z are not determined by fitting as is done frequently when one looks for universality.

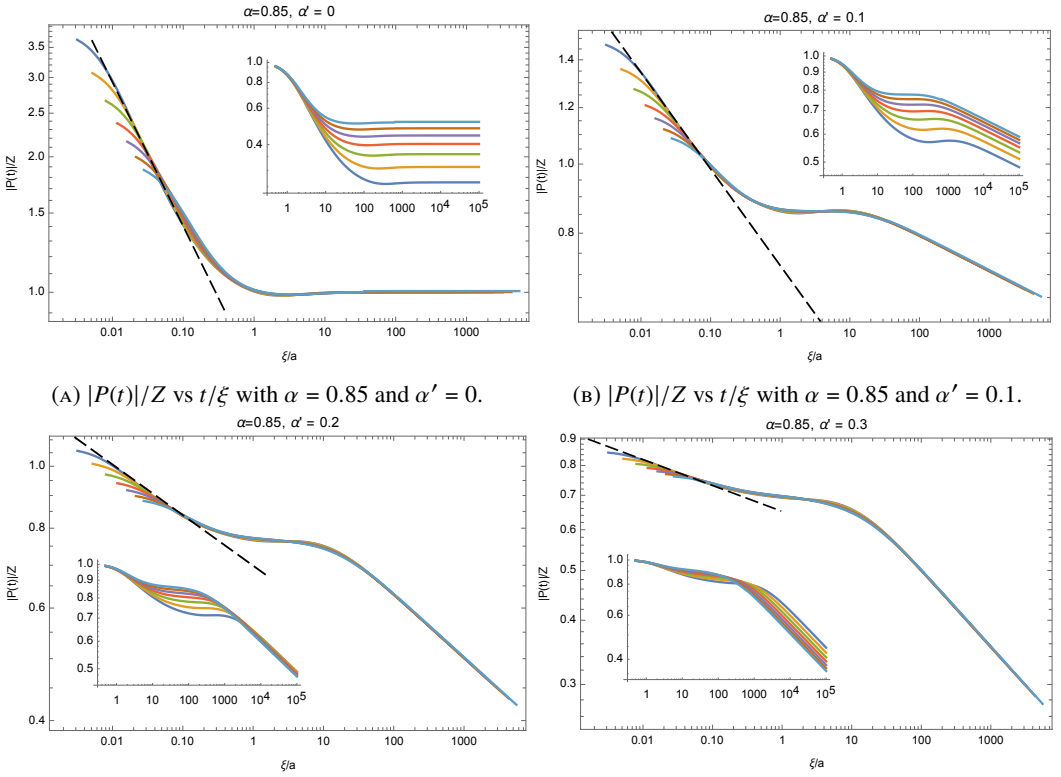

(A) $|P(t)|/Z$ vs t/ξ with $\alpha = 0.85$ and $\alpha' = 0$.

(B) $|P(t)|/Z$ vs t/ξ with $\alpha = 0.85$ and $\alpha' = 0.1$.

(C) $|P(t)|/Z$ vs t/ξ with $\alpha = 0.85$ and $\alpha' = 0.3$.

(D) $|P(t)|/Z$ vs t/ξ with $\alpha = 0.85$ and $\alpha' = 0.5$.

FIGURE 3.3: The amplitudes of the scaled Loschmidt echoes vs time in units of Z and ξ given in Eqs. 3.84 and 3.85, respectively. The insets show the corresponding unscaled data vs time in units a. The sloped dashed lines represent the power-law decay for $|P(t)|/Z = C(t/a)^{-\xi/2}$, with C and ξ obtained by fitting to amplitude data for $t < 10^{-1}\xi$.

We observe two algebraic decays in the regimes $t \ll \xi$ and $t \gg \xi$. For short-time behaviour of the Loschmidt echo we see that $|P(t)|/Z$ follows a short-time power-law in the time window $a < t < \xi$ and that for the various values of Δ/a, $|P(t)|$ is relatively independent of Δ/a at small t. This is seen in in Fig. 3.3(A) where, at short-times, the echoes with different values of Δ/a decay at the same rate and, as a result, the echoes align with one another. A similar behaviour is observed for different values of α' where at short-decay times, $|P(t)|/Z$ is independent of Δ. Additional results for different values of α and α' are found in Appendix A. We can extract the short-time power-law exponent from the scaled echoes. This is represented by the sloped dashed line which represents the power-law decay for $|P(t)|/Z = C(t/a)^{-\xi/2}$, with C and ξ obtained by fitting to amplitude data for $t < 10^{-1}\xi$. These results are compared to the approximate analytical result $\chi = (\sqrt{\alpha} - \sqrt{\alpha'})^2/2$. This is shown in Fig. 3.4 where solid lines represent the analytical expression of χ and the dotted lines are the extracted power-laws exponents at short times. Below $\alpha \simeq 0.5$ we find good agreement with the approximate analytical result. At small α, modes with $1/\xi \ll \omega_n \ll 1/a$ are associated with

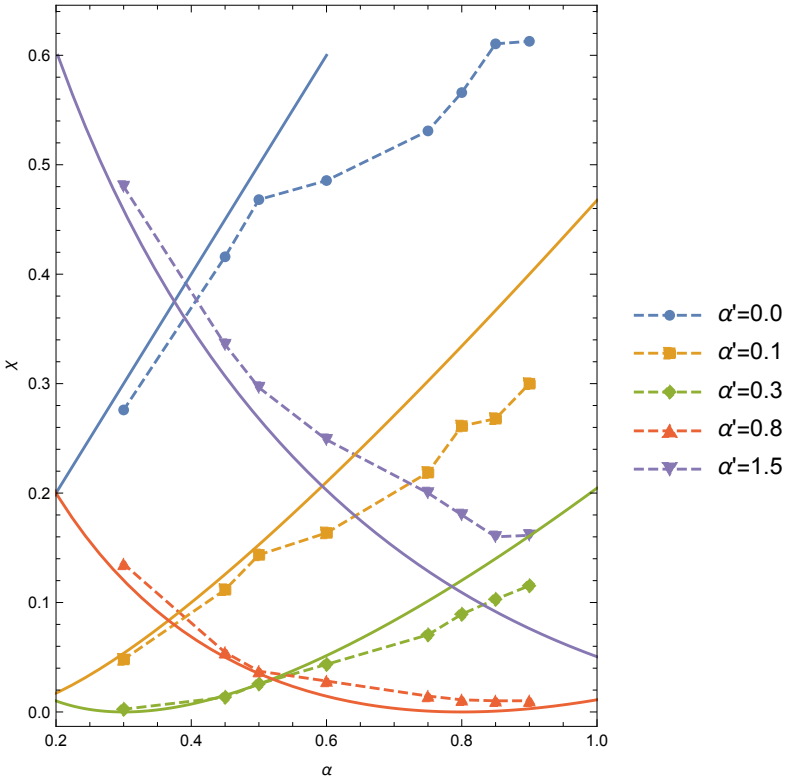

FIGURE 3.4: Symbols: The short-time power-law exponent χ defined in Eq. 3.77 at five different values of α' as extracted from our numerical $P(t)$ data. Curves: The small α prediction $\chi = (\varphi/\pi - \varphi'/\pi)$.

displacements $f_{mn} \simeq \sqrt{\alpha} g_n / 2\omega_n$, as if $\Delta = 0$. This allows for a straightforward explanation of the power-law in terms of the response of non-interacting spin-up and spin-down Fermi seas to a local quench. At larger α, $|P(t)|$ still obeys a short-time power-law, but the power-law exponent deviates from that of the approximate analytical result. In this case, we find numerically that the non-interacting Fermi sea behaviour of f_{mn} only sets in close to the ultraviolet cut-off $1/a$. If a non-interacting Fermi sea explanation is possible in this regime, the coherent-state expansion does not make this manifest. When $\alpha = \alpha'$ the analytical result of Refs. [28, 29] is that $\chi = 0$. The largest deviation we found from this is at $\alpha = \alpha' = 0.8$, where $\chi = 0.018$. We believe this is a small finite-size error, and note that we unambiguously find that χ is minimal when $\alpha = \alpha'$. We also note oscillatory behaviour that might be a numerical error in the results for $\alpha' = 0, 0.1$, and $\alpha > 0.6$. The same fluctuations are not seen at other α' values. Given that the same ground state data was used for all α', we attribute any error that is present to the numerical extraction of the power-law exponent rather than to errors in the ground state data.

With the assumption verified that in the regime $a \ll t \ll \xi$ the Loschmidt echo is both independent of Δ and obeys a power-law $t^{-\chi/2}$, our conclusion regarding the power-law dependence of the ground

state overlap on the Kondo length must be correct. We now calculate the ground state to grounds state overlap $(2\pi a/L)^{-\beta/2}\,|\langle\alpha',0|\alpha,\Delta\rangle\,|^2$ directly by adapting the result for Z in Eq. 3.84. Indeed we find that at a fixed α and α' (that is, a fixed $J_{\|}$ and $J'_{\|}$ in the Kondo language) $Q = |\langle\alpha',0|\alpha,\Delta\rangle\,|^2$ has a power-law dependence on ξ, that is

$$|\langle\alpha',0|\alpha,\Delta\rangle\,|^2 \propto \xi^{\eta}. \tag{3.86}$$

As as example, in Fig. 3.5 we show this power-law dependence for results for $\alpha = 0.85$ and various α'. In each case, we observe the expected linear dependence when plotting $(2\pi a/L)^{-\beta/2}\,|\langle\alpha',0|\alpha,\Delta\rangle\,|^2$ vs ξ/a noting that a we increase α' there is an observed increase in gradient.

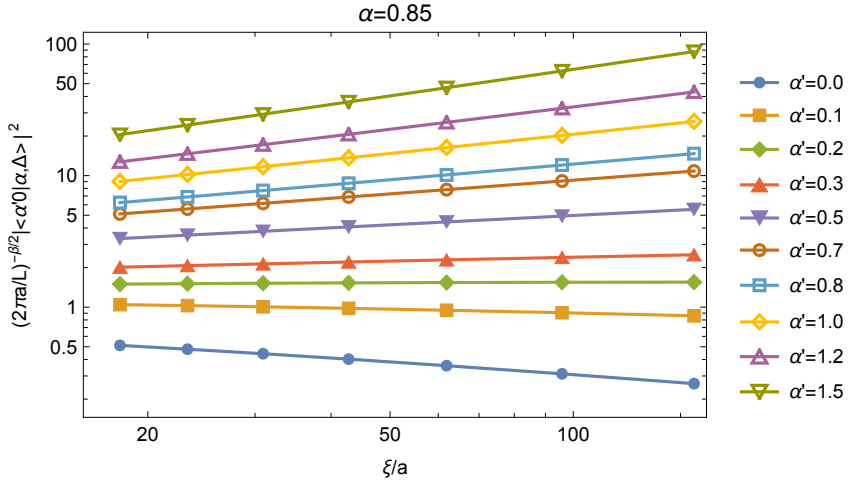

FIGURE 3.5: Symbols: The ground state to ground state overlap squared $|\langle\alpha',0|\alpha,\Delta\rangle\,|$ vs the Kondo length ξ for various values of α' for a fixed $\alpha = 0.85$. Lines: The power-law $|\langle\alpha',0|\alpha,\Delta\rangle\,| = G\xi^{\eta}$, with G and η obtained by fitting the data with $\xi \gtrapprox 25a$.

The data in Fig. 3.5 is now used to compare the power-law exponent in Eq. 3.86. This is done by extracting the gradient and comparing it to that of the short-time power-law exponent χ of the scaled Loschmidt echoes in Figs. 3.3 for the various values of α'. This relationship is shown in Fig 3.6 where we see very good agreement with our prediction that $\eta = (\beta - \chi)/2$. The inset displays an enlarged view of the clustered $\alpha' = 0.5$ data. The largest deviations are seen at $\alpha' = 0$ and $\alpha > 0.6$. As we noted already, the extracted values of the exponent χ for these data points may contain some noise. However, even here, the largest deviation between the extracted η values and the line representing $\eta = (\beta - \chi)/2$ is 5%. For the other data sets, the deviation is of the order of a percent at most.

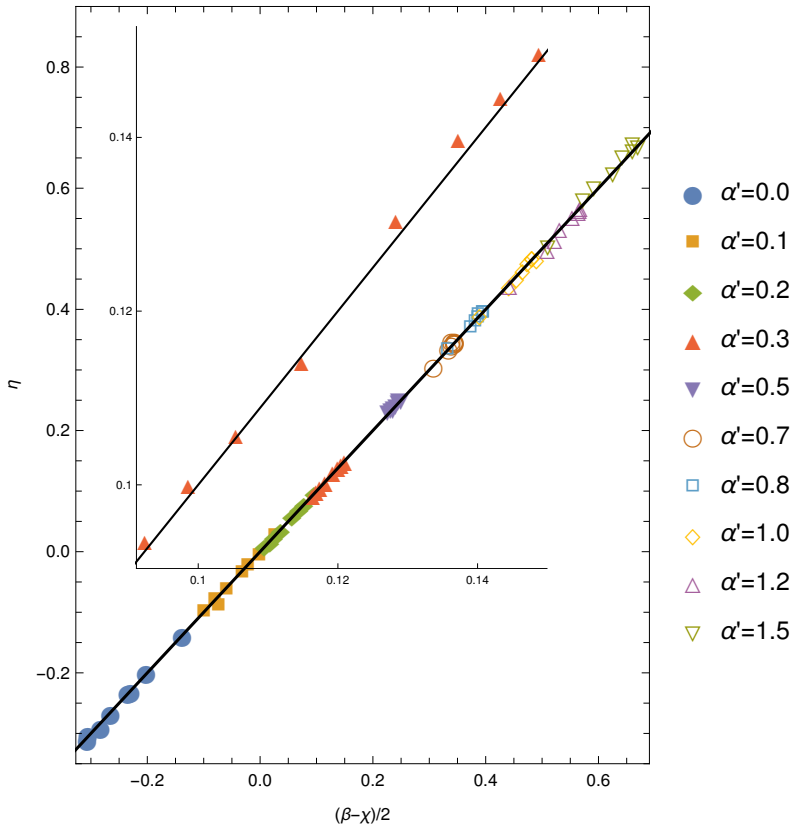

FIGURE 3.6: Symbols: Each data point corresponds to a fixed value of α and β. The x and y coordinates of each point are respectively $(\beta - \xi)/2$, with a short-time power-law exponent ξ cf. Eq. 3.86, as extracted from the data in such as that plotted in Fig. 3.5. Black lines: The heuristic prediction $\eta = (\beta - \chi)/2$. Inset: An enlarged view of the clustered $\beta = 0.3$ data.

3.10 Conclusion

For the Kondo model, we have demonstrated that the Loschmidt echo and the overlap between ground states before and after the quench are connected not only via dynamics at long times, but also via dynamics at short times. Our main results are contained in Eqs. 3.4 and 3.5 and can be summarized as follows. If one subtracts the slope seen at short times in the log-log plot of the Loschmidt echo (as shown in the main panels in Fig. 3.3), from the slope seen at long times, one obtains the slope seen in the log-log plot of the ground state to ground-state overlap squared versus the Kondo length (Fig. 3.5). The overlap's dependence on the emergent length scale ξ thus elegantly encodes information about both IR and UV dynamics. Apart from Anderson's orthogonality theorem, the other essential ingredients that produced this result were the universal scaling and power-law behaviour of the Loschmidt echo at short times. In light of this, it may be interesting to revisit results for the overlap in studies of other systems that have focused on system size dependence to see if similar connections exist.

Appendix A

Further Numerical Results

In this appendix, we provide the numerical results in addition to those presented in Chapter 3. In Figs. A.1 and A.2, we plot the rest of the numerical Loschmidt echo data for $\alpha = 0.85$. These plots provide readers with an intuitive understanding of how the Loschmidt echo depends on different values for α'. Additionally, they show the quality of scaling collapse and the existence of an ultraviolet power law throughout the parameter space.

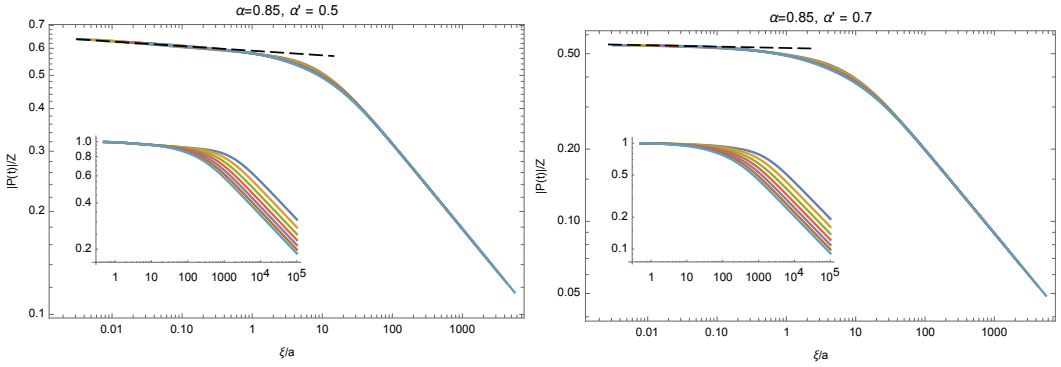

(A) $|P(t)|/Z$ vs t/ξ with $\alpha = 0.85$ and $\alpha' = 0.5$.

(B) $|P(t)|/Z$ vs t/ξ with $\alpha = 0.85$ and $\alpha' = 0.7$.

FIGURE A.1: The amplitudes of the scaled Loschmidt echoes vs time in units of Z and ξ given in Eqs. 3.84 and 3.85, respectively. The insets show the corresponding unscaled data vs time in units a. The sloped dashed lines represent the power-law decay for $|P(t)|/Z = C(t/a)^{-\xi/2}$, with C and ξ obtained by fitting to amplitude data for $t < 10^{-1}\xi$.

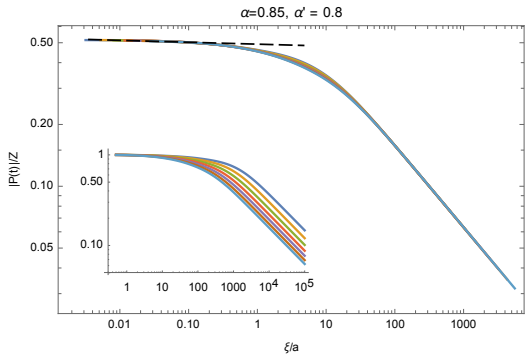

(A) $|P(t)|/Z$ vs t/ξ with $\alpha = 0.85$ and $\alpha' = 0.8$.

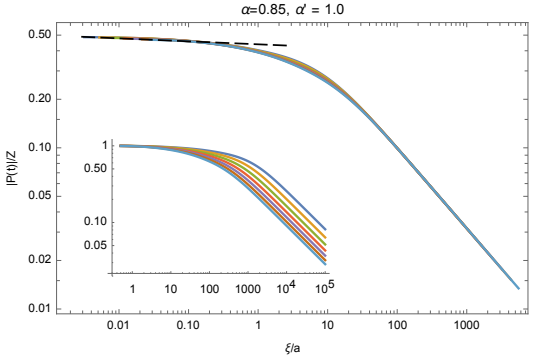

(B) $|P(t)|/Z$ vs t/ξ with $\alpha = 0.85$ and $\alpha' = 1.0$.

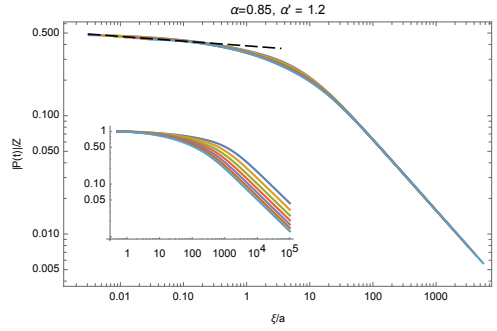

(C) $|P(t)|/Z$ vs t/ξ with $\alpha = 0.85$ and $\alpha' = 1.2$.

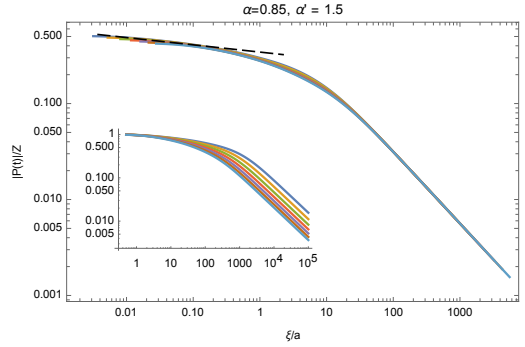

(D) $|P(t)|/Z$ vs t/ξ with $\alpha = 0.85$ and $\alpha' = 1.5$.

FIGURE A.2: The amplitudes of the scaled Loschmidt echoes vs time in units of Z and ξ given in Eqs. 3.84 and 3.85, respectively. The insets show the corresponding unscaled data vs time in units a. The sloped dashed lines represent the power-law decay for $|P(t)|/Z = C(t/a)^{-\xi/2}$, with C and ξ obtained by fitting to amplitude data for $t < 10^{-1}\xi$.

Part II

Chapter 4

Introduction

In Chapter 4, we introduce the formation of rogue waves in the context of oceanography, as readers are likely to be familiar with their occurrences in this context. We then discuss how linear mechanisms can give rise to rogue waves. However, we note that for theoretical predictions to coincide with experimental observations, nonlinearity in the models that describe the system is necessary. We identify the nonlinear Schrödinger equation as the most commonly studied of these nonlinear models and we emphasise its universality by showing that the same model is used when describing rogue wave formation in the ocean as well as optical rogue waves in discrete optical waveguide arrays. We then introduce the unstable nonlinear Schrödinger equation, which we study in Chapter 5, and we discuss how it has been realised in real discrete optical waveguide arrays, particularly for its role of modelling random fluctuations in the system. Finally, we shift our focus to modulation instability and discuss how this leads to the formation of rogue waves in many different physical systems.

4.1 A Brief History of Rogue Waves in the Ocean

Oceanic rogue waves, sometimes referred to as freak or giant waves, are rare, large amplitude, localised surface waves that appear suddenly and then disappear almost immediately [66]. Their amplitudes are often reported to exceed 15 meters in height from their crest to their trough [67]. Their destructive nature has resulted in the tragic loss of human lives and poses a threat to ships and on- and off-shore structures. Rogue waves have been known to mariners for centuries with horrifying tales dating back

to the 1400s [67]. At that time, their causes were unknown and their reputation became part of marine folklore.

Despite the continued development of models and mechanisms that describe their profiles and predict their occurrences, the lack of quantitative data kept the existence of rogue waves shrouded in mystery well into the last century [68]. That was until the first significant measurement of a rogue wave was made from the Draupner Jacket platform off the cost of Norway in 1995 [69]. The crest mean of this wave measured 18.6 m while its height measured 25.6 m. This sparked interest from the scientific community as it verified many of the theoretical predictions put forward decades earlier. In more recent times, the measurement of rogue waves is done with sophisticated equipment such as buoys equipped with altimeters and pressure gauges that track the surface elevation of the ocean [70]. Today, the existence of rogue waves is no longer debated and research into these fascinating phenomena continues to develop into many varied fields [71].

To classify a rogue wave event such as the Draupner wave, oceanographers often make use of a rather simple parameter referred to as the abnormality index [72]. This index is the ratio of the rogue wave height, H_{RW}, to it's significant wave height, H_{Sig}. The latter is defined as the average wave height among one third of the highest waves. This is usually measured over a longer period of time relative to the time the rogue wave event occurs. The abnormality index is given by

$$AI = \frac{H_{\mathrm{RW}}}{H_{\mathrm{Sig}}} \geq 2. \tag{4.1}$$

The value on the right hand side of Eq. 4.1 often varies and has been known to range between 1.5 and 3 [73]. This has drawn criticisms, which state that the index does not include weather conditions or other conditions such as wind swept waves [74]. However, the general consensus is that an AI larger than 2 identifies extremely large amplitude waves systems that can only be classified as rogue waves [72].

In general, one can obtain likelihoods and other statistical information about oceanic waves from a simple linear model [75]. Here, it is assumed that the ocean waves are comprised of random superpositions of waves which vary in their frequencies, directions, and phases. Under this assumption, the wave components are no longer correlated and the elevation of the waves follows a normal distribution, while the wave envelope follows a skewed distribution which is often a Rayleigh distribution. Furthermore, for linear waves which fall within a narrow banded spectrum, the wave height is assumed to be twice the crest height. The probability of observing a rogue wave exceeding a

particular height falls within the tail end of the skewed distribution [71]. However, measurements of rogue waves indicate that they occur more frequently than this distribution suggests [76–79].

The most commonly studied linear mechanisms known to result in oceanic rogue waves include (i) geometrical and spatial focusing of waves, (ii) wave-current interaction, and (iii) wind interactions that result in the focusing of waves. In case (i), straight crest ocean wave fronts become curved and are transformed into circular or cylindrical ones. This is either due to the varying sea floor topography, or due to the fact that the ocean waves are reflected from complex coastal line structures. These ocean waves are refracted similar to their optical counterparts in an optical lens and, at the focal point, their heights are amplified. In case (ii), when travelling waves meet with a current travelling in the same direction, there is a transfer of energy between the two as they interact constructively resulting in a larger wave [80]. In case (iii), a non-uniform wind profile blowing over the surface of the ocean results in an energy transfer and larger waves form [81, 82]. This process is often coupled with changes in atmospheric pressure [83] and also includes other parameters such as wind speed and the fetch of the wind. In this thesis we focus on a specific linear effect that is included in our system, which will increase the instability of the system. For hydrodynamic systems, the effect comes as a result of the surface tension between to fluids of different densities. More specifically, a less dense fluid that on top of a denser fluid increases the overall instability of the system caused by gravity, because of their mutual interaction at the interface [84].

Though linear mechanisms do result in rogue wave formation, their associated models often fail to predict the observed heights of rogue waves [74]. This motivates the use of nonlinear models, which predict wave amplitudes that are more consistent with experimental measurements and they predict wave heights that are more consistent with Eq. 4.1. Moreover when nonlinear models are utilized, the likelihoods of rogue wave formation are still shown to have a Rayleigh distribution, which is also consistent with experimental observations [85]. The most commonly studied of all models is the nonlinear Schrödinger equation (NLSE), which not only addresses the inconsistencies of the linear models, but it also sheds light on a multitude of other nonlinear phenomena like solitons, which we will discuss later. These phenomena were initially thought to be unrelated. However, they are now identified as forming part of a hierarchy of solutions known to exist for the NLSE [86]. We will discuss the most commonly know solutions to the NLSE later in this chapter.

4.2 The Nonlinear Schrödinger Equation

Let us first introduce the NLSE for ocean waves. To this end, we introduce it, as is often done [1, 87], in the case of a deep (or infinite depth) water system. We will assume that the waves under consideration are quasi-monochromatic and that the surface elevation is slowly varying. A function that can describe the resulting surface elevation in terms of a spatial co-ordinate x and a temporal co-ordinate t is given by

$$\eta(x,t) = \frac{1}{2}\left(A(x,t)\exp\left(ik_0x - i\omega_0 t\right) + \text{c.c.}\right), \tag{4.2}$$

where c.c. stands for complex conjugate, k_0 and ω_0 are the wave number and wave frequency of the carrier wave, and $A(x,t)$ is a complex wave envelope determined by a nonlinear model. This nonlinear model can be described by the NLSE and is written as

$$i\frac{\partial A}{\partial x} + i\frac{1}{v_g}\frac{\partial A}{\partial t} - \frac{k_0}{\omega_0^2}\frac{\partial^2 A}{\partial t^2} - k_0^3|A|^2A = 0, \tag{4.3}$$

where $v_g = \partial\omega/\partial k$ is the group velocity, the third term describes the dispersion of the surface elevation, and the forth term is the nonlinear term. Eq. 4.3 describes the evolution of wave trains which is strongly determined by the initial condition. As we show in the next chapter, the nature and occurrences of rogue waves are very sensitive to initial conditions.

By performing a transformation of Eq. 4.3 where $T = t-(1/v_g)x$ and $X = x$, and defining dimensionless quantities $\xi = -k_0^3A_0^2X$ and $\tau = (1/\sqrt{2})\omega_0k_0A_0T$ where A_0 is the initial amplitude of $A(x,t)$, we obtain a dimensionless NLSE in terms of a normalized wave function $\psi(x,t) = A(x,t)/A_0$ given by

$$i\frac{\partial\psi}{\partial\xi} + \frac{1}{2}\frac{\partial^2\psi}{\partial\tau^2} + |\psi|^2\psi = 0. \tag{4.4}$$

Eq. 4.4 is sometimes referred to as the *time* NLSE relating to the second derivative in time in the second term. It can be used to describe the propagation of light waves along an optical fibre, provided that additional parameters are introduced to the terms which characterise certain length and time scales. We will explore this further in Sec. 4.3. For now, we note that in many hydrodynamic experiments [88], the time and position coordinates are swapped in Eq. 4.4. In this case, the equation is then referred to as the *space* NLSE. From a mathematical point of view, the solutions of the space NLSE are identical to those in Eq. 4.4, though the physical interpretations are different. To illustrate concepts relating to nonlinear optical systems one often refers to the time NLSE. However, for our work we make use of the space NLSE and therefore emphasise temporal evolution of the system.

Due to the simplicity and universality of Eq. 4.4, the NLSE is the basis of more complex models and has been utilized in various scientific fields outside of oceanography [89]. This is because of the analogous nature between wave dynamics of ocean waves and a variety of other wave phenomena. Among the most significant of these analogous systems is that of a Bose-Einstein Condensate (BEC) formed in ultra cold vapours [90]. This lead to the discovery of stable, solitary waves, known as *solitons*, that propagate within the nonlinear BEC medium [91]. Like rogue waves, solitons are also solutions to the NLSE [86]. They are well documented [92] and were also first observed in water wave systems. Other analogous systems that display solitons include plasma physics [93], magnetic systems [94], and biological systems where they appear in proteins which result from thermal transitions in membranes [95]. In optics, solitons appear as solitary pulses or beams of light and studies have been conducted in 1D and multidimensional systems. Often these studies are divided up into spatial, temporal, or spatiotemporal categories [89] and they have also been observed in coupled NLSE systems [96]. Let us shift our focus now to the formation of solitons in the context of nonlinear optics, noting that this field has become a playground in which systems such as those described by the NLSE and similar equations can be experimentally realised. We will then discuss a link between the formation of rogue waves and solitons based on the NLSE.

4.3 Nonlinear Optics

The first suggestion that optical solitons could be generated and measured came in the early 1970s [97, 98]. This was based on the idea that there is always a delicate balancing between a term that governs the dispersion of light in a medium and a nonlinear term which leads to a stable, self-focusing light pulse. The self-focusing effect, often referred to as the optical Kerr effect, has been realized experimentally by increasing the refractive index of a nonlinear medium [99]. This effect is relatively weak but can be enhanced through light confinement in the core of optical fibre as well as by ensuring that there is a large propagation distance of light sent through such a system. One field of optics that makes use of this effect is telecommunication [100], where optical solitons are particularly attractive as they could travel vast distances through optical fibres while their wave profile remains undistorted.

To develop an understanding of how light propagates through an optical fibre in a way that leads to nonlinear phenomena, we will describe how the NLSE appears as part of the equation governing such a system. A detailed derivation can be found in Ref. [101]. What we wish to motivate in the following is that the response of the optical fibre to the polarization of the electric field is nonlinear and that it is well approximated by the NLSE.

It is well known that an electromagnetic field propagating through an homogeneous, source-free medium is governed by Maxwell's wave equation which, in an optical fibre, is described by

$$\nabla^2 \vec{E} = -\frac{1}{c^2}\frac{\partial^2}{\partial t^2}\vec{E} - \mu_0 \frac{\partial^2}{\partial t^2}\vec{P}, \tag{4.5}$$

where $\vec{E}$ is the electric field, $\vec{P}$ is the induced polarization, the speed of light in a vacuum is $c = (\mu_0 \epsilon_0)^{1/2}$, and μ_0 and ϵ_0 are the vacuum permeability and vacuum permittivity, respectively. Assuming that the response of the optical fibre to the electric field is local and that it obeys time-reversal symmetry, the total polarisation is expressed by the series expansion

$$\vec{P}(r,t) = \sum_{i=0}^{\infty} \vec{P}^{(i)}(\vec{r},t). \tag{4.6}$$

A term in this series is generally given by

$$\vec{P}^{(i)}(\vec{r},t) = \epsilon_0 \int_{-\infty}^{t} dt_1 \cdots \int_{-\infty}^{t} dt_i \chi^{(i)}(t-t_1,\cdots,t-t_i) \otimes \vec{E}(\vec{r},t_1)\cdots\vec{E}(\vec{r},t_i), \tag{4.7}$$

where χ is the susceptibility related to the materials response to the applied electric field and the symbol"$\otimes$" denotes the tensor product between the applied electric field and the ith order susceptibility tensor. We note that $\chi^{(i)}$ denotes the tenors that are of rank $(i+1)$. The first order term in χ usually dominates. Terms of even order in χ vanish due to inversion symmetry property of the optical medium [99, 102]. The next term in Eq. 4.7 does not vanish and it describes a nonlinear effect due to the anharmonic motion of the bound electrons. This term is third order in $\vec{E}$ and its effect is present in materials such as silica glass gallium arsenide or aluminium gallium arsenide. For this reason many types of optical fibres are manufactured using these materials. The total instantaneous polarization in these materials can then be approximated by

$$\vec{P}(\vec{r},t) = \epsilon_0 \left(\chi^{(1)}_{kl}\vec{E}_l(\vec{r},t) + \chi^{(3)}_{klmn}\vec{E}_l(\vec{r},t)\vec{E}_m(\vec{r},t)\vec{E}_n(\vec{r},t)\right), \tag{4.8}$$

where we use Einstein notation to denote the tensor products.

If the polarization remains constant during the propagation of light along the optical fibre then a function $A(\vec{r},t)$ can be used to approximate a slowly varying quasi-monochromatic electric field [102] of the form

$$\vec{E}(\vec{r},t) = \frac{1}{2}\hat{e}_x \left(F(x,y)A(\vec{r},t)\exp\left(i\beta_0 x - i\omega_0 t\right) + \text{c.c.}\right), \tag{4.9}$$

where β_0 is the wave number, $\hat{e}_x$ is the unit vector of polarization, $F(x,y)$ is the modal distribution,

and $A(\vec{r}, t)$ is the mentioned complex pulse envelope obeying a nonlinear model. For a single fibre mode, assuming no losses in optical intensity or modal distribution, $F(x, y)$ is well approximated by a Gaussian distribution. In general, A need not be a function of $\vec{r}$ and t [101] and it can be assumed that it is only a function of one spatial coordinate, say z, alongside its dependence on t. This case represents a concentrated pulse travelling within an optical fibre with the dispersion only taking place in the direction of propagation. We determine A from

$$\frac{\partial A}{\partial z} + \beta_1 \frac{\partial A}{\partial t} + i\frac{\beta_2}{2}\frac{\partial^2 A}{\partial t^2} - i\gamma\omega_0|A|^2 A = 0, \tag{4.10}$$

where γ is the parameter relating to the optical nonlinearity of the fibre. The parameter $\beta_1 = c/v_g$ and β_2 describes group velocity dispersion. These parameters are related to the wave number, β_0, which, in turn, is related it to the dispersion relation of the material through a propagation constant, $\beta(\omega)$. The latter can be expanded using a Taylor expansion as

$$\beta(\omega) = \sum_{m=0}^{\infty} \frac{1}{m!}(\omega - \omega_0)^m \beta_m, \tag{4.11}$$

with $\beta_m = (d^m\beta/d\omega^m)_{\omega=\omega_0}$ and $m \in \mathbb{N}_0$. Once more, we can transform Eq. 4.10 and describe it in a retarded frame using $T = t - z/v_g$ which yields

$$i\frac{\partial A}{\partial z} - \frac{\beta_2}{2}\frac{\partial^2 A}{\partial T^2} + \gamma|A|^2 A = 0. \tag{4.12}$$

We note that, by setting

$$\xi = \frac{z}{L_{\mathrm{NL}}} \quad \text{where} \quad L_{\mathrm{NL}} = \frac{1}{\gamma P_0}, \tag{4.13a}$$

$$\tau = \frac{T}{T_0} \quad \text{where} \quad T_0 = \sqrt{|\beta_2| L_{\mathrm{D}}}, \tag{4.13b}$$

$$\psi = \frac{A(z,t)}{\sqrt{P_0}}, \tag{4.13c}$$

we obtain the optical counterpart to Eq. 4.4 indicating that the two equations form part of the same universality class of general wave phenomena. In the above equations L_{NL} and L_{D} correspond to nonlinear and dispersion lengths [103], and P_0 is the incident optical power intensity.

In turns our that a negative group velocity dispersion ($\beta_2 < 0$) (in the case of in Eq. 4.10) and the correct choice of γ, results in an optical Kerr effect, which allows for the propagation of bright solitons. During manufacturing, β_2 could be controlled by doping the optical fibre [100] and γ could be enhanced by increasing the refractive index. Moreover, if the length of the optical fibre,

L, is larger than both L_{NL} and L_{D}, defined in Eq.4.13a and Eq.4.13b, respectively, the profile of the soliton should remain unchanged during propagation [104]. This was indeed accomplished in 1980 [105], where bright optical solitons were experimentally observed in a single-mode silica-glass fiber. A proposal for "repeaterless" communication subsequently was proposed after examinations via numerical simulations [106] and these predictions were later realised in a real optical fibre systems with the addition of amplifiers [107]. Since then, various theoretical and experimental breakthroughs have seen propagation distances increase to over 10^6 km with relatively low losses or changes to soliton profiles. A review of the history and technical details of these achievements can be found in [100].

We note that the observation of rogue waves in optical fibres, in contrast to optical solitons, is relatively new with the first optical rogue wave being experimentally observed in 2007 [108]. Since then however, the field branched out into various directions. One of these branches is devoted to the study of discrete optical systems, which we will utilise in our own study on rogue waves. To this end we now introduce discrete optical waveguide arrays and highlight some of the breakthroughs made in this field.

4.4 Discrete Optical Waveguide Arrays

Nonlinear phenomena have been studied in various discrete lattices including optical waveguide arrays [109]. The latter are manufactured from materials that are similar to those in optical fibres and consist of a number of waveguides that are coupled to one another to form an array as in Fig. 4.1. These systems also allow for the experimental verification of various theoretical predictions often originating from basic quantum mechanics. This link between quantum mechanics and optics is based on the equivalence that exists between the Schrödinger equation and a paraxial approximation to the scalar Helmholtz equation [110, 111], where a detailed derivation of this equivalence has been presented before [112] and will not be repeated here.

This equivalence has allowed experimentalists to fabricate and study, for example, a topological phase transition in a bulk system, which has an extra feature of being non-Hermitian [113]. The experimental system comprised of evanescent coupled waveguide arrays, which can be modelled using the tight-binding model to yield discrete Schrödinger equation [114]. The topological model studied was a 1D non-Hermtian dimer, which resembles the Su-Schreiffer-Heeger (SSH) model of polyacetylene [115]. The SSH model is defined in terms of hopping parameters that alternate between

weaker and stronger bonds and it includes topologically distinct phases, which are defined by a topological number: the winding number [116]. The non-Hermiticity of the system was ensured by allowing losses along every other waveguide in the array by fabricating them such that they "wiggle" . The topological phases were demonstrated by propagating light through the bulk for and displaying trivial and non-trivial winding numbers. Other examples of photonic topological insulators have also been realised [117] through coupled waveguide arrays as well as models describing non-relativistic quantum mechanical phenomena [118, 119] and nonlinear systems [120].

For a slowly varying envelope of guided model fields in identical, periodically coupled single-mode waveguide arrays, the mathematical model describing a discrete NLSE was first described in [121, 122]. The corresponding discrete unstable NLSE (UNLSE) consisting of N homogeneous waveguides is given by [123]

$$i\frac{\partial A_m}{\partial z} + \beta\left(A_{m+1} - 2A_m + A_{m-1}\right) + \gamma|A_m|^2 A_m + \Gamma_m A_m = 0, \tag{4.14}$$

where the second term Eq. 4.14 is a nearest neighbour interaction; β and γ are the coupling and the nonlinear coefficients, respectively; $A_m(z)$ represents the wave amplitude with a spatial dependence on the propagation direction z; m indicates the site on the lattice (or waveguide number) where $m \in \{1, 2, \cdots, N\}$; and Γ_m represents the effects of defects in the waveguides, which results in random fluctuations and an additional instability in the system. These defects can be obtained through various mechanisms which include amplifiers, by imprinting photorefractive crystals with partially incoherent light into the profile of the waveguides [124], by randomly changing the width of each waveguide [125], or by increasing the number point defects in the waveguide [126]. Often these effects are neglected in numerical simulations but they are often difficult to control in real systems [127]. However, it has been shown [128] that modelling even small fluctuations results in drastic outcomes.

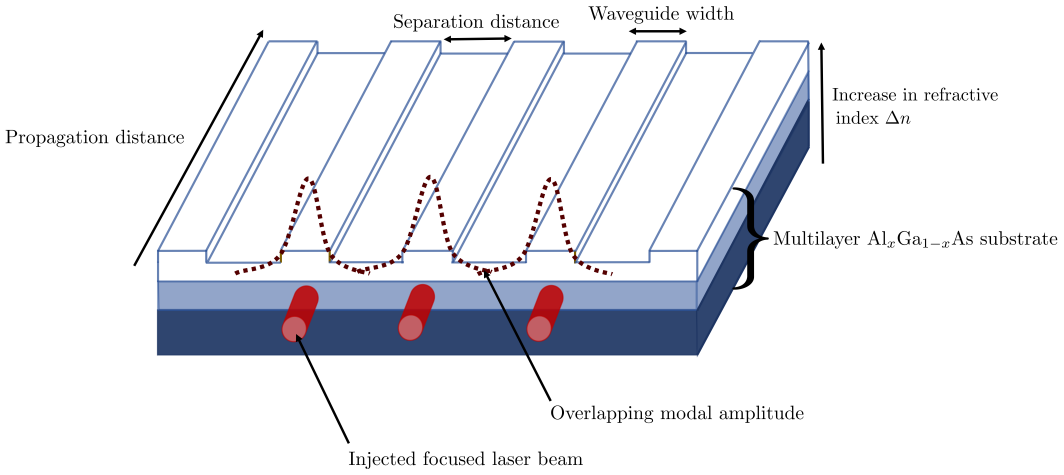

FIGURE 4.1: A schematic illustration of a possible experimental set up to study the NLSE. The waveguide system consists of $Al_xGa_{1-x}As$ multilayerd cladding, the layers of which are usually grown on top of a GaAs substrate with increasing refractive index to ensure nonlinearity. A focused light beam is injected into a waveguide and is allowed to propagate along the length of the waveguide array. These waveguides usually have a defined separation distance between waveguides of a particular width and the dotted lines indicate the overlapping modal amplitudes to allow for tunnelling into neighbouring waveguides.

Fig. 4.1 depicts a possible experimental set up of a coupled nonlinear waveguide array, which corresponds to Eq. 4.14. These waveguides are usually made from multiple layers of Al_xGa_{1-x}, where x indicates the ratio between Al and Ga ranging between 0.18 and 0.4 [129]. The layers are grown on a GaAs substrate, where each subsequent layer has a larger refractive index than the previous one. This leads to a Kerr self-focusing of the beam (nonlinearity) that is approximately 800 times more pronounced than that of fused silica [130]. Identically shaped waveguides, with subtly defined widths and separation distances, are directly written into these materials using a femto-second laser method [131]. A focused beam of light is injected into one or more central waveguides to propagate along the z-direction. Intensities are measured at the output after propagation. The dotted lines above the waveguides in Fig. 4.1 indicate the overlap of the modal amplitudes, which indicates the possible occurrence of coherent tunnelling into neighbouring waveguides.

Some experimental realisations of rogue waves in optical systems include the generation of optical rogue waves in linear optical systems, where they are spatial or spatiotemporal focused resulting in a linear superposition of waves with random wave dynamics [108]. This has been demonstrated in mutlimode glass fibres that make use of focussing lenses [132], and in spatially modulated optical beams [133]. Additionally, coupled NLSEs have been realised and gained much attention in recent years. These systems allow for the formation of optical rogue waves through oblique or head on collisions [134, 135] and have been realised by employing a switching method [136, 137]. One

particular generating mechanism of rogue waves, regardless of context, is modulation instability which has been widely studied experimentally and numerically. We introduce this mechanism next and discuss how it leads to the formation of rogue waves and solitons and a whole hierarchy of other nonlinear phenomena.

4.5 Solutions to the NLSE and Modulation Instability

Let us briefly discuss the most commonly reported analytical solutions to the NLSE and relate it to modulation instability (MI), which describes the exponential growth of an unstable modulation process on a finite background amplitude [138]. The NLSE has integrable solutions and, in its form of Eq. 4.4, has been solved using an inverse scattering method [139]. This method produces first-order solutions that are spatially and temporally periodic given by

$$\psi(\xi,\tau) = e^{i\xi}\left[1 + \frac{2(1-2a)\cosh(b\xi) + ib\sinh(b\xi)}{\sqrt{2a}\cos(\omega\tau) - \cosh(b\xi)}\right], \tag{4.15}$$

where $\omega = 2\sqrt{1-2a}$ and $b = \sqrt{8a(1-2a)}$. The positive parameter a governs the solutions permitted by Eq. 4.15 and we note that $a \neq 1/2$. The trivial case is that of $a = 0$, where the solution is a plane wave. When $0 < a < 0.5$, Eq. 4.15 permits a Akhmediev breather [138], which is a train of localised pulses that evolve with a defined temporal periodicity but it does not evolve spatially. When $a > 0$, both ω and b are imaginary and we observe a Kuznetsov-Ma soliton [140], which is a train of localised pulses that evolve with a defined spatial periodicity but it does not evolve temporally.

To understand how these solutions are related to MI, it is time now to introduce this important concept. MI is known as a possible mechanism for the formation of rogue waves and solitons resulting from the NLSE [71, 141]. It occurs various nonlinear systems such as water wave systems [142], biological systems such as DNA structures [143], or nonlinear optical waves [97, 98]. The idea behind MI is that a finite amplitude plane wave is unstable under a small perturbation when propagating through an isotropic weakly-nonlinear medium [1]. The perturbation of the plane wave leads to modulated wave envelopes, as depicted on the left panel of Fig. 4.2, where we see how the envelopes develop as the MI increases before, up to, and beyond some position ξ'. This effect was first described by Benjamin and Feir [142, 144] in water wave systems and therefore, MI is often referred to as the Benjamin-Feir instability.

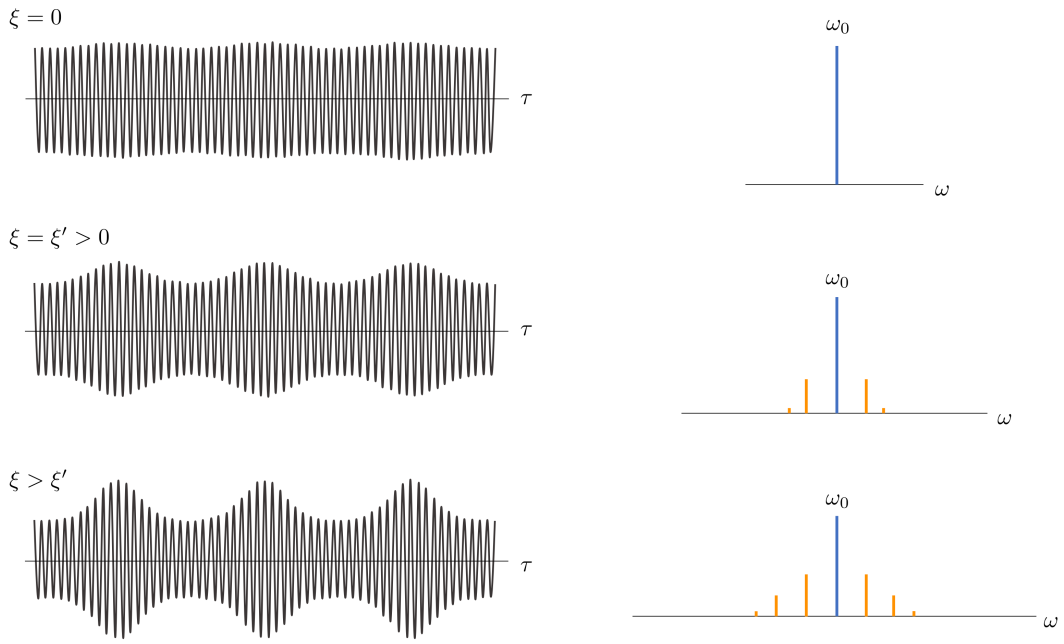

FIGURE 4.2: The effect of MI in a nonlinear medium on a finite amplitude plane wave in the time (left) and frequency (right) domain. The left panel depicts how the plane wave becomes unstable to a small perturbation which results in wave envelopes. The right panel depicts how sideband frequencies grow to the left and right of an intensity peak representing the carrier wave frequency, ω_0. Adapted from [1].

In the right panel of Fig. 4.2, we observe an interaction between the carrier frequency, ω_0, (shown in blue) and additional frequencies (shown in orange) that emerge, which are both associated with the perturbation. These additional frequencies initially grow at an exponential rate [145] and are often referred to as sidebands. By studying the frequency domain of the NLSE, we observe a region of frequency space that allows us to predict where nonlinear phenomena usually form and to derive the criteria needed for this to happen.

To understand this we can simply make use of a solution to Eq. 4.4 given by Eq. 4.15. By solving for b in terms of ω and plotting it, we observe the familiar lobe-like structure of the sideband [1, 146]. This is shown in Fig 4.3, where the grey, dashed line indicates where the MI is at its maximum. This occurs at the point $\omega = \sqrt{2}$, which corresponds to the value $a = 0.25$. At this value Eq. 4.15 permits an Akhmediev breather, as previously discussed. A similar result is observed when $a > 0.5$ and we observe a Kuznetsov-Ma soliton. These two cases nicely illustrate how MI leads to different nonlinear phenomena in the NLSE.

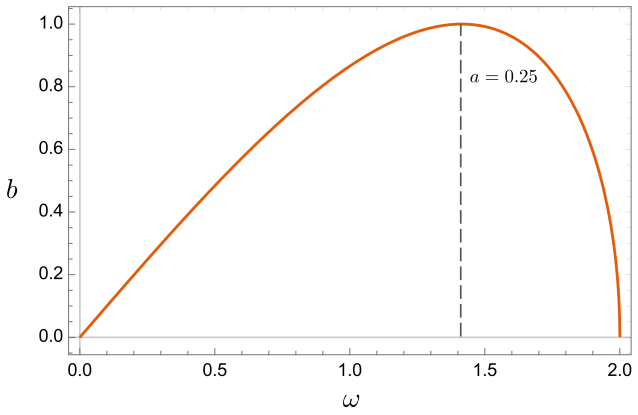

FIGURE 4.3: Modulation instability as a function of ω, where the grey, dashed lined indicates a maximum at $\omega = \sqrt{2}$ corresponding to the value $a = 0.25$.

Next, we focus on the case when $a \to 1/2$. Here, we obtain the solution [147]

$$\psi(\xi, \tau) = e^{i\xi}\left[1 - \frac{4(1 + 2i\xi)}{1 + 4\tau^2 + 4\xi^2}\right], \tag{4.16}$$

which yields a Peregrine soliton [148] (often referred to as a Peregrine rogue wave). This a single, strongly localised pulse in both the temporal and spatial dimensions emerging from a finite background amplitude, as depicted in Fig. 4.4. In all three regimes of a, we can study the profile of each of the solutions to Eq. 4.15. By fine tuning the value of a and, provided that the correct initial condition is chosen, these three solutions have been realised in pioneering experimental work, particularly in the context of optical waveguides. More specifically, the Kuznetsov-Ma soliton [140], the Akhmediev breather [149], and the Peregrine soliton [108] have all been observed in optical waveguide arrays up to now. These studies, along with many others, have strongly supported MI as a possible mechanism for generating nonlinear phenomena in the NLSE. Finally, it should be noted that all of these solutions fall into a much more general family of solutions [86] and recent studies have shown [150] that even more exotic solutions exist in these systems.

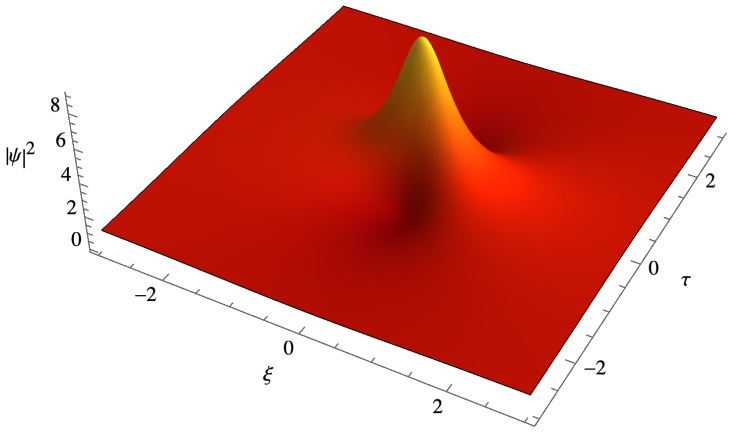

FIGURE 4.4: Solution to Eq. 4.16, where we plot $|\psi(\xi,\tau)|^2$. This yields a Peregrine soliton emerging from a finite background amplitude.

However, one does not need to follow the route of obtaining a particular analytical solution to the NLSE first and then studying the MI. In fact, one can first study the MI by making use of an approximate, linear MI analysis and then use numerical integration techniques to study the evolution of the NLSE, given the inputs provided by the MI analysis [151]. We will take this route in our analysis of rogue wave formation. It is straightforward to perform such an analysis by postulating a solution to Eq. 4.4 of the form $\psi(\xi,\tau) = (\alpha_0 + \varepsilon(\xi,\tau))e^{i(q\xi-\omega\tau)}$, where ω and q are the wave frequency and wave number of the of the carrier wave, respectively, and α_0 is the initial amplitude of the wave. In this Ansatz, the function $\varepsilon(\xi,\tau)$ represents the small perturbation, which obeys $|\varepsilon(\xi,\tau)| \ll \alpha_0$. Furthermore, the perturbation has the solution $\varepsilon(\xi,\tau) = \varepsilon_1 e^{i(Q\xi-\Omega\tau)} + \varepsilon_2^* e^{-i(Q\xi-\Omega^*\tau)}$, where Ω and Q are the wave frequency and wave number of the perturbation, respectively, and ε_1 and ε_2^* are complex numbers. Substituting the Ansatz into Eq. 4.4 results in linear dispersion relation, which identifies the unstable regions of the system when the dispersion becomes imaginary. It should be noted that the form of the perturbation and initial conditions used for numerical integration, result in nonlinear phenomena that can differ from known analytical solutions [152].

In Chapter 5, we study the effects of increasing both Γ_m and MI on particular types of rogue waves that emerge from a finite background in the discrete UNLSE. We perform an analytical MI analysis on the UNLSE and determine regions of stability and instability. We then choose points of interest that lie in these regions and we verify them using a numerical technique to temporally evolve the system. The latter part of the work presented in Chapter 5 has been published in *J. Opt. Soc. Am. A* **37**, C67-C72 (2020) by C. Pelwan, A. Quandt, and R. Warmbier [153].

Chapter 5

Rogue Waves Originating from Modulation Instability in the UNLSE

The appearance of oceanic rogue waves resulting from MI has been well documented and understood. The destructive and elusive nature of rogue waves has fascinated scientists for centuries, and a particularly intriguing feature is that they are often reported to "appear out of nowhere" and then "disappear suddenly". As we have discussed in Chapter 4, the NLSE provides us with a mathematical tool, which we can use to study rogue waves.

Moreover, optical waveguide arrays provide experimentalists with a playground where simple, experimental set-ups can be used to study and confirm the analytical solutions to the NLSE. Recently, studies on these systems have discussed the role of rogue wave formation as a result of increasing disorder to the system [127, 154]. These systems have also exhibited long-lived rogue waves [128], which were modelled by the UNLSE for a particular choice of initial conditions. These long-lived rogue waves are formed as a result of small, random fluctuations for the unstable parameter, Γ_m. Unlike Peregrine rogue waves, these discrete, long-lived rogue waves are large amplitude peaks that are very delocalised along the waveguide and are confined to few waveguides in the array. However, such phenomena are not restricted to discrete optical waveguides, as similar observations have been noted in discrete, biological DNA structures [143] and a 1D chain of hydrogen-bonds that contains a peptide group [155]. As we have pointed out in Chapter 4, often focus is placed on the spatial or

temporal evolution of rogue waves resulting from MI. However, to the best of our knowledge, the time taken for them to emerge from the background has been largely overlooked.

In what follows, we study the formation of rogue waves that form as a result of MI in the UNLSE. We then study the effects that increasing Γ_m has on a system of multiple long-lived rogue waves for various points identified by the MI analysis.

5.1 The Unstable Nonlinear Schrödinger Equation

We study the discrete UNLSE which is used to to describe nonlinear phenomena in optical waveguide arrays. For ease of reference, we restate the UNLSE, which is a 1D lattice that models an optical waveguide array. Here, the separation between waveguides (sites) is set to unity and the array (lattice) includes a coupled, nearest neighbours interaction, a nonlinear term, and the unstable term. In dimensionless units, the UNLSE is given by [123]

$$i\frac{\partial}{\partial t}A_m + \beta\left(A_{m+1} - 2A_m + A_{m-1}\right) + \gamma|A_m|^2 A_m + \Gamma_m A_m = 0, \tag{5.1}$$

where $A_m(t)$ is a complex valued function, the parameters β and γ are real valued numbers, and m represents a waveguide in an array of N waveguides. We study values of $\Gamma_m = w\Gamma_0$ such that w, the maximum amplitude of these fluctuations, is a small constant in the range $[5 \cdot 10^{-5}, 5 \cdot 10^{-2}]$, Γ_0 randomly fluctuates between $[-1, 1]$, and for simplicity we set $\beta = \gamma = 1$.

5.1.1 Aims

We aim to study the effects that both MI and the randomly fluctuating parameter Γ_m have on a system of long-lived rogue waves. To do so, we perform an MI analysis and identify points of interest that lie an instability region. We then use a numerical technique to study the time evolution of the system for small values of increasing Γ_m using these unstable points of interest, where rogue waves are likely to occur.

5.2 Analytical Analysis: Modulation Instability

To obtain the regions where Eq. 5.1 becomes unstable, one performs a standard linear stability analysis by applying a plane wave solution to Eq. 5.1 given by

$$A_m(t) = A_0 e^{i\theta_m}, \quad \text{with} \quad \theta_m = qm - \omega t, \tag{5.2}$$

where ω and q are the wave frequency and wave number of the of the carrier wave, respectively, and A_0 is the initial amplitude of the wave. Strictly speaking, this plane wave solution is only valid when the potential is constant. Thus, for the validity of the MI analysis to hold, we consider a Γ_m independent of the waveguide m and we will proceed with the assumption that $\Gamma_m = \Gamma = 0$. Therefore, final equation governing the MI will be independent of Γ but, for the simulations that follow, we will consider the effects of Γ_m assuming that the fluctuations will not shift the system out of the instability region.

By substituting Eq. 5.2 into Eq. 5.1 with $\Gamma_m = \Gamma = 0$, we obtain an equation governing the frequency ω, which is found to be

$$\omega = 4\beta \sin^2\left(\frac{q}{2}\right) - \gamma A_0^2. \tag{5.3}$$

At this point, we introduce the perturbation into our system, which forms part of the stability analysis. This is done by investigating solutions to Eq. 5.1 for the Ansatz

$$A_m(t) = \left(A_0 + \varepsilon_m\right) e^{i\theta_m}, \tag{5.4}$$

where $\varepsilon_m = \varepsilon_m(t)$ represents a small perturbation such that $|\varepsilon_m| \ll A_0$. We substitute this Ansatz into Eq. 5.1 beginning with the first term which is given by

$$\begin{aligned} i\frac{\partial}{\partial t}A_m &= \left(\omega A_0 + \omega\varepsilon_m + i\frac{\partial}{\partial t}\varepsilon_m\right) e^{i\theta_m} \\ &= \left(4\beta \sin^2\left(\frac{q}{2}\right) A_0 - \gamma A_0^3 + 4\beta \sin^2\left(\frac{q}{2}\right)\varepsilon_m - \gamma A_0^2\varepsilon_m - i\frac{\partial}{\partial t}\varepsilon_m\right) e^{i\theta_m}, \end{aligned} \tag{5.5}$$

where we arrived at the second line in Eq. 5.5 by making use of the relation in Eq. 5.3. The second term is given by

$$\begin{aligned} \beta\left(A_{m+1} - 2A_m + A_{m-1}\right) &= \beta\left(A_0 e^{iq} + A_0 e^{-iq} - 2A_0 + \varepsilon_{m+1}e^{iq} + \varepsilon_{m-1}e^{-iq} - 2\varepsilon_m\right) e^{i\theta_m} \\ &= -4\beta \sin^2\left(\frac{q}{2}\right) A_0 e^{i\theta_m} + \beta\left(\varepsilon_{m+1}e^{iq} + \varepsilon_{m-1}e^{-iq} - 2\varepsilon_m\right) e^{i\theta_m}. \end{aligned} \tag{5.6}$$

Finally, the third term is expanded to give

$$\begin{aligned}\gamma|A_m|^2A_m &= \gamma\left[(A_0+\varepsilon_m)\left(A_0+\varepsilon_m^*\right)\right](A_0+\varepsilon_m)\,e^{i\theta_m}\\ &= \gamma\left[A_0^3+A_0^2\left(\varepsilon_m+\varepsilon_m^*\right)+A_0|\varepsilon_m|^2+A_0^2\varepsilon_m+A_0\left(\varepsilon_m+\varepsilon_m^*\right)\varepsilon_m+A_0|\varepsilon_m|^2\varepsilon_m\right]e^{i\theta_m},\end{aligned} \tag{5.7}$$

where ε_m^* is the complex conjugate of ε_m.

We can now collect all the terms, noting the cancellations of many of them. We then drop the phase factor of $e^{i\theta_m}$ and keep terms that are $O(\varepsilon_m)$. In doing so, we obtain the linear equation governing the perturbation which is given by

$$\boxed{i\frac{\partial}{\partial t}\varepsilon_m+\beta\left(\varepsilon_{m+1}e^{iq}+\varepsilon_{m-1}e^{-iq}-2\varepsilon_m+4\sin^2\left(\frac{q}{2}\right)\varepsilon_m\right)+\gamma A_0^2\left(\varepsilon_m+\varepsilon_m^*\right)=0.} \tag{5.8}$$

Eq. 5.8 has a steady-state solution when we choose [104]

$$\varepsilon_m(t)=\varepsilon_1e^{i\varphi_m}+\varepsilon_2e^{-i\varphi_m^*}, \tag{5.9}$$

with $\varphi_m=(Qm-\Omega t)$. Here, ε_1 and ε_2 are complex, where Q is the real wave number, and Ω is a complex valued frequency. Substituting this into the first term in Eq. 5.8 gives

$$i\frac{\partial}{\partial t}\varepsilon_m=\Omega\varepsilon_1e^{\varphi_m}-\Omega^*\varepsilon_2e^{\varphi_m^*}. \tag{5.10}$$

The second term reads

$$\begin{aligned}&\beta\left(\varepsilon_{m+1}e^{iq}+\varepsilon_{m-1}e^{-iq}-2\varepsilon_m+4\sin^2\left(\frac{q}{2}\right)\varepsilon_m\right)\\ &=\beta\Bigg(\varepsilon_1e^{i\varphi_m}\left(e^{i(q+Q)}+e^{-i(q+Q)}\right)+\varepsilon_2e^{-i\varphi_m^*}\left(e^{i(q-Q)}+e^{-i(q-Q)}\right)-2\left(\varepsilon_1e^{i\varphi_m}+\varepsilon_2e^{-i\varphi_m^*}\right)\\ &\quad+4\sin^2\left(\frac{q}{2}\right)\left(\varepsilon_1e^{i\varphi_m}+\varepsilon_2e^{-i\varphi_m^*}\right)\Bigg)\\ &=\beta\left(\varepsilon_1e^{i\varphi_m}\left(2\cos(q+Q)-2+4\sin^2\left(\frac{q}{2}\right)\right)+\varepsilon_2e^{-i\varphi_m^*}\left(2\cos(q-Q)-2+4\sin^2\left(\frac{q}{2}\right)\right)\right)\\ &=4\beta\left(\varepsilon_1e^{i\varphi_m}\left(\sin^2\left(\frac{q}{2}\right)-\sin^2\left(\frac{q+Q}{2}\right)\right)+\varepsilon_2e^{-i\varphi_m^*}\left(\sin^2\left(\frac{q}{2}\right)-\sin^2\left(\frac{q-Q}{2}\right)\right)\right).\end{aligned} \tag{5.11}$$

Lastly, the third term becomes

$$\gamma A_0^2\left(\varepsilon_m+\varepsilon_m^*\right)=\gamma A_0^2\left(\varepsilon_1e^{i\varphi_m}+\varepsilon_1^*e^{-i\varphi_m^*}+\varepsilon_2e^{-i\varphi_m^*}+\varepsilon_2^*e^{i\varphi_m}\right), \tag{5.12}$$

where ε_1^* and ε_2^* are the complex conjugates of ε_1 and ε_2, respectively. By collecting all the terms, we see that there are two linear equations for $\varepsilon_1$and ε_2, respectively. This forms the following matrix equation

$$\begin{bmatrix} \Omega + 4\beta\left(\sin^2\left(\frac{q}{2}\right) - \sin^2\left(\frac{q+Q}{2}\right)\right) + \gamma A_0^2 & \gamma A_0^2 \\ \gamma A_0^2 & -\Omega^* + 4\beta\left(\sin^2\left(\frac{q}{2}\right) - \sin^2\left(\frac{q-Q}{2}\right)\right) + \gamma A_0^2 \end{bmatrix} = 0, \quad (5.13)$$

which has a nontrivial solution. By taking the determinant of Eq. 5.13, we obtain the dispersion relation for Ω as function of Q and q

$$\boxed{\Omega(Q,q) = 2\beta \sin Q \sin q + 2i \sin\left(\frac{Q}{2}\right)\sqrt{2\beta\cos q\left(\beta\cos q\left(\cos Q - 1\right) + \gamma A_0^2\right)}.} \quad (5.14)$$

Eq. 5.14 provides us with regions where the system is unstable. Later, we will verify these regions through numerical simulations.

Furthermore, in Eq. 5.14 both q and Q are restricted to the first Brillouin zone, that is, q and $Q \in [-\pi, \pi]$ [151]. However, since Ω is symmetric about the x- and y-axis, we restrict ourselves to studying the range where q and $Q \in [0, \pi]$. As noted in [156], in the self-focusing case when $\gamma > 0$, an instability region appears only when $\cos(q) > 0$, which implies that $q/\pi < 1/2$. We plot the imaginary part of Eq. 5.14, $\mathrm{Im}(\Omega)$, in Fig. 5.1(A), with $\beta = \gamma = A_0 = 1$. The orange band depicts values where $\mathrm{Im}(\Omega) > 0$ and where for small Q the instability in the system increases exponentially.

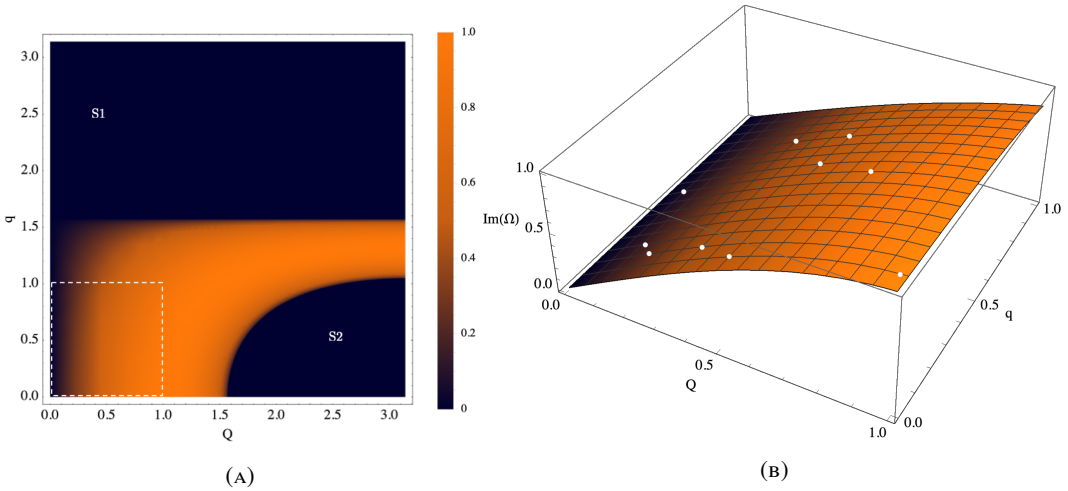

FIGURE 5.1: The modulation instability $\mathrm{Im}(\Omega(Q,q))$ of Eq. 5.14 with $\beta = \gamma = A_0 = 1$. The orange band in (A) depicts values where the $\mathrm{Im}(\Omega)$ is non-zero. Labels S1 and S2 identify stable points where $\mathrm{Im}(\Omega)$ is zero. The dashed box in (A) is represented in 3D in (B). In (B), each white circle indicates a point of interest, where $0 < \mathrm{Im}(\Omega) \leq 1$.

The dashed box in Fig. 5.1(A) represents our region of interest, where the system is unstable. In Fig. 5.1(B), we plot the 3D landscape of Im(Ω) to show how the instability grows in this dashed box. Each white circle that is situated on this plane represents a point of interest that we consider in the following analysis. When the respective Q and q values of these points are inserted into Eq. 5.14, we find that $0 < \text{Im}(\Omega) \leq 1$. Thus, we can study the effect of increasing MI in the system. We also identify two points in the stability region, where Im(Ω) = 0. These are at S1 = (0.6, 2.5) and S2= (2.5, 0.6). We will insert all points of interest into our second choice of initial conditions when propagating Eq. 5.1 in time. For points S1 and S2, we expect no rogue wave formation. But we expect large amplitude waves and rogue wave formation when using the points in the unstable region as inputs.

5.3 Rogue Wave Solutions to the UNLSE

In this section we use numerical techniques to integrate Eq. 5.1 using two different initial conditions that yield different rogue wave solutions. The first initial condition we consider highlights the "appearing out of nowhere" and "disappearing without a trace" characteristic that is associated with oceanic rogue waves. The second initial condition highlights rogue waves that are referred to as long-lived that were initially observed in optical waveguide simulations [128]. These rogue waves also "appear out of nowhere" but they can typically survive for as long as we have been able to monitor their evolution along the waveguide system. In the latter case, we utilise the points of interest that we have identified in the MI analysis when applying our numerical integration and then discuss the effect that increasing random fluctuations have on the system. To this end, we use SciPy [157] and we employ the Runge-Kutta 4 algorithm [158], which is an initial valued ordinary differential equation solver. To ensure the conservation of total amplitude, $\sum_m |A_m|^2$, at each step during integration, we set the relative error tolerance value to 10^{-8}. Random fluctuations for Γ_0 were generated for each waveguide in the lattice using the built-in `random` function of SciPy. We provide further numerical details in Appendix B.

The first initial condition, $A_m(t = 0)$, relates to a solution to the NLSE, which we have discussed in Sec. 4.5. It is given by

$$A_m(t=0) = \epsilon \left(1 - 4 \left(\frac{1 - 2i\epsilon^2 T}{1 + 2\epsilon^2 \left(\frac{N}{2\pi} \sin\left(\frac{2\pi m}{N} \right) \right)^2 + 4\epsilon^4 T^2} \right) \right) e^{-i\epsilon^2 T}, \tag{5.15}$$

where the perturbation ϵ should be $\ll A_0$ for the solution to be valid. A similar initial condition has been discussed in both the continuous [159] and discrete [160, 161] versions of the NLSE. Since Eq. 5.15 is not dependent on either Q or q, we do not make use of our points of interest identified by the MI analysis. However, as we have pointed out in Sec. 4.5, this initial condition is similar to the first order solution to the continuous NLSE in Eq. 4.16, where the MI is at a maximum. We therefore expect that the solution to the analogous, discrete system be is similar to that shown in Fig. 4.4, which is a rogue wave emerging from a finite background, classified specifically as a Peregrine rogue wave.

Fig. 5.2(A) depicts the time evolved solution to Eq. 5.1 for this choice of the initial condition, where we have set the following parameters for the simulation: $w = 0$, $N = 100$, $\epsilon = 2 \cdot 10^{-1}$, and $T = 5000$. The time dynamics show a finite plane wave amplitude that propagates without any increase in amplitude for $0 \leq t \lesssim 4500$, where we note that t is in units of $[1/10\beta]$. For $t > 4500$, we find the formation of large amplitude waves that emerge from this background. The increase in intensity is indicated by the change in colour from red to white in Fig. 5.2(A) and we find that these waves are approximately 2.5 times larger than the finite background plane wave. By making use of the AI index, which we introduced in Sec. 4.1, we can identify this wave as a rogue wave as done in [160] since their heights are at least twice as large as the background amplitude.

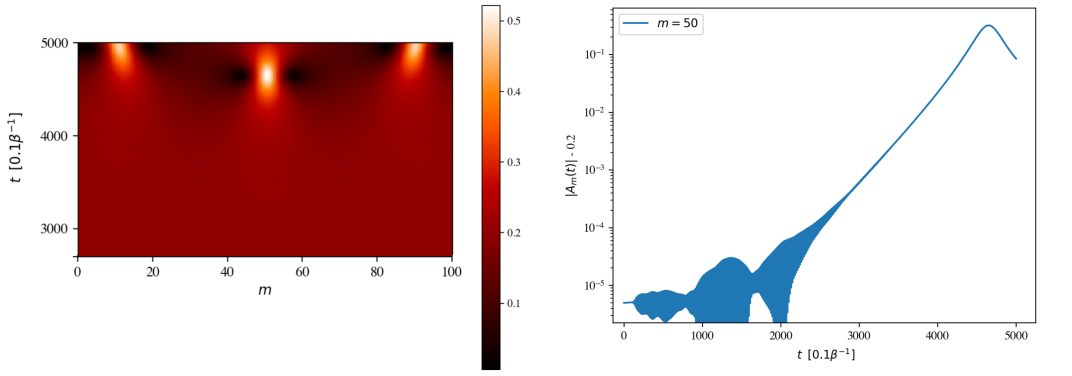

(A) Centrally occurring rogue wave at waveguide $m = 50$.

(B) Log scale of difference between amplitude at $m = 50$ and background.

FIGURE 5.2: Time evolution of Eq. 5.1 with initial condition Eq. 5.15 showing a Peregrine rogue wave solution and profile along maximum intensity. Here, $\beta = \gamma = 1$, $N = 100$, $T = 5000$, $\epsilon = 2 \cdot 10^{-1}$, and $w = 0$.

The appearance of this rogue wave is as a result of MI. Since MI is at a maximum for Eq. 5.15, any perturbation results in the instability of the plane wave that grows exponentially to a maximum value. In this case, we have set the perturbation to the size of $\epsilon = 2 \cdot 10^{-1}$. This process is clearly seen in Fig. 5.2(B), where we plot the log of the difference between the amplitude along $m = 50$ and the

amplitude of the finite background. We see that the effect of perturbation results in modulations of the plane wave from around $t \geq 150$. Initially, these modulations are broad, but they self-focus and grow within waveguide $m = 50$. After $t > 2000$, we see the exponential growth of the modulation, which then self-focuses to a maximum amplitude, forming the rogue wave. Thereafter, the modulation defocusses and the rogue wave "disappears". The profile along $m = 50$ indicates that the rogue wave takes on a Gaussian-like form, as it is localised in t and only appears in one waveguide in the array. This is similar to the Peregrine rogue wave shown in Fig. 4.4, which is strongly localised in both time and space.

We now consider how an increasing MI effects the solutions to the UNLSE. That is, we make use of the MI analysis performed in Sec. 5.2 to highlight differences in the formation of long-lived rogue waves for $\mathrm{Im}(\Omega) \in [0, 1]$. We introduce our second initial condition, which is a periodically modulating wave that takes in both Q and q as inputs. The initial condition takes the form

$$A_m(t = 0) = \left(A_0 + \epsilon e^{iQm}\right) e^{iqm}, \tag{5.16}$$

where we set $A_0 = 1$ and the perturbation size to $\epsilon = 1 \cdot 10^{-3}$. To study the long time dynamics of the system, we set $T = 1.6 \cdot 10^4$ and we increase the total number of waveguides in the system to $N = 400$. All other parameters are kept the same as before.

To begin with, we consider the temporal evolution of our system in the stable regions, where $\mathrm{Im}(\Omega)$=0. That is, we insert the values of Q and q from S1 and S2 into Eq. 5.16 and time evolve Eq. 5.1 by numerical integration with $w = 0$. The solutions to S1 and S2 show no sign of rogue waves and energy in the system is evenly distributed among all waveguides in both cases. This corroborates our conjecture that the stability regions identified by Eq. 5.14 do not give rise to rogue waves.

For $\mathrm{Im}(\Omega) = 0$, setting w to $5 \cdot 10^{-2}$ leads to perturbations to the plane wave background that increase its amplitude in a chaotic manner. However, this increase does not lead to the formation of rogue waves as is shown in Fig. 5.3, where there are several localised areas that develop on the plane wave. These findings are similar to those reported in [162], where an intermediate regime of MI is studied, but with no random fluctuations introduced into the system. The reported findings indicate that in order for rogue waves to form, not only are perturbations to the plane wave required, but also that the magnitude of the self-focusing parameter needs to be sufficiently large. Thus, in our case when $\mathrm{Im}(\Omega) = 0$ and $\gamma = 1$, the magnitude of self-focusing effect is insufficiently small to form rogue waves, despite the perturbations to the plane wave caused by Γ_m.

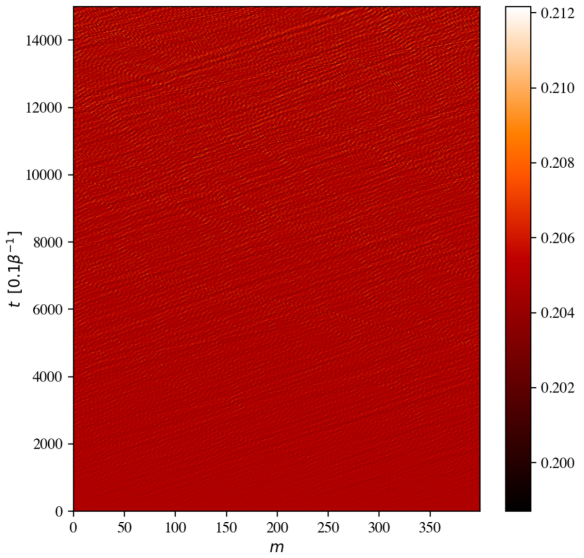

FIGURE 5.3: Temporal evolution of Eq. 5.1 with initial condition Eq. 5.16, where $\beta = \gamma = A_0 = 1$, $N = 400$, $T = 1.6 \cdot 10^4$, $\epsilon = 1 \cdot 10^{-3}$, $w = 5 \cdot 10^{-2}$, $Q = 0$, and $q = 0.75\pi$.

Next, we consider solutions to Eq. 5.1 for the points of interest we identified in Fig. 5.1(B), where the system is unstable. As an example of the effects that increasing MI has on the system, let us study time evolution of Eq. 5.1 for two different points of interest where $\mathrm{Im}(\Omega) = 0.35$ and 1, respectively, with the maximum amplitude of the fluctuations $w = 0$. In both cases, we find that the nonlinear phenomena in the system form as a result of the interplay between MI, as discussed previously, as well as hopping which drives the spreading out of wave packets, and the nonlinearity, which for $\gamma > 0$ drives self-focussing.

Let us first consider the short time dynamics of these systems for times between $0 \leq t \lesssim 250$. This is shown in Fig. 5.4, where we find that the interplay between self-focusing and MI leads to large amplitude waves, similar to the Peregrine rogue wave previous discussed. These waves re-emerge are some time and they can hop into other waveguides since $\beta > 0$. A wave may inelastically collide with another to form a larger amplitude wave that becomes more delocalised in time. This effect is referred to as self-trapping [162] and can be understood as follows: provided that the amplitude of a wave is sufficiently large [163], the wave may remain localised within a few waveguides, but becomes delocalised in time. Using the nomenclature of [128] we can refer to the delocalised nature of these rogue waves as long-lived as they remain self-trapped for relatively long times. Thus, these long-lived waves either continue to inelastically collide with each other to form a delocalised wave that extends beyond the total temporal size of the system, or if their amplitudes are not sufficiently large enough, they may defocus and disappear.

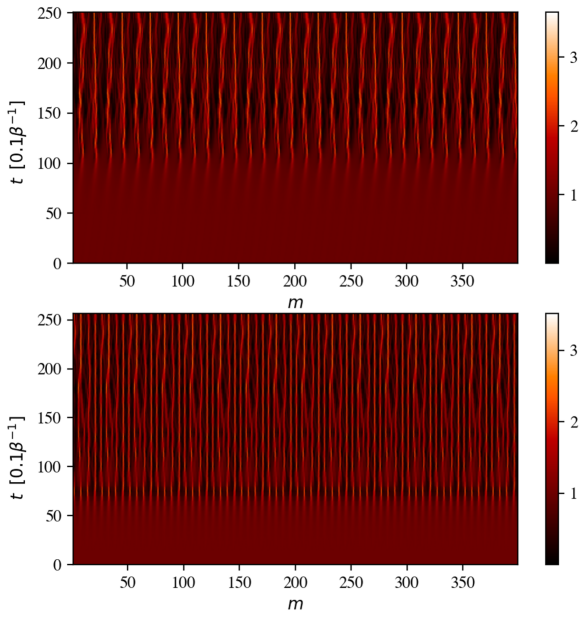

FIGURE 5.4: Time evolution of Eq. 5.1 with initial condition Eq. 5.16 between $0 \leq t \lesssim 250$ for $Q = 0.31$ and $q = 0.75$ giving $\mathrm{Im}(\Omega) = 0.35$ (upper), and $Q = 1$ and $q = 0.06$ giving $\mathrm{Im}(\Omega) = 1$ (lower). Here, $\beta = \gamma = A_0 = 1$, $w = 0$, $N = 400$, $T = 1.6 \cdot 10^4$, and $\epsilon = 1 \cdot 10^{-3}$.

We see examples of both these cases in Fig. 5.5(A), where we display the full temporal evolution of the system. Between waveguides $m = 100$ and $m = 150$, we find long-lived, large amplitude waves that continue to propagate to around $t \approx 500$, where they undergo defocusing. On the other hand, we also observe multiple long-lived, large amplitude waves that extend beyond the total time of the system; an example of this is found at waveguide $m = 79$ in Fig. 5.5(A). Once again, we can classify these large amplitude waves as rogue waves using the AI criterion. We also find that the long-lived rogue waves that form in Figs. 5.5(A) and 5.5(B) remain within at most three waveguides that are direct neighbours of each other. These observations are consistent with those reported in [128, 155], where the formation of multiple rogue waves have been studied in similar systems.

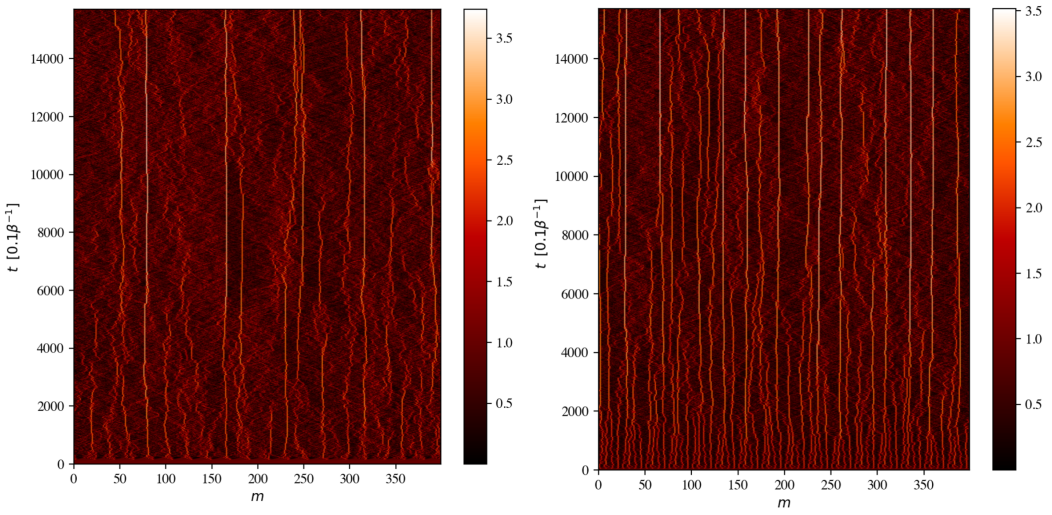

FIGURE 5.5: Time evolution of Eq. 5.1 with initial condition Eq. 5.16 showing multiple long-lived rogue waves for $Q = 0.31$ and $q = 0.75$ giving $\mathrm{Im}(\Omega) = 0.35$ in (A), and $Q = 1$ and $q = 0.06$ giving $\mathrm{Im}(\Omega) = 1$ in (B). Here, $\beta = \gamma = A_0 = 1$, $w = 0$, $N = 400$, $T = 1.6 \cdot 10^4$, and $\epsilon = 1 \cdot 10^{-3}$.

In general, the effect of increasing MI results in a larger number of self-trapped, long-lived rogue waves. This is evident from Fig. 5.5(B), where a larger number rogue waves is observed than in Fig. 5.5(A), which indicates that for larger MI in the system there is an increase in the number of perturbations to the plane wave finite background. This results in a greater number of large amplitude peaks that inelastically collide. In Fig. 5.5(B), we clearly see the formation of these peaks between $70 \lesssim t \lesssim 2000$. Many of these inelastic collisions result in much longer lived rogue waves that extend beyond the total temporal size of the system. As in Fig. 5.5(A), we also find rogue waves in Fig. 5.5(B) that disappear after some time as their amplitudes are not large enough for them to continue indefinitely.

Finally, we note that as MI is increased in the system, the time that passes until large amplitude waves emerge from the finite background decreases. We will refer to this as the onset time. The earlier onset for larger MI is observed in Fig. 5.4, but can easily quantified by considering Fig. 5.6. Here, we plot the maximum amplitude for each t during the time evolution of Eq. 5.1 using $\mathrm{Im}(\Omega) = 0.08$ and $\mathrm{Im}(\Omega) = 1$ as an example. As is shown in the inset of Fig. 5.6, for $\mathrm{Im}(\Omega) = 0.08$ we find that the finite background remains at a value of 1 before exponentially increasing at around $t \approx 260$, whereas for $\mathrm{Im}(\Omega) = 1$ the exponential increase occurs at around $t \approx 30$. We also find that the onset of rogue waves, with $|A_m| \geq 2$, occurs earlier for larger MI.

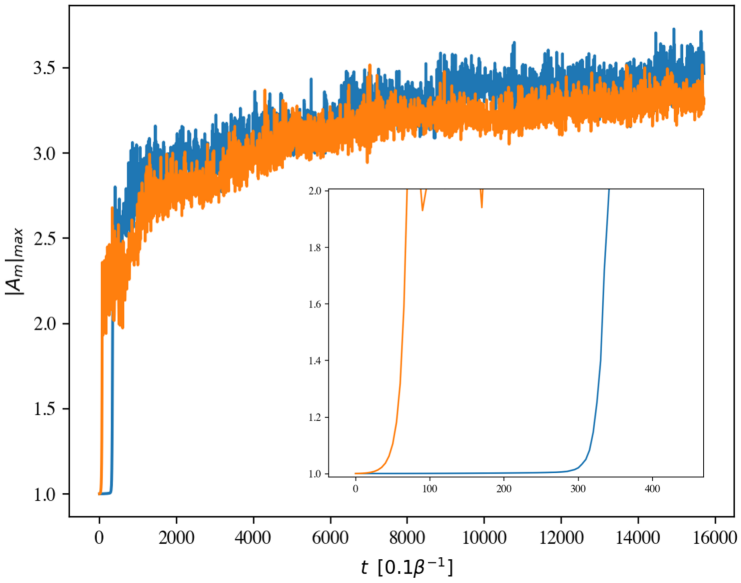

FIGURE 5.6: Time evolution of maximum amplitude for two different values of Im(Ω), where the inset shows the time evolution for $0 \leq t \leq 500$.

Recall that the exponential increase in Fig. 5.6 is associated with the self-trapping of rogue waves in the system. In general, we find that for $|A_m| \approx 2.5$, this exponential increase ceases and instead the maxima of $|A_m|$ flattens out gradually to around 3.7. Thus, we find that rogue waves have a larger amplitude towards the end of the time evolution. We can understand this behaviour by considering Fig. 5.5(B). Here, the amplitude of the rogue waves that occur between $70 \lesssim t \lesssim 2000$ are smaller before colliding inelastically. As a result of these collisions, the self-trapped rogue waves increase in amplitude. As the time evolution approaches T, there are fewer rogue waves in the system than at the onset of the rogue waves. Since the total energy of the system is conserved, the rogue waves at T have a larger amplitude than those recorded at the onset.

We now turn our attention to the effects of random fluctuations in the system, by setting $\Gamma_m \neq 0$ in Eq. 5.1. We reiterate that the effects of random fluctuations induced by Γ_m are often neglected in numerical simulations, but can often be difficult to control in real life experiments. Thus, studying these effects is relevant. Similar numerical studies to ours have considered rogue waves that appear periodically for a particular choice of initial condition [128]. These studies have shown the inclusion of small ($\sim 10^{-3}$) random fluctuations in this system results in the loss of this periodic structure, which then leads to the formation of long-lived rogue waves. The second initial condition we have chosen already exhibits long-lived rogue waves for $\Gamma_m = 0$. Therefore, we ask what other effects random fluctuations may have on the system for increasing MI.

We time evolve Eq. 5.1 for each point of interest in Fig. 5.1(B) and we find that increasing Γ_m for a given value of Im(Ω) leads to a decrease in the onset time. Thus, we note that increasing Γ_m has an effect similar to MI when considering the onset of rogue waves. We find no correlations between increasing Γ_m and the amplitude of the rogue waves or how many rogue waves appear in the system. We also note that rogue waves appear at random waveguides in the array.

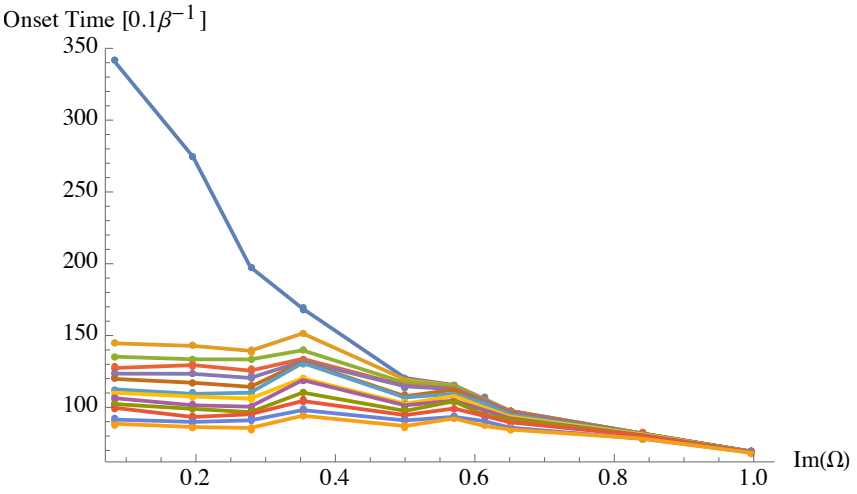

FIGURE 5.7: The onset time vs Im(Ω), where each line, from dark blue to orange, represents an increasing Γ_m.

By plotting the time evolution of the maximum amplitude of different values of Γ_m for a given Im(Ω) and obtaining the onset time which occurs when $|A_m|_{max} = 2$, we obtain the results of Fig. 5.7. In this figure, we show the onset times for different values of Im(Ω) when the first rogue wave occurs. The size of each marker represents the error associated with that particular value. These errors were obtained by randomly dividing the array into 10 sub-arrays of 30 waveguides each. The error is then the standard deviation between the onset times for these sub-arrays. The different values of Γ_m are indicated by different colours, where the first dark blue line represents the onset times with $\Gamma_m = 0$. At small Im(Ω), we see that as Γ_m increases, the onset times decrease monotonically, starting light brown line representing $w = 5 \cdot 10^{-5}$ and increasing w up to the orange line where $w = 5 \cdot 10^{-2}$.

The earlier onset times as a result of increasing Γ_m can be understood by noting that the random fluctuations that occur on the finite background result in an increase to the instability of the background. This leads to an increased number of peaks that occur at earlier onset times for larger values of w. Fig. 5.7 also shows that for a small value of Im(Ω), there is already a large difference in onset times between a system where $w = 0$ and even a very small increase in w. This difference become less pronounced as Im(Ω) is increased. Regardless of the value of w, when Im(Ω) is at its maximum,

the onset times converge to around $t \approx 69$. Therefore, MI has a larger effect on the onset times than increasing Γ_m.

5.4 Conclusions

We investigated the interplay between modulation instability and a small, randomly fluctuating Γ_m in the UNLSE describing a nonlinear waveguide array. We have studied the effects of modulation instability when $\Gamma_m = 0$. This was done by investigating the well-know Peregrine rogue wave solution in the UNLSE, which emerges as the result of the interplay between modulation instability and self-focusing.

We then studied the effects of an increasing modulation instability. To do this we introduced a new initial condition that depends both on the wave number of the carrier wave q and the perturbation Q, respectively. Using analytical techniques we identified the stable and unstable regions governed by the modulation instability function, $\mathrm{Im}(\Omega(Q, q))$. We then selected points in the unstable region to demonstrate the effects of modulation instability in the system. We found large amplitude waves, which collide inelastically to form long-lived rogue waves. As modulation instability increases, we found that the number of long-lived rogue waves increases and that the onset time for these waves decreases.

We then introduced random fluctuations by setting $\Gamma_m \neq 0$. We found that an increase in Γ_m at a particular modulation instability, results in an earlier onset time due to random fluctuations that occur on the finite background. Near the maximum MI, we always observed a convergence to the same onset time for all values of Γ_m. This suggests that a large modulation instability has a stronger effect than Γ_m with respect to the onset times of rogue waves, but that random effects play a noticeable role when modulation instability is small. Let us also point out that the suggested waveguide array can be fabricated and therefore provides an experimental playground to study rogue waves and their onset times under controlled conditions. Furthermore, the insights gained from ours and similar simulations may be very helpful in the context of optical technologies that are based on real, large-scale waveguide arrays.

Appendix B

Numerical Analysis

In this appendix section, we provide details to the Runge Kutta 4 algorithm used for the numerical integration in Chapter 5. Runge Kutta 4 is an algorithm that can be used to solve initial value problems for ordinary differential equations. In our case, we numerically integrated the UNLSE in Eq. 5.1. In general, this method can be used to solve equations with a general form

$$\frac{dy(t)}{dt} = f(t, y(t)), \quad \text{with} \quad y(t_0) = y_0, \tag{B.1}$$

where t_0 represents the initial time and y_0 is the corresponding initial value of the function. In Eq. B.1, the time derivative of $y(t)$ is dependent on t and on that solution $y(t)$ at t. The Runge Kutta 4 algorithm uses the an approximate initial condition and then estimates the slope of the function up to forth order to produce a weighted sum given by

$$y_{n+1} = y_n + h\left(\frac{1}{6}k_1 + \frac{1}{3}k_2 + \frac{1}{3}k_3 + \frac{1}{6}k_4\right), \tag{B.2}$$

where k_i is the ith slope at some small time step h and we approximate $y(t_{n+1})$ with y_{n+1}. Each of these slopes is explicitly calculated using

$$\begin{aligned} k_1 &= f(t_n, y_n), \\ k_2 &= f\left(t_n + \frac{h}{2}, y_n + \frac{k_1}{2}\right), \\ k_3 &= f\left(t_n + \frac{h}{2}, y_n + \frac{k_2}{2}\right), \quad \text{and} \\ k_4 &= f\left(t_n + h, y_n + k_3\right). \end{aligned} \tag{B.3}$$

We see from Eqs. B.3, that at each k_2, k_3, and k_4, we improve the accuracy of the estimate for the next k. These additional corrections make Runge Kutta 4 a very accurate method and it has become a standard for calculating ordinary differential equations. In our case, we found that the integration was numerically stable for the parameters we were interested in.

As an example, we integrate

$$i\frac{\partial}{\partial t}A_m + \beta\left(A_{m+1} - 2A_m + A_{m-1}\right) + \gamma|A_m|^2 A_m + \Gamma_m A_m = 0, \tag{B.4}$$

using the initial condition

$$A_m(t=0) = \left(A_0 + \epsilon e^{iQm}\right) e^{iqm}, \tag{B.5}$$

where we set $Q = 1$, $q = 0.06$, $\epsilon = 1 \cdot 10^{-3}$, $\beta = A_0 = \gamma = 1$, and $w = 0$ and $w = 5 \cdot 10^{-2}$. Then, we plot the relative change in the total amplitude, $\sum_m(|A_m|^2/|A_0|^2) - 1$, which gives us an indication of the energy conservation at each step during integration. The relative error tolerance value was set to 10^{-8} for Runge Kutta 4.

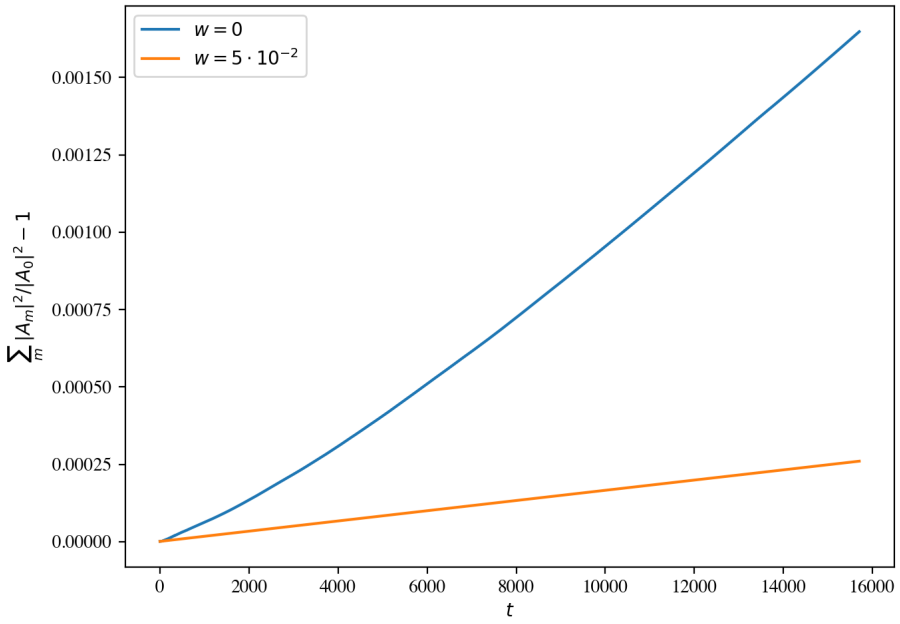

FIGURE B.1: The relative change in the total amplitude over the total time of integration $T = 1.6 \cdot 10^4$ for the Runge Kutta algorithm. Parameters in Eq. B.4 are set to $\beta = \gamma = 1$, and $w = 0$ and $w = 5 \cdot 10^{-2}$. Parameters in Eq. B.5 are set to $Q = 1$, $q = 0.06$, $\epsilon = 1 \cdot 10^{-3}$, and $A_0 = 1$, with the relative error tolerance values in both simulations set to 10^{-8}.

In both cases, we observe that the relative change in the total amplitude increases as t increases. For $w = 0$, the maximum deviation is around $1.75 \cdot 10^{-3}$, but this is smaller when random fluctuations are included. The slower increase can be attributed to Γ_0, which can take negative values that present during integration when $w \neq 0$. Therefore, $\sum_m |A_m|^2$ does not increase as rapidly when $\Gamma_m \neq 0$.

Chapter 6

Summary

In this thesis we have studied aspects relating to two one-dimensional systems, namely, the anisotropic Kondo model and the discrete unstable nonlinear Schrödinger equation. Our findings highlight the diversity of these low-dimensional systems and the interesting phenomena we have observed in them. There are three themes that are common to both models. These are the nonlinearity associated with each of the systems, the time-dependence of the phenomena we observe, and the universality of the systems. The latter refers to the fact that different systems are governed by the same physics.

The Kondo physics explored in Part I emerges from the low-energy description provided by many models, which include the Anderson impurity model, the interacting resonant level model, and the Ohmic spin boson model. These models are used to describe systems as diverse as quantum dots and dynamic impurities in bulk metals. Similarly, the nonlinear Schrödinger equation studied in Part II is used to describe related phenomena is systems as diverse as large wave formation in the ocean, biological structures that are formed in DNA strands, and light propagation in nonlinear optical fibres. The universal behaviour of both systems is intimately tied to the non-linearities that are present in them. In Kondo physics, the non-linearities are repulsive Coulomb interactions between electrons and in optical waveguide arrays described by the nonlinear Schrödinger equation, nonlinearity is governed by the polarization of the electric field. The interesting phenomena that are present in both of these one-dimensional systems are observed during the time evolution from a non-equilibrium initial condition.

In Chapter 3, we found a connection between the ultraviolet and infrared dynamics for the anisotropic Kondo model, where the Kondo length is an emergent length scale. This was done by studying the

equivalent Ohmic spin boson model, which allowed us to make use of the multimode coherent state expansion to calculate quantum quenches with equal accuracy at all energy scales. The quenches we considered were from strongly correlated ground states of the Kondo model to a Fermi sea, where the Kondo coupling is abruptly switched off and the system time evolves to the new Hamiltonian. We calculated the Loschmidt echo, which is defined as the transition amplitude between the initial and evolved state at some time after the quench, as well as the overlap between ground states before and after the quench. We motivated a scaling Ansatz for the Loschmidt echo from which we extracted the Kondo length dependence of the overlap at a fixed Kondo coupling. Our main result revealed a new power-law exponent for the overlap, which is equal to the difference between the ultraviolet and infrared exponents of the Loschmidt echo. We emphasised that it may be interesting to revisit results for the overlap in studies of other systems that have focused on system size dependence to see if similar connections exist.

In Chapter 5, we found that the effects of random fluctuations on the onset times of rogue waves in the discrete unstable nonlinear Schrödinger equation are prominent for small modulation instability, but that large modulation instability dominates the onset behaviour. This was done by performing a linear stability analysis on the discrete unstable nonlinear Schrödinger equation when applying a small perturbation to the system. This yielded a modulation instability function which depends on the wave numbers of both the carrier wave and the perturbation, and which provides a region of instability of the system where rogue waves are likely to occur. Numerical simulations showed that a small perturbation to the system in this region results in the formation of rogue waves that emerge from the background after some time. For a particular initial condition, the longer time dynamics of the system, results in long-lived rogue waves. Our main findings show that when random fluctuations in the system are increased for small modulation instability, there is an earlier onset time for rogue waves in the system. Near the maximum modulation instability, there is a convergence to the same onset time for all values of the random fluctuations. It is hoped that these results can be experimentally realised in real optical waveguide arrays.

References

[1] V. E. Zakharov and L. A. Ostrovsky, "Modulation instability: The beginning," *Physica D* **238** no. 5, (2009) 540 – 548.

[2] L. D. Landau and E. M. Lifschits, "Course of Theoretical Physics," vol. 9, pp. 1 – 385. Pergamon, 1980.

[3] T. Giamarchi, "One-dimensional physics in the 21st century," *C. R. Physique* **17** no. 3, (2016) 322 – 331.

[4] I. Affleck, "Non-Fermi Liquid Behavior in Kondo Models," *J. Phys. Soc. Jpn.* **74** no. 1, (2005) 59–66.

[5] M. Balkanski and I. Yanchev, *Fabrication, Properties and Applications of Low-Dimensional Semiconductors*. Springer, Dordrecht, 1st ed., 1995.

[6] J. Kondo, "Resistance Minimum in Dilute Magnetic Alloys," *Prog. Theor. Phys.* **32** no. 1, (Jul, 1964) 37–49.

[7] P. W. Anderson, "Localized Magnetic States in Metals," *Phys. Rev.* **124** (Oct, 1961) 41–53.

[8] W. J. de Haas, J. de Boer, and G. J. van dën Berg, "The electrical resistance of gold, copper and lead at low temperatures," *Physica* **1** no. 7, (1934) 1115 – 1124.

[9] A. J. Dekker, "The resistivity of dilute magnetic alloys," *Physica* **25** no. 7, (1959) 1244 – 1252.

[10] A. D. Brailsford and A. W. Overhauser, "Theory of the resistance minimum in dilute paramagnetic alloys," *J. Phys. Chem. Solids* **15** no. 1, (1960) 140 – 145.

[11] J. R. Schrieffer and P. A. Wolff, "Relation between the Anderson and Kondo Hamiltonians," *Phys. Rev.* **149** (Sep, 1966) 491–492.

[12] A. Altland and B. D. Simons, *Condensed Matter Field Theory*. Cambridge University Press, 2nd ed., 2010.

[13] A. C. Hewson, *The Kondo Problem to Heavy Fermions*. Cambridge Studies in Magnetism. Cambridge University Press, 1st ed., 1993.

[14] P. W. Anderson, "A poor man's derivation of scaling laws for the Kondo problem," *J. Phys. Condens. Matter* **3** no. 12, (Dec, 1970) 2436–2441.

[15] K. G. Wilson and J. Kogut, "The renormalization group and the ϵ expansion," *Phys. Rep.* **12** no. 2, (1974) 75 – 199.

[16] R. Bulla, T. A. Costi, and T. Pruschke, "Numerical renormalization group method for quantum impurity systems," *Rev. Mod. Phys.* **80** (Apr, 2008) 395–450.

[17] A. Alvermann and H. Fehske, "Sparse Polynomial Space Approach to Dissipative Quantum Systems: Application to the Sub-Ohmic Spin-Boson Model," *Phys. Rev. Lett.* **102** (Apr, 2009) 150601.

[18] S. F. Huelga and M. B. Plenio, "Vibrations, quanta and biology," *Contemp. Phys.* **54** no. 4, (2013) 181–207.

[19] L. Magazzù, P. Forn-Díaz, R. Belyansky, J. -L. Orgiazzi, M. A. Yurtalan, M. R. Otto, A. Lupascu, C. M. Wilson, and M. Grifoni, "Probing the strongly driven spin-boson model in a superconducting quantum circuit," *Nat. Commun.* **9** (Apr, 2018) 1403.

[20] A. J. Leggett, S. Chakravarty, A. T. Dorsey, M. P. A. Fisher, A. Garg, and W. Zwerger, "Dynamics of the dissipative two-state system," *Rev. Mod. Phys.* **59** (Jan, 1987) 1–85.

[21] J. von Delft and H. Schoeller, "Bosonization for beginners — refermionization for experts," *Ann. Phys. (Berl.)* **7** no. 4, (1998) 225–305.

[22] R. A. Harris and R. Silbey, "On the stabilization of optical isomers through tunneling friction," *J. Chem. Phys.* **78** no. 12, (1983) 7330–7333.

[23] R. A. Harris and R. Silbey, "Variational calculation of the tunneling system interacting with a heat bath. II. Dynamics of an asymmetric tunneling system," *J. Chem. Phys.* **83** no. 3, (1985) 1069–1074.

[24] C. D. Pelwan and I. Snyman, "Ultraviolet dynamics from ground-state overlap in the Kondo model," *Phys. Rev. B* **99** (Feb, 2019) 075432.

[25] W. Münder, A. Weichselbaum, M. Goldstein, Y. Gefen, and J. von Delft, "Anderson orthogonality in the dynamics after a local quantum quench," *Phys. Rev. B* **85** (Jun, 2012) 235104.

[26] S.-J. Gu, "Fidelity approach to quantum phase transitions," *Int. J. Mod. Phys. B* **24** (Nov, 2010) 4371–4458.

[27] A. Weichselbaum, W. Münder, and J. von Delft, "Anderson orthogonality and the numerical renormalization group," *Phys. Rev. B* **84** (Aug, 2011) 075137.

[28] S. L. Lukyanov, H. Saleur, J. L. Jacobsen, and R. Vasseur, "Exact overlaps in the kondo problem," *Phys. Rev. Lett.* **114** (Feb, 2015) 080601.

[29] S. L. Lukyanov, "Fidelities in the spin-boson model," *J. Phys. A* **49** no. 16, (Mar, 2016) 164002.

[30] V. Khemani, R. Nandkishore, and S. L. Sondhi, "Nonlocal adiabatic response of a localized system to local manipulations," *Nat. Phys* **11** (Jun, 2015) 560–565.

[31] D.-L. Deng, J. H. Pixley, X. Li, and S. Das Sarma, "Exponential orthogonality catastrophe in single-particle and many-body localized systems," *Phys. Rev. B* **92** (Dec, 2015) 220201.

[32] R. Vasseur and J. E. Moore, "Multifractal orthogonality catastrophe in one-dimensional random quantum critical points," *Phys. Rev. B* **92** (Aug, 2015) 054203.

[33] P. Zanardi and N. Paunković, "Ground state overlap and quantum phase transitions," *Phys. Rev. E* **74** (Sep, 2006) 031123.

[34] M. Cozzini, R. Ionicioiu, and P. Zanardi, "Quantum fidelity and quantum phase transitions in matrix product states," *Phys. Rev. B* **76** (Sep, 2007) 104420.

[35] H.-Q. Zhou, R. Orús, and G. Vidal, "Ground State Fidelity from Tensor Network Representations," *Phys. Rev. Lett.* **100** (Feb, 2008) 080601.

[36] A. O. Gogolin, "Local time-dependent perturbation in Luttinger liquid," *Phys. Rev. Lett.* **71** (Nov, 1993) 2995–2998.

[37] F. Ares, K. S. Gupta, and A. R. de Queiroz, "Orthogonality catastrophe and fractional exclusion statistics," *Phys. Rev. E* **97** (Feb, 2018) 022133.

[38] G. Yuval and P. W. Anderson, "Exact Results for the Kondo Problem: One-Body Theory and Extension to Finite Temperature," *Phys. Rev. B* **1** (Feb, 1970) 1522–1528.

[39] J. J. Hopfield, "Infrared divergences, x-ray edges, and all that," *Comments Solid State Phys.* **2** (1969) .

[40] K. Ohtaka and Y. Tanabe, "Theory of the soft-x-ray edge problem in simple metals: historical survey and recent developments," *Rev. Mod. Phys.* **62** (Oct, 1990) 929–991.

[41] R. Vasseur, K. Trinh, S. Haas, and H. Saleur, "Crossover Physics in the Nonequilibrium Dynamics of Quenched Quantum Impurity Systems," *Phys. Rev. Lett.* **110** (Jun, 2013) 240601.

[42] D. M. Kennes, V. Meden, and R. Vasseur, "Universal quench dynamics of interacting quantum impurity systems," *Phys. Rev. B* **90** (Sep, 2014) 115101.

[43] P. Nordlander, M. Pustilnik, Y. Meir, N. S. Wingreen, and D. C. Langreth, "How Long Does It Take for the Kondo Effect to Develop?," *Phys. Rev. Lett.* **83** (Jul, 1999) 808–811.

[44] F. B. Anders and A. Schiller, "Real-Time Dynamics in Quantum-Impurity Systems: A Time-Dependent Numerical Renormalization-Group Approach," *Phys. Rev. Lett.* **95** (Oct, 2005) 196801.

[45] D. Lobaskin and S. Kehrein, "Crossover from nonequilibrium to equilibrium behavior in the time-dependent Kondo model," *Phys. Rev. B* **71** (May, 2005) 193303.

[46] F. B. Anders and A. Schiller, "Spin precession and real-time dynamics in the Kondo model: Time-dependent numerical renormalization-group study," *Phys. Rev. B* **74** (Dec, 2006) 245113.

[47] M. Heyl and S. Kehrein, "Interaction quench dynamics in the Kondo model in the presence of a local magnetic field," *J. Phys.: Condens. Matter* **22** no. 34, (Aug, 2010) 345604.

[48] M . Medvedyeva, A. Hoffmann, and S. Kehrein, "Spatiotemporal buildup of the Kondo screening cloud," *Phys. Rev. B* **88** (Sep, 2013) 094306.

[49] B. Lechtenberg and F. B. Anders, "Spatial and temporal propagation of Kondo correlations," *Phys. Rev. B* **90** (Jul, 2014) 045117.

[50] S. Ghosh, P. Ribeiro and M. Haque, "Dynamics of the impurity screening cloud following quantum quenches of the resonant level model," *J. Stat. Mech.: Theory Exp.* **2015** no. 8, (Aug, 2015) P08002.

[51] J. A. Andrade, A. A. Aligia, and P. S. Cornaglia, "Many-body dynamics of the decay of excitons of different charges in a quantum dot," *Phys. Rev. B* **94** (Dec, 2016) 235109.

[52] C. Latta, F. Haupt, M. Hanl, A. Weichselbaum, M. Claassen, W. Wuester, P. Fallahi, S. Faelt, L. Glazman, J. von Delft, H. E. Türeci, and A. Imamoglu, "Quantum quench of Kondo correlations in optical absorption," *Nature* **474** (Jun, 2011) 627–630.

[53] P. W. Anderson, "Infrared Catastrophe in Fermi Gases with Local Scattering Potentials," *Phys. Rev. Lett.* **18** (Jun, 1967) 1049–1051.

[54] P. W. Anderson, "Ground State of a Magnetic Impurity in a Metal," *Phys. Rev.* **164** (Dec, 1967) 352–359.

[55] F. Guinea, V. Hakim, and A. Muramatsu, "Bosonization of a two- level system with dissipation," *Phys. Rev. B.* **32** (Oct, 1985) 4410–4418.

[56] G . Kotliar and Q. Si, "Toulouse points and non-Fermi-liquid states in the mixed-valence regime of the generalized Anderson model," *Phys. Rev. B* **53** (May, 1996) 12373–12388.

[57] T. A. Costi and G. Zaránd, "Thermodynamics of the dissipative two-state system: A Bethe-ansatz study," *Phys. Rev. B* **59** (May, 1999) 12398–12418.

[58] S. Florens and I. Snyman, "Universal spatial correlations in the anisotropic Kondo screening cloud: Analytical insights and numerically exact results from a coherent state expansion," *Phys. Rev. B* **92** (Nov, 2015) 195106.

[59] M. Hanl and A. Weichselbaum, "Local susceptibility and Kondo scaling in the presence of finite bandwidth," *Phys. Rev. B* **89** (Feb, 2014) 075130.

[60] Z. Blunden-Codd, S. Bera, B. Bruognolo, N.-O. Linden, A. W. Chin, J. von Delft, A. Nazir, and S. Florens, "Anatomy of quantum critical wave functions in dissipative impurity problems," *Phys. Rev. B* **95** (Feb, 2017) 085104.

[61] S. Bera, A. Nazir, A. W. Chin, H. U. Baranger, and S. Florens, "Generalized multipolaron expansion for the spin-boson model: Environmental entanglement and the biased two-state system," *Phys. Rev. B* **90** (Aug, 2014) 075110.

[62] S. Bera, S. Florens, H. U. Baranger, N. Roch, A. Nazir, and A. W. Chin, "Stabilizing spin coherence through environmental entanglement in strongly dissipative quantum systems," *Phys. Rev. B* **89** (Mar, 2014) 121108.

[63] K. E. Cahill, "Coherent-State Representations for the Photon Density Operator," *Phys. Rev.* **138** (Jun, 1965) B1566–B1576.

[64] N. Gheeraert, X. H. H. Zhang, T. Sépulcre, S. Bera, N. Roch, H. U. Baranger, and S. Florens, "Particle production in ultrastrong-coupling waveguide QED," *Phys. Rev. A* **98** (Oct, 2018) 043816.

[65] N. Gheeraert, S. Bera, and S. Florens, "Spontaneous emission of Schrödinger cats in a waveguide at ultrastrong coupling," *New J. Phys.* **19** no. 2, (Feb, 2017) 023036.

[66] N. Akhmediev, J. M. Soto-Crespo, and A. Ankiewicz, "Extreme waves that appear from nowhere: On the nature of rogue waves," *Phys. Lett.* **373** no. 25, (2009) 2137 – 2145.

[67] C. Kharif and E. Pelinovsky, "Physical mechanisms of the rogue wave phenomenon," *Eur. J. Mech. B Fluids* **22** no. 6, (2003) 603 – 634.

[68] J. K. Mallory, "Abnormal waves on the south-east of South Africa," *Inst. Hydrog. Rev.* **51** (Jan, 1974) 89–129.

[69] T. A. A. Adcock, P. H. Taylor, S. Yan, Q. W. Ma, and P. A. E. M. Janssen, "Did the Draupner wave occur in a crossing sea?," *Proc. R. Soc. A* **467** no. 2134, (2011) 3004–3021.

[70] G. Z. Forristall, S. F. Barstow, H. E. Krogstad, M. Prevosto, P. H. Taylor, and P. S. Tromans, "Wave Crest Sensor Intercomparison Study: An Overview of WACSIS ," *J. Offshore Mech. Arct. Eng.* **126** no. 1, (03, 2004) 26–34.

[71] M. Onorato, S. Residori, U. Bortolozzo, A. Montina, and F. T. Arecchi, "Rogue waves and their generating mechanisms in different physical contexts," *Phys. Rep* **528** no. 2, (2013) 47 – 89.

[72] C. Kharif, E. Pelinovsky, and A. Slunyaev, *Advances in Geophysical and Environmental Mechanics and Mathematics*. Springer-Verlag Berlin Heidelberg, 1st ed., 2009.

[73] H. Tomiwa and T. Kawamura, "Statistical Analysis and Inference from the In-Situ Data of the Sea of Japan with Reference to Abnormal and/or Freak Waves," in *The Tenth International Offshore and Polar Engineering Conference*, vol. 28. International Society of Offshore and Polar Engineers, 2000.

[74] J. Touboul, C. Kharif, E. Pelinovsky, and J.-P. Giovanangeli, "On the interaction of wind and steep gravity wave groups using Miles' and Jeffreys' mechanisms," *Nonlinear Process. Geophys* **15** (2008) 1023–1031.

[75] M. Longuet-Higgins, "On the statistical distributions of sea waves," *J. Mar. Res.* **11** (1998) 245–265.

[76] T. Yasuda and N. Mori, "Occurrence Properties of Giant Freak Waves in Sea Area around Japan," *J. of Waterw. Port Coast.* **123** no. 4, (1997) 209–213.

[77] M. Christou and K. Ewans, "Examining a Comprehensive Dataset Containing Thousands of Freak Wave Events: Part 2—Analysis and Findings," vol. 2 of *International Conference on Offshore Mechanics and Arctic Engineering*, pp. 827–837. 06, 2011.

[78] M. Christou and K. Ewans, "Examining a Comprehensive Dataset Containing Thousands of Freak Wave Events: Part 1—Description of the Data and Quality Control Procedure," vol. 2 of *International Conference on Offshore Mechanics and Arctic Engineering*, pp. 815–826. 06, 2011.

[79] P. Stansell, "Distributions of freak wave heights measured in the North Sea," *App. Ocean Res* **26** no. 1, (2004) 35 – 48.

[80] M. S. Longuet-Higgins and R. W. Stewart, "Changes in the form of short gravity waves on long waves and tidal currents," *J. Fluid Mech.* **8** no. 4, (1960) 565–583.

[81] J. W. Miles, "On the generation of surface waves by shear flows," *J. Fluid Mech.* **3** no. 2, (1957) 185–204.

[82] J. W. Miles, "On the generation of surface waves by turbulent shear flows," *J. Fluid Mech.* **7** no. 3, (1960) 469–478.

[83] L. F. Bliven, N. E. Huang, and S. R. Long, "Experimental study of the influence of wind on Benjamin–Feir sideband instability," *J. Fluid Mech.* **162** (1986) 237–260.

[84] T. Iizuka and M. Wadati, "The Rayleigh-Taylor Instability and Nonlinear Waves," *J. Phys. Soc. Japan* **59** no. 9, (1990) 3182–3193.

[85] A. Hadjihosseini, J. Peinke, and N. P. Hoffmann, "Stochastic analysis of ocean wave states with and without rogue waves," *New J. Phys.* **16** no. 5, (May, 2014) 053037.

[86] D. J. Kedziora, A. Ankiewicz, and N. Akhmediev, "Classifying the hierarchy of nonlinear-Schrödinger-equation rogue-wave solutions," *Phys. Rev. E* **88** (Jul, 2013) 013207.

[87] H. Hasimoto and H. Ono, "Nonlinear modulation of gravity waves," *J. Phys. Soc. Jpn* **33** no. 3, (1972) 805–811.

[88] A. R. Osborne, "The random and deterministic dynamics of 'rogue waves' in unidirectional, deep-water wave trains," *Marine Structures* **14** no. 3, (2001) 275 – 293.

[89] Y. V. Kartashov, B. A. Malomed, and L. Torner, "Solitons in nonlinear lattices," *Rev. Mod. Phys.* **83** (Apr, 2011) 247–305.

[90] M. H. Anderson, J. R. Ensher, M. R. Matthews, C. E. Wieman, and E. A. Cornell, "Observation of Bose-Einstein Condensation in a Dilute Atomic Vapor," *Science* **269** no. 5221, (1995) 198–201.

[91] U. Al-Khawaja, H. T. C. Stoof, R. G. Hulet, K. E. Strecker, and G. B. Partridge, "Bright Soliton Trains of Trapped Bose-Einstein Condensates," *Phys. Rev. Lett.* **89** (Oct, 2002) 200404.

[92] J. J. Stoker, *Long Waves in Shallow Water*, ch. 10, pp. 289–449. John Wiley and Sons, Ltd, 2011.

[93] N. J. Zabusky and M. D. Kruskal, "Interaction of "Solitons" in a Collisionless Plasma and the Recurrence of Initial States," *Phys. Rev. Lett.* **15** (Aug, 1965) 240–243.

[94] A. M. Kosevich, V. V. Gann, and A. I. Zhukov, "Magnetic soliton motion in a nonuniform magnetic field," *J. Exp. Theor. Phys* **87** (Aug, 1998) 401–407.

[95] T. Heimburg and A. D. Jackson, "On soliton propagation in biomembranes and nerves," *Proc. Natl. Acad. Sci. U.S.A* **102** no. 28, (2005) 9790–9795.

[96] P. Petersonm, T. Soomere, J. Engelbrecht, and E. van Groesen, "Soliton interaction as a possible model for extreme waves in shallow water," *Nonlin. Proc. Geophys.* **10** no. 6, (2003) 503–510.

[97] A. Hasegawa and F. Tappert, "Transmission of stationary nonlinear optical pulses in dispersive dielectric fibers. I. Anomalous dispersion," *Appl. Phys. Lett.* **23** no. 3, (1973) 142–144.

[98] A. Hasegawa and F. Tappert, "Transmission of stationary nonlinear optical pulses in dispersive dielectric fibers. II. Normal dispersion," *Appl. Phys. Lett.* **23** no. 4, (1973) 171–172.

[99] B. Malomed, *Soliton Management in Periodic Systems*, pp. 1 – 12. Springer, Boston, MA, 2006.

[100] H. A. Haus and W. S. Wong, "Solitons in optical communications," *Rev. Mod. Phys.* **68** (Apr, 1996) 423–444.

[101] L. Debnath, *The Nonlinear Schrödinger Equation and Solitary Waves*, ch. 10, pp. 405–450. Birkhäuser, Boston, MA, 1st ed., 1997.

[102] R. W. Boyd, *Chapter 2 - Wave-Equation Description of Nonlinear Optical Interactions*, pp. 67 – 127. Academic Press, San Diego, 2nd ed., 2003.

[103] G. Agrawal, *Chapter 3 - Group-Velocity Dispersion*, pp. 57 – 85. Optics and Photonics. Academic Press, Boston, 5th ed., 2013.

[104] G. Agrawal, *Chapter 5 - Optical Solitons*, pp. 129 – 191. Optics and Photonics. Academic Press, Boston, 5th ed., 2013.

[105] L. F. Mollenauer, R. H. Stolen, and J. P. Gordon, "Experimental Observation of Picosecond Pulse Narrowing and Solitons in Optical Fibers," *Phys. Rev. Lett.* **45** (Sep, 1980) 1095–1098.

[106] A. Hasegawa, "Numerical study of optical soliton transmission amplified periodically by the stimulated Raman process," *Appl. Opt.* **23** no. 19, (Oct, 1984) 3302–3309.

[107] T. Li and R. Giles, "Optical amplifiers transform long-distance lightwave telecommunications," *Proc. IEEE* **84** no. 6, (Jun, 1996) 870–883.

[108] D. R. Solli, C. Ropers, P. Koonath, and B. Jalali, "Optical rogue waves," *Nature* **450** (Dec, 2007) 1054–1057.

[109] F. Lederer, S. Darmanyan, and A. Kobyakov, *Discrete Solitons in Nonlinear Waveguide Arrays*, pp. 131–157. NATO Science Series (Series II: Mathematics, Physics and Chemistry). Springer, Dordrecht, 1st ed., 2001.

[110] O. Steuernagel, "Equivalence between focused paraxial beams and the quantum harmonic oscillator," *Am. J. Phys* **73** no. 7, (2005) 625–629.

[111] M. A. M. Marte and S. Stenholm, "Paraxial light and atom optics: The optical Schrödinger equation and beyond," *Phys. Rev. A* **56** (Oct, 1997) 2940–2953.

[112] C. Etrich, F. Lederer, B. Malomed, T. Peschel, and U. Peschel, "Optical Solitons in Media with a Quadratic Nonlinearity," *Prog. Optics* **41** (12, 2000) 483–568.

[113] J. M. Zeuner, M. C. Rechtsman, Y. Plotnik, Y. Lumer, S. Nolte, M. S. Rudner, M. Segev, and A. Szameit, "Observation of a Topological Transition in the Bulk of a Non-Hermitian System," *Phys. Rev. Lett.* **115** (Jul, 2015) 040402.

[114] A. L. Jones, "Coupling of Optical Fibers and Scattering in Fibers," *J. Opt. Soc. Am.* **55** no. 3, (Mar, 1965) 261–271.

[115] W. P. Su, J. R. Schrieffer, and A. J. Heeger, "Solitons in Polyacetylene," *Phys. Rev. Lett.* **42** (Jun, 1979) 1698–1701.

[116] B. A. Bernevig and T. L. Hughes, *Topological Insulators and Topological Superconductors*. Princeton University Press, STU - Student ed., 2013.

[117] M. C. Rechtsman, J. M. Zeuner, Y. Plotnik, Y. Lumer, D. Podolsky, F. Dreisow, S. Nolte, M. Segev, and A. Szameit, "Photonic Floquet topological insulators," *Nature* **496** (Sep, 2013) 196.

[118] O. Bahat-Treidel, O. Peleg, M. Grobman, N. Shapira, M. Segev, and T. Pereg-Barnea, "Klein Tunneling in Deformed Honeycomb Lattices," *Phys. Rev. Lett.* **104** (Feb, 2010) 063901.

[119] F. Dreisow, M. Heinrich, R. Keil, A. Tünnermann, S. Nolte, S. Longhi, and A. Szameit, "Classical Simulation of Relativistic Zitterbewegung in Photonic Lattices," *Phys. Rev. Lett.* **105** (Sep, 2010) 143902.

[120] F. Lederer, G. I. Stegeman, D. N. Christodoulides, G. Assanto, M. Segev, and Y. Silberberg, "Discrete solitons in optics," *Phys. Rep.* **463** no. 1, (2008) 1 – 126.

[121] D. N. Christodoulides and R. I. Joseph, "Discrete self-focusing in nonlinear arrays of coupled waveguides," *Opt. Lett.* **13** no. 9, (Sep, 1988) 794–796.

[122] D. Cai, A. R. Bishop, and N. Grønbech-Jensen, "Localized states in discrete nonlinear Schrödinger equations," *Phys. Rev. Lett.* **72** (Jan, 1994) 591–595.

[123] H. Trompeter, U. Peschel, T. Pertsch, F. Lederer, U. Streppel, D. Michaelis, and A. Bräuer, "Tailoring guided modes in waveguide arrays," *Opt. Express* **11** no. 25, (Dec, 2003) 3404–3411.

[124] Y. V. Kartashov, V. A. Vysloukh, and L. Torner, "Soliton Shape and Mobility Control in Optical Lattices," vol. 52 of *Progress in Optics*, pp. 63 – 148. Elsevier, 2009.

[125] Y. Lahini, A. Avidan, F. Pozzi, M. Sorel, R. Morandotti, D. N. Christodoulides, and Y. Silberberg, "Anderson Localization and Nonlinearity in One-Dimensional Disordered Photonic Lattices," *Phys. Rev. Lett.* **100** (Jan, 2008) 013906.

[126] F. Palmero, R. Carretero-González, J. Cuevas, P. G. Kevrekidis, and W. Królikowski, "Solitons in one-dimensional nonlinear Schrödinger lattices with a local inhomogeneity," *Phys. Rev. E* **77** (Mar, 2008) 036614.

[127] D. Pierangeli, M. Flammini, L. Zhang, G. Marcucci, A. J. Agranat, P. G. Grinevich, P. M. Santini, C. Conti, E. DelRe, "Observation of Fermi-Pasta-Ulam-Tsingou Recurrence and Its Exact Dynamics," *Phys. Rev. X* **8** (Oct, 2018) 041017.

[128] S. Efe and C. Yuce, "Discrete rogue waves in an array of waveguides," *Phys. Lett.* **379** no. 18, (2015) 1251 – 1255.

[129] H. S. Eisenberg, Y. Silberberg, R. Morandotti, A. R. Boyd, and J. S. Aitchison, "Discrete Spatial Optical Solitons in Waveguide Arrays," *Phys. Rev. Lett.* **81** (Oct, 1998) 3383–3386.

[130] G. Stegeman, A. Villenevue, J. Kang, J. S. Aitchison, C. N. Ironside, K. Al-Hemyari, C. C. Yang, C.-H. Lin, H.-H. Lin, G. T. Kennedy, R. S. Grant, and W. Sibbett, "AlGaAs Below Half Bandgap: The Silicon of Nonlinear Materials," *Int. J. Nonlinear Opt. Phys.* **3** no. 3, (1994) 347–371.

[131] K. Itoh, W. Watanabe, S. Nolte, and C. Schaffer, "Ultrafast Processes for Bulk Modification of Transparent Materials," *MRS Bulletin* **31** no. 8, (2006) 620–625.

[132] F. T. Arecchi, U. Bortolozzo, A. Montina, and S. Residori., "Granularity and Inhomogeneity Are the Joint Generators of Optical Rogue Waves," *Phys. Rev. Lett.* **106** (Apr, 2011) 153901.

[133] M. Leonetti and C. Conti, "Observation of three dimensional optical rogue waves through obstacles," *Appl. Phys. Lett.* **106** no. 25, (2015) 254103.

[134] A. I. Maĭmistov, "Propagation of a light pulse in nonlinear tunnel-coupled optical waveguides," *Sov. J. Quantum Electron* **21** no. 6, (Jun, 1991) 687–690.

[135] W.-P. Zhong and B. Milivoj, "Traveling wave and soliton solutions of coupled nonlinear Schrödinger equations with harmonic potential and variable coefficients," *Phys. Rev. E* **82** (Oct, 2010) 047601.

[136] S. Trillo, S. Wabnitz, E. M. Wright, and G. I. Stegeman, "Optical solitary waves induced by cross-phase modulation," *Opt. Lett.* **13** no. 10, (Oct, 1988) 871–873.

[137] C. Paré and M. Florjanczyk, "Approximate model of soliton dynamics in all-optical couplers," *Phys. Rev. A* **41** (Jun, 1990) 6287–6295.

[138] N. N. Akhmediev and V. I. Korneev, "Modulation instability and periodic solutions of the nonlinear Schrödinger equation," *Theor. Math. Phys* **69** no. 2, (Nov, 1986) 1089–1093.

[139] V. E. Zaharov and A. B. Sabat, "Exact theory of two-dimensional self-focusing and one-dimensional self-modulation of waves in nonlinear media," *Sov. Phys. JETP* **34** (1972) 62–69.

[140] B. Kibler, J. Fatome, C. Finot, G. Millot, G. Genty, B. Wetzel, N. Akhmediev, F. Dias, and J. M. Dudley, "Observation of Kuznetsov-Ma soliton dynamics in optical fibre," *Sci. Rep.* **2** (Jun, 2012) .

[141] Q. Wang and X. Li, "Collision properties of rogue waves in optical fiber," *Opt. Commun.* **435** (2019) 255 – 264.

[142] T. B. Benjamin, "Instability of periodic wavetrains in nonlinear dispersive systems," *Proc. R. Soc. Lond. A* **299** no. 1456, (Jun, 1967) 59–76.

[143] M. Peyrard and A. R. Bishop, "Statistical mechanics of a nonlinear model for DNA denaturation," *Phys. Rev. Lett.* **62** (Jun, 1989) 2755–2758.

[144] T. B. Benjamin and J. E. Feir, "The disintegration of wave trains on deep water Part 1. Theory," *J. Fluid Mech.* **27** no. 3, (1967) 417–430.

[145] M. Onorato, A. R. Osborne, and M. Serio, "Modulational Instability in Crossing Sea States: A Possible Mechanism for the Formation of Freak Waves," *Phys. Rev. Lett.* **96** (Jan, 2006) 014503.

[146] V. E. Zakharov, A. I. Dyachenko, and A. O. Prokofiev, "Freak waves as nonlinear stage of Stokes wave modulation instability," *Eur. J. Mech. B Fluids* **25** no. 5, (2006) 677 – 692.

[147] S. K. Gupta and A. K. Sarma, "Peregrine rogue wave dynamics in the continuous nonlinear Schrödinger system with parity-time symmetric Kerr nonlinearity," *Commun. Nonlinear Sci. Numer. Simulat.* **36** (2016) 141 – 147.

[148] D. H. Peregrine, "Water waves, nonlinear Schrödinger equations and their solutions," *J. Austral. Math. Soc. Ser. B* **25** no. 1, (1983) 16–43.

[149] J. M. Dudley, G. Genty, F. Dias, B. Kibler, and N. Akhmediev, "Modulation instability, Akhmediev Breathers and continuous wave supercontinuum generation," *Opt. Express* **17** no. 24, (Nov, 2009) 21497–21508.

[150] V. N. Serkin, A. Ramirez, and T. L. Belyaeva, "Nonlinear-optical analogies to the Moses sea parting effect: Dark soliton in forbidden dispersion or nonlinearity," *Optik* **192** (2019) 162928.

[151] A. Visinescu and D. Grecu, "Modulational instability of some nonlinear continuum and discrete systems," *AIP Conf. Proc.* **729** no. 1, (2004) 389–395.

[152] J. W. Dold and D. H. Peregrine, *Water-Wave Modulation*, ch. 3, pp. 163–175. 1986.

[153] C. D. Pelwan, A. Quandt, and R. Warmbier, "Onset times of long-lived rogue waves in an optical waveguide array," *J. Opt. Soc. Am. A* **37** no. 11, (Nov, 2020) C67–C72.

[154] D. Pierangeli, F. Di Mei, C. Conti, A. J. Agranat, and E. DelRe, "Spatial rogue waves in photorefractive ferroelectrics," *Phys. Rev. Lett.* **115** (Aug, 2015) 093901.

[155] J. D. Tchinang Tchameu, A. B. Togueu Motcheyo, and C. Tchawoua, "Biological multi-rogue waves in discrete nonlinear Schrödinger equation with saturable nonlinearities," *Phys. Lett. A* **380** no. 38, (2016) 3057 – 3060.

[156] Y. Kivshar and M. Peyrard, "Modulational instabilities in discrete lattices," *Phys. Rev. A* **46** (Sep, 1992) 3198–3205.

[157] P. Virtanen, R. Gommers, T. Oliphant, *et al.*, "SciPy 1.0: Fundamental Algorithms for Scientific Computing in Python," *Nat. Methods* **17** (2020) 261–272.

[158] J. R. Dormand and P. J. Prince, "A family of embedded Runge-Kutta formulae," *J. Comput. Appl. Math* **6** no. 1, (1980) 19 – 26.

[159] N. Akhmediev, A. Ankiewicz, and M. Taki, "Waves that appear from nowhere and disappear without a trace," *Phys. Lett. A* **373** no. 6, (2009) 675 – 678.

[160] Y. V. Bludov and V. Konotop and N. Akhmediev, "Rogue waves as spatial energy concentrators in arrays of nonlinear waveguides," *Opt. Lett.* **34** no. 19, (Oct, 2009) 3015–3017.

[161] M. Erkintalo, G. Genty, B. Wetzel, and J. M. Dudley, "Akhmediev breather evolution in optical fiber for realistic initial conditions," *Phys. Lett. A* **375** no. 19, (2011) 2029 – 2034.

[162] V. L. Chaves Filho, R. P. A. Lima, and M. L. Lyra, "Interplay between modulational instability and self-trapping of wavepackets in nonlinear discrete lattices," *Chaos* **25** no. 6, (2015) 063101.

[163] R. Y. Chiao, E. Garmire, and C. H. Townes, "Self-Trapping of Optical Beams," *Phys. Rev. Lett.* **13** (Oct, 1964) 479–482.